

NASA Contractor Report 3641

NASA
CR
3640-
v.2
c.1

LOAN COPY
AFWL TECHN
KIRTLAND AF

0062147



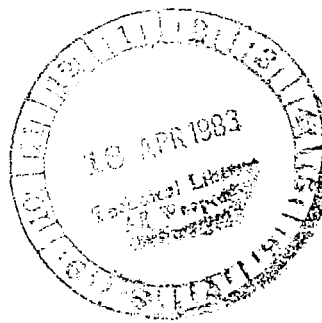
TECH LIBRARY KAFB, NM

Aeroelastic Loads Prediction for an Arrow Wing

Task II - Evaluation of Semi-Empirical Methods

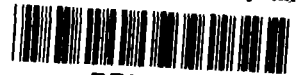
Andre C. Wery and Robert M. Kulfan

CONTRACT NAS1-15678
MARCH 1983



25th Anniversary
1958-1983

NASA



NASA Contractor Report 3641

Aeroelastic Loads Prediction for an Arrow Wing

Task II - Evaluation of Semi-Empirical Methods

Andre C. Wery and Robert M. Kulfan
Boeing Commercial Airplane Company
Seattle, Washington

Prepared for
Langley Research Center
under Contract NAS1-15678



National Aeronautics
and Space Administration

Scientific and Technical
Information Branch

1983

CONTENTS

	Page
SUMMARY	1
INTRODUCTION	2
SYMBOLS	4
DATA BASE	6
Wind Tunnel Models	6
Wind Tunnel Testing	6
Data	6
BACKGROUND	8
APPROACH	10
Parameters Selected for Evaluation	10
Evaluation Criteria	11
EVALUATION OF PARAMETERS	12
Local Section Angle of Attack	12
Section Normal Force	12
Key Assumption	12
Applicability for Use in an Aeroelastic Analysis	12
Evaluation	13
Method Limitations	13
Full Theoretical Leading-Edge Suction Coefficient	14
Net Leading-Edge Suction Coefficient	14
Key Assumption	14
Applicability for Use in an Aeroelastic Analysis	14
Evaluation	15
Streamwise Sections	15
Crossflow Sections	16
CONCLUSIONS	17
Pressures Related to Section Normal Force	17
Nonlinear Pressure Increments Related to Net Leading-Edge Suction	17
Streamwise Sections	17
Crossflow Sections	17
RECOMMENDATIONS	18
APPENDIX A. DESCRIPTION OF DATA BASE	19
APPENDIX B. DATA REDUCTION	61
APPENDIX C. METHOD FOR CALCULATING NET LEADING-EDGE SUCTION COEFFICIENTS	70
REFERENCES	75

LIST OF TABLES

	Page
1. Summary of Subsonic/Transonic Test Conditions by Test and Run Number ..	7
A-1. Wing Half-Thickness Distribution, Percent Chord	20
A-2. Wing Section Camber Definition, Percent Chord	22
A-3. Wing Pressure Orifice Locations, Percent Local Chord	24
A-4. Body Pressure Orifice Locations	31
A-5. Summary of Subsonic/Transonic Test Conditions by Run Number (NASA Contract NAS1-12875)	37
A-6. Summary of Subsonic/Transonic Test Conditions by Run Number (NASA Contract NAS1-14962)	40
A-7. Summary of Supersonic Test Conditions by Run Number. Reynolds Number = 8.65×10^6 (NASA Contract NAS1-14141)	41
B-1. Integration Constants	68

LIST OF FIGURES

	Page
A-1. General Arrangement and Characteristics	43
A-2. Spanwise Twist Distribution for the Model Wing	44
A-3. Cambered-Twisted Wing Section Geometry	45
A-4. Fin Geometry, Section at 0.725 Semispan	46
A-5. Pressure Orifice Locations	47
A-6. Control Surface Bracket Details	48
A-7. Boeing Transonic Wind Tunnel	49
A-8. Variation of Reynolds Number and Dynamic Pressure With Mach Number ..	50
A-9. Data Acquisition and Reduction System-Boeing Transonic Wind Tunnel	51
A-10. Schematic of 9- by 7-ft Supersonic Leg of NASA Ames Unitary Wind Tunnel	52
A-11. Data Acquisition and Reduction System-9- by 7-ft Supersonic Leg of NASA Ames Unitary Wind Tunnel	53
A-12. Model in Boeing Transonic Wind Tunnel-Flat Wing; L.E. Deflection, Full Span = 0.0°; T.E. Deflection, Full Span = 0.0° (NASA Contract NAS1-12875)	54
A-13. Model in Boeing Transonic Wind Tunnel-Twisted Wing; T.E. Deflection, Full Span = 0.0°; (NASA Contract NAS1-14962)	55
A-14. Model in Boeing Transonic Wind Tunnel-Cambered-Twisted Wing, Fin Off; T.E. Deflection, Full Span = 0.0°; (NASA Contract NAS1-14962)	56
A-15. Model in Boeing Transonic Wind Tunnel-Cambered-Twisted Wing, Fin On; T.E. Deflection, Full Span = 0.0° (NASA Contract NAS1-14962)	57
A-16. Model Installation in Boeing Transonic Wind Tunnel (NASA Contracts NAS1-12875 and NAS1-14962)	58
A-17. Model in 9- by 7-ft Supersonic Leg of NASA Ames Unitary Wind Tunnel- Flat Wing, Rounded L.E. (NASA Contract NAS1-14141)	59
A-18. Model in 9- by 7-ft Supersonic Leg of NASA Ames Unitary Wind Tunnel- Twisted Wing (NASA Contract NAS1-14141)	59
A-19. Model Installation in 9- by 7-ft Supersonic Leg of NASA Ames Unitary Wind Tunnel (NASA Contract NAS1-14141)	60
B-1. Codes Used to Interpolate and Extrapolate	69
C-1. Sample Calculation of C_l , Flat Wing, $M = 0.85$, $\delta = 10^\circ$, $\eta = 0.319$	74
1. General Arrangement and Characteristics	77
2. Spanwise Twist Distribution for the Model Wing	78
3. Cambered-Twisted Wing Section Geometry	78
4. Pressure Orifice Locations	79
5. Upper Surface Isobars, Flat Wing, Rounded Leading Edge, $M = 0.85$	80
6. Comparison of Experimental Section Normal Force Coefficients for Two Wing Shapes, $M = 0.85$, $\eta = 0.80$	80
7. Typical Procedures Used for Aerolastic Loads Prediction, $M = 0.85$, $\eta = 0.80$	81
8. Net Leading-Edge Suction Coefficients for the Three Wing Shapes, Rounded Leading Edge, $M = 0.85$, Calculated From FLEXSTAB Pressures	82
9. Proposed Iterative Aeroelastic Loads Prediction Method Based on Section Normal Force Coefficient	84
10. Chordwise Pressure Distributions Which Produce the Same Section Normal Force Coefficient, Flat and Twisted Wings, $M = 0.85$	85

LIST OF FIGURES (Concluded)

		Page
11.	Chordwise Pressure Distributions Which Produce the Same Section Normal Force Coefficient, Twisted and Cambered-Twisted Wings, $M = 0.85$	89
12.	Comparison of Experimental Section Normal Force Coefficients for Three Wing Shapes, $M = 0.85$	93
13.	Definition of Streamwise Wing Sections	94
14.	Definition of Crossflow Wing Sections	94
15.	Proposed Iterative Aeroelastic Loads Prediction Method Based on Net Leading-Edge Suction Coefficient	95
16.	Procedure to Establish a Data Base Which Relates Nonlinear Pressure Coefficients to Net Leading-Edge Suction Coefficient	96
17.	Prediction of Streamwise Section Coefficients for the Cambered-Twisted Wing Using the Data Base for the Flat Wing Data Related to the Net Leading-Edge Suction Coefficient, $M = 0.85$	97
18.	Prediction of Streamwise Section Coefficients for the Cambered-Twisted Wing Using the Data Base for the Flat Wing Data Related to the Net Leading-Edge Suction Coefficient, Compared to Linear Theory, $M = 0.85$	98
19.	Prediction of Streamwise Section Coefficients for the Twisted Wing Using the Data Base for the Flat Wing Data Related to the Net Leading-Edge Suction Coefficient, $M = 0.85$	101
20.	Prediction of Streamwise Section Coefficients for the Cambered-Twisted Wing Using the Data Base for the Twisted Wing Data Related to the Net Leading-Edge Suction Coefficient, $M = 0.85$	102
21.	Incremental Nonlinear Net Pressure Coefficients as a Function of the Net Leading-Edge Suction Coefficient for the Three Wings, $\eta = 0.50$, $M = 0.85$	103
22.	Typical Variation of Crossflow Section Coefficients with Angle of Attack for the Three Wings, $M = 0.85$	105
23.	Prediction of Crossflow Section Coefficients for the Twisted Wing Using the Data Base for the Flat Wing Data Related to the Net Leading-Edge Suction Coefficient, $M = 0.85$	106
24.	Prediction of Crossflow Section Coefficients for the Cambered-Twisted Wing Using the Data Base for the Twisted Wing Data Related to the Net Leading-Edge Suction Coefficient, $M = 0.85$	108
25.	Prediction of Crossflow Section Coefficients for the Cambered-Twisted Wing Using the Data Base for the Flat Wing Data Related to the Net Leading-Edge Suction Coefficient, $M = 0.85$	110
26.	Prediction of Crossflow Section Coefficients for the Cambered-Twisted Wing Using the Data Base for the Flat Wing Data Related to the Net Leading-Edge Suction Coefficient, Compared to Linear Theory, $M = 0.85$	112
27.	Pressure Distribution on the Cambered-Twisted Wing Based on the Leading-Edge Suction Coefficients at Constant Body Stations and the Flat Wing Data Base, Streamwise Section, $\eta = 0.50$, $M = 0.85$, $\alpha = 12^\circ$	116

SUMMARY

The accurate prediction of loads on flexible, low aspect-ratio aircraft is critical to the design of reliable and efficient vehicles. The conditions for structural design frequently involve nonlinear aerodynamics.

Under previous NASA contracts (NAS1-12875, NAS1-14141, and NAS1-14962), a large experimental data base for three wing shapes was obtained and linear theoretical methods were evaluated. The current contract, NAS1-15678, extends the evaluation of state-of-the-art theoretical predictive methods to two separated-flow computer programs and also evaluates a semi-empirical method for incorporating the experimentally measured separated-flow effects into a linear aeroelastic analysis.

The resultant three tasks have been documented separately. This volume describes the development and evaluation of a semi-empirical method to predict pressure distributions on a deformed wing by using an experimental data base. The evaluation of R. P. White's (NASA Division of Systems Research Laboratories) separated-flow method (Task I) is described in NASA CR-3640. The evaluation of The Boeing Company's Three-Dimensional Leading-Edge Vortex (LEV) code (Task III) is presented in NASA CR-3642.

This semi-empirical method to predict pressure distributions uses an experimental data base in addition to a linear potential-flow solution. The experimental data accounts for the effects of aeroelasticity by relating the pressures to a parameter that is influenced by the deflected shape. Several parameters were examined before the net leading-edge suction coefficient was selected as the best.

INTRODUCTION

Accurate analytical techniques for the prediction of the magnitude and distribution of aeroelastic loads are required in order to achieve an optimum design of the structure of large flexible aircraft. Uncertainties in the characteristics of loads may result in an improper accounting for aeroelastic effects, leading to understrength or overweight designs and unacceptable fatigue life. In addition, the correct prediction of load distribution and the resultant structural deformation is essential to the determination of the aircraft stability and control characteristics, control power requirements, and flutter boundaries. The alternative to using satisfactory analytical techniques is the increased use of expensive, time-consuming wind tunnel testing for each aircraft configuration.

The problem of accurate load prediction becomes particularly acute for aircraft with low aspect-ratio wings where critical design conditions occur in the transonic speed regime. In this region at typical design angles of attack, the flow is generally nonlinear – mixed flow, embedded shocks, separation, and vortex flow.

A program was started in 1974 to systematically obtain experimental pressure data for an arrow wing throughout the subsonic, transonic, and low supersonic Mach numbers. This program was comprised of three NASA contracts: NAS1-12875, NAS1-14141, and NAS1-14962 (documented in refs. 1 through 12). As the specific objective was to understand the change in load with aeroelastic deformation, three wing shapes were tested – all with the same planform and thickness distribution. The first wing was flat (no camber or twist); the second has a spanwise twist (typical of aeroelastic deformation) but no camber; and the third has the same twist with camber superimposed.

In addition to the creation of a data base, which is useful for evaluating aeroelastic effects, a second objective was to evaluate state-of-the-art theoretical methods that might be used for this purpose. Primarily these methods were linear and the evaluations showed that linear theories are adequate at low angles of attack, which are typical of cruise conditions, and are basically capable of predicting loading changes due to smooth changes in wing shape at these low angles. However, at the higher angles of attack, which are typical of structural design conditions, these methods are not useful because the flow is nonlinear due to leading-edge separation of the flow. The limited comparisons that were made with advanced separated-flow methods indicated some hope, even though the aerodynamic panel model available at that time was very crude (only a few panels to represent the camber surface).

The current evaluation of methods for predicting pressure distributions when the flow is separated is divided into three tasks. Two currently available computer codes were evaluated in Tasks I and III, and an approach involving semi-empirical corrections to linear theory was investigated in Task II. The three tasks are essentially independent efforts and are documented separately: Task II, the development and evaluation of a semi-empirical method in this document; Task I, an evaluation of R. P. White's computer code in NASA CR-3640; and Task III, an evaluation of Boeing's Three-Dimensional Leading-Edge Vortex computer code in NASA CR-3642.

The semi-empirical methods evaluated in this task use wind tunnel pressure data from a representative model to predict the nonlinear aeroelastic load distribution on a wing when the flow is dominated by leading-edge vortices and areas of separated flow.

Several possible parameters were examined with which to relate the net pressures. The most successful of these is the net leading-edge suction coefficient, which is calculated from the theoretical pressures and directly accounts for the effects of aeroelastic wing camber and twist. This is because the pressures from the appropriate shape are used to calculate the suction coefficient. The results were best when using the leading-edge suction at the same body station.

SYMBOLS

b	wing span, cm
BL	buttock line, cm; distance outboard from model plane of symmetry
c	section chord length, cm
\bar{c} , M.A.C.	mean aerodynamic chord length, cm
C_B	surface bending moment coefficient referenced to y_{ref} , positive wingtip up
C_C	surface chord force coefficient; positive aft
C_c	section chord force coefficient; positive aft
C_M	surface pitching moment coefficient, referenced to 0.25 M.A.C.; positive leading edge up
C_m	section pitching moment coefficient referenced to section leading edge or side of body; positive leading edge up
$C_{m.25c}$	section pitching moment coefficient referenced to section 0.25c; positive leading edge up
C_N	surface normal force coefficient; positive up
C_n	section normal force coefficient; positive up
C_p	pressure coefficient = $\frac{\text{measured pressure} - \text{reference pressure}}{q}$
$C_{s,net}$	net leading-edge suction coefficient
D	body diameter, cm
M	Mach number
MS	model station, cm; measured aft along the body centerline from the nose
p_s	static pressure, kN/m ²
p_t	total pressure, kN/m ²
q	dynamic pressure, kN/m ²
S	reference area used for surface coefficients, cm ²

S_h	area of streamwise strip associated with a pressure station, cm^2 ; used in summation of section force coefficients (app. B)
x,y,z	general coordinates for distances in the longitudinal, lateral, and vertical directions respectively
y_{ref}	distance outboard of model centerline of the bending moment reference point, cm
α	corrected angle of attack, degrees; the angle between the wing-root chord and the relative wind measured in the model plane of symmetry; includes compensation for sting deflection, tunnel-flow angularities, and wall effects; positive nose up with respect to relative wind
α_{sec}	wing twist angle relative to wing reference plane, degrees; positive leading edge up
β	angle of sideslip, degrees; positive nose left with respect to relative wind
$\Delta C_{p,\text{NL}}$	nonlinear incremental pressure coefficient
δ	control surface deflection, degrees; positive leading edge down for leading edge (see exception in app. B) and trailing edge down for trailing edge
η	fraction of wing semispan, $y/(b/2)$
Λ	sweep angle, degrees; measured from a line perpendicular to the model centerline, positive aft
ϕ	angle defining location of pressure orifices on the surface of the cylindrical body at a constant MS, degrees; measured from the top of the body

Subscripts:

exp.	experimental data
L.E.	leading-edge control surface
lin.	linear theory
r	wing root
s	referenced to segment of local chord
T.E.	trailing-edge control surface

DATA BASE

The data obtained, both experimental and theoretical, have been presented in several papers (refs. 1 through 3) and are presented in more detail in numerous NASA reports (refs. 4 through 12).

WIND TUNNEL MODELS

The configuration chosen for this study was a thin, low aspect-ratio, highly swept wing mounted below the centerline of a high fineness-ratio body. The general arrangement and characteristics of the model are shown in figure 1. Two complete wings were constructed for contract NAS1-12875, one with no camber or twist and one with no camber but with a spanwise twist variation. A third wing with camber and twist was constructed for contract NAS1-14962. Deflectable control surfaces were available on all three of these wings.

The three wings, body, and fin used to create this data base are described in detail in appendix A. The wings all have the same planform, thickness distribution, and placement of orifices. The twisted wing and the cambered-twisted wing have the same twist, i.e., the coordinates of the leading edges and trailing edges of the two wings are the same. This twist distribution is shown in figure 2. Sections at the root, midspan, and tip of the cambered-twisted wing (fig. 3) show not only the camber but the position of the sections of the cambered-twisted wing and the twisted wing, relative to the wing reference plane (flat wing). The flat wing had a sharp-leading-edge segment in addition to the rounded-leading-edge segment common to all three wings.

The capability to measure the detailed load distribution on the wing and body of this configuration was provided by distributing 300 pressure orifices on the model. Each wing had 217 pressure orifices equally divided into seven streamwise sections on the left half. Orifices were located on both the top and bottom surfaces at the chordwise locations shown in figure 4. Pressure orifices were located on the body in five streamwise rows of 15 orifices each. An additional eight orifices in the area of the wing-body junction made a total of 83 orifices on the left side of the body.

WIND TUNNEL TESTING

The experimental data used in this study were obtained in the Boeing Transonic Wind Tunnel (BTWT) under NASA contracts NAS1-12875 and NAS1-14962. A description of the tunnel and tests are in appendix A. The current study was limited to the wings that had both leading-edge and trailing-edge control surfaces undeflected. Table 1 shows a summary of these data.

DATA

The measured pressures were edited, as necessary, to account for plugged or leaking orifices or missing data points. The pressure coefficients were then integrated, as described in appendix B, to obtain streamwise section coefficients and total surface coefficients. When pressure coefficients were required at points other than where measured, a linear interpolation was used.

Table 1.--Summary of Subsonic/Transonic Test Conditions by Test and Run Number

Contract	Test number	Mach number							Data document
		0.40	0.70	0.85	0.95	1.00	1.05	1.10	
Flat wing, rounded leading edge									
NAS1-12875	BTWT 1415	269	263	267	266	268	264	262	NASA CR-132727
Flat wing, sharp leading edge									
NAS1-12875	BTWT 1415	368	366	372	374	373	367	365	NASA CR-132727
Twisted wing, rounded leading edge									
NAS1-12875 NAS1-14962	BTWT 1415 BTWT 1627	450 15	445 14	449 13	447 12	448 11	446 10	444 -	NASA CR-132727 NASA CR-165701
Cambered-twisted wing, rounded leading edge (fin off)									
NAS1-14962	BTWT 1627	43	41	40	39	38	37	-	NASA CR-165701

BACKGROUND

The objective of Task II is to evaluate semi-empirical techniques for predicting pressure distributions in the presence of separated flows for application to the nonlinear aeroelastic loads analysis of highly swept wings.

The study is specifically directed at identifying the best approach for using wind tunnel pressure data from a representative model to predict the load distribution on an elastic airplane. This loads prediction technique will be used to account for the effects of aeroelasticity on the airload distribution, particularly when the flow over the wing is dominated by leading-edge vortices and areas of separated flow.

Wind tunnel pressure measurements have shown that the airload distributions on the surface of highly swept, low aspect-ratio wings at moderate to high angles of attack are highly nonlinear due to flow separation and the formation of leading-edge vortices. While a test provides accurate measurement of the airloads on a rigid model, including nonlinearities, there are no satisfactory methods for predicting these airloads including the effect of aeroelastic twist and camber. Assuming potential flow, only the linear loads and their linear variations due to aeroelasticity can be predicted by linear theories. Yet, the structural engineer who is faced with showing compliance of the structure to the maneuver and gust criteria, needs accurate aeroelastic load predictions throughout the range of airplane angle of attack.

In 1979, Boeing Independent Research and Development money supplemented NASA funds for investigating semi-empirical techniques for the predicting of nonlinear wing pressures on a deformed wing, using a known experimental distribution on a rigid wing. This research has been made possible by the availability of a large, wind tunnel data base, which was generated under previous NASA contracts. Data are included for three arrow wings that were deformed to simulate aeroelastic deformation, one flat, one twisted, and one cambered and twisted (see figs. 1 through 4), but having identical planform and thickness distribution. The nonlinearities that occur in total wing lift and local pressures on this configuration are documented in references 4 through 12. Comparisons between experimental data and data predicted using several linear theoretical methods are shown in references 4, 7, 8, 9, and 12.

Typical wing upper surface isobars are shown in figure 5 for the flat wing with rounded-leading edge at Mach = 0.85 for two angles of attack. At $\alpha = 2.1^\circ$, the flow over the upper surface is attached, and the pressure distribution can be predicted using linear theory. These theories will also accurately predict the changes in loading due to moderate aeroelastic deformation at these angles of attack (ref. 12). At $\alpha = 11.9^\circ$, the flow has separated along the leading edge, and a strong vortex dominates the flow over the wing. Total wing aerodynamic coefficients, wing section data, and local pressures all show highly nonlinear characteristics as a function of angle of attack. The linear theories cannot predict how such a lift distribution will vary when the wing deforms under load.

Figure 6 shows the section normal force coefficient versus angle of attack for a streamwise wing section located at 80-percent semispan for both the flat wing and the cambered-twisted wing. The objective of Task II will have been met when a semi-empirical technique, using the data from the flat wing as a data base, accurately predicts the cambered-twisted wing test data.

Two typical methods used in the past for aeroelastic load prediction are outlined in figure 7. Part (a) shows the prediction of section C_n for the cambered-twisted wing using the linear potential-flow theory FLEXSTAB; the shaded area shows the error between this linear prediction and actual test data.

Figure 7 (b) shows how the flat wing test data, corrected by linear theory for the incremental effect of twist and camber, would compare with actual test data. Clearly, neither of these methods is satisfactory.

APPROACH

The goal in this task was to find some parameter that would relate the net pressure coefficients from a data base wing shape to the net pressure coefficients on a deformed wing shape.

PARAMETERS SELECTED FOR EVALUATION

The following parameters were selected for examination:

- o Local section angle of attack (wing angle of attack plus local twist angle)
- o Local section normal force coefficient
- o Full theoretical leading-edge suction coefficient
- o Net leading-edge suction coefficient (includes effect of leading-edge shape and wing deformation)

For the first three of these parameters, the full net pressure coefficient would be obtained directly. However, only the nonlinear portion of the net pressure coefficient would be obtained from the data base when using the net leading-edge suction coefficient, and it would be added to the net pressure coefficient calculated using linear theory.

The use of the leading-edge suction analogy of Polhamus for predicting the gross effects of leading-edge vortices has been well substantiated for very sharp, thin, plate-type wind tunnel model wings (see ref. 13). This analogy uses the full theoretical leading-edge suction coefficient, which, as described in appendix C, is obtained from the net pressure distribution predicted by FLEXSTAB (refs. 14 through 17).

Experimental data have shown that wing thickness affects the growth and development of leading-edge vortices. Furthermore, the effects of wing thickness on the leading-edge vortex development depend on whether the leading edge is sharp or rounded.

The concept of net leading-edge suction has been formulated to account for thickness and leading-edge shape effects on leading-edge vortices (see refs. 18 and 19). The net suction coefficient relates the local vortex strength to the leading-edge suction calculated at what amounts to a reduced (or effective) angle of attack. This reduced angle of attack for wings with sharp-nose airfoils is equal to the average angle of attack over the front portion of the local streamwise airfoil upper surface. The vortex growth is assumed to begin when this angle becomes positive.

Using the same terminology, the effective angle of attack of airfoils with rounded noses is also reduced. At each section, the effective angle of attack is defined as the difference between the local angle of attack and the angle at which the leading-edge suction equals the parabolic nose drag (the local nose is approximated by a parabola). It is assumed that the local vortex growth begins when this angle becomes positive. The procedure used for this calculation is developed in references 18 and 19 and is summarized in appendix C.

The relationship of net leading-edge suction coefficient $C_{s,net}$ to angle of attack is shown in figure 8 for the flat wing, the twisted wing, and the cambered-twisted wing. The square root of $C_{s,net}$ is used because it is a linear function of the angle of attack in the range shown (-8° to $+16^\circ$).

EVALUATION CRITERIA

For each method examined under this task, the following points were considered:

- o Definition of a theoretical basis for the method
- o Identification of the key assumptions
- o Determination of how the method would be used with test data in an aeroelastic analysis
- o Evaluation of the method by comparing these predictions to linear-theory predictions and to test data for the appropriate configuration from references 1 through 12
 - Predict pressure distributions on the cambered-twisted wing using the flat wing data for the data base
 - Predict pressure distributions on the cambered-twisted wing using the twisted wing data for the data base
 - Predict pressure distributions on the twisted wing using the flat wing data for the data base
- o Identification of method limitations, deficiencies, improvement options, and/or alternate methods.

EVALUATION OF PARAMETERS

All evaluations were made at a Mach number of 0.85, as the data at that Mach number appears to be representative of the data on this configuration.

LOCAL SECTION ANGLE OF ATTACK

Relating pressure distributions to the local section angle of attack clearly could not account for the effects of wing camber changes. Therefore, the examination of this approach was limited to plotting of some of the data.

SECTION NORMAL FORCE

KEY ASSUMPTION

In this method, it must be assumed that aeroelastic wing twist and camber changes will not appreciably affect the shape of the chordwise pressure distributions for a specific section normal force coefficient and spanwise station.

APPLICABILITY FOR USE IN AN AEROELASTIC ANALYSIS

An aeroelastic method, based on relating the local net pressure to the section normal force coefficient, could be implemented as shown in figure 9. This method would be used to predict aeroelastic twist effects by using wind tunnel model data in the following manner:

1. Establish a data base using experimental pressure data. At each spanwise station, the net pressure coefficients are related to the section normal force coefficient obtained by the integration of these pressures.
2. Set external pressure field for FLEXSTAB to zero.
3. Execute FLEXSTAB – a trimmed, flexible airplane solution – for the required load factor. Include the appropriate external pressure field.
 - o Evaluate theoretical pressure distributions for this deformed shape
 - o Integrate the pressure coefficients (include external pressure field) to obtain the section normal force coefficient
4. Obtain the net pressure distribution from the data base for the section normal force coefficients, calculated in step 3, to use as the external pressure field in the FLEXSTAB solution.
5. Repeat steps 3 and 4 until the following converge:
 - o airplane angle of attack and,
 - o elevator angle required to trim

As stated above, this approach is based on the assumption that the shape of the chordwise pressure distribution is not affected by aeroelastic deflections. Since

chordwise camber does affect the shape of the pressure distribution, this approach is not expected to be applicable when there are chordwise camber changes.

EVALUATION

In order to evaluate this parameter, comparisons were made at a number of spanwise stations of the net pressure distributions that produced the same section normal force coefficients for the flat and twisted wings. This comparison is shown in figure 10. A similar comparison of data on the twisted and cambered-twisted wings is shown in figure 11.

The shapes of these pressure distributions on the flat wing and the twisted wing show small differences that would affect the ability to predict local loading and load paths. The pressures on the twisted wing and the cambered-twisted wing indicate that the simulated camber changes affect the shape of the chordwise load distributions significantly over most of the wing and, therefore, would affect not only local loading but overall torsion. In order to obtain a partial assessment of the effects of the difference in chordwise pressure distribution on the overall load distribution for the flat and the twisted wings, calculations were made of the bending moment, shear, and torsion about the reference axis; this was done by integrating the pressures shown in figure 10.

The results indicate that the difference in the pressure distribution, due to twist, have a very small effect on the overall wing shear, bending moment, and torsion. However, this can be misleading when analyzing the structure of low aspect-ratio wings that generally have multiple load paths. Similar calculations for the camber effect clearly show a significant discrepancy in torsion, which in turn would affect the aeroelastic behavior of the wing.

METHOD LIMITATIONS

In addition to the inaccuracies mentioned above, two major difficulties have been identified that affect the validity and potential usefulness of using normal force as a means of predicting pressure distributions.

1. This method requires the calculation of changes in section normal force caused by aeroelastic distortion. The change in aeroelastic shape affects both the strength and location of the leading-edge vortices. Hence, the effect of those changes on the spanwise normal force distribution is highly nonlinear and cannot be predicted by a linear-theory analysis, such as FLEXSTAB.
2. A second and perhaps more serious difficulty is illustrated by the section normal force comparisons in figure 12. At the inboard stations, the section normal force coefficients for the study wings increased with angle of attack over the range plotted. However, near the wing tip, the section normal force coefficients initially increase as the leading-edge vortex develops; then as the leading-edge vortex grows and the vortex core moves inboard, the normal force drops and remains nearly constant. The same normal force coefficient may occur at two or more angles of attack; however, the chordwise load distributions usually are significantly different. Also, comparisons of section normal force indicate the possibility of having a particular section normal force within the linear-flow region on the flat wing, and within a highly nonlinear-flow region on the cambered-twisted wing. Again, the chordwise load distributions are significantly different.

FULL THEORETICAL LEADING-EDGE SUCTION COEFFICIENT

The possibility of relating net pressures to the full theoretical leading-edge suction was briefly explored. The concept of using the net leading-edge suction as a parameter for predicting the appearance, growth, strength, and location of the leading-edge vortex, and hence, its incremental, nonlinear effect on the pressure distribution, seemed to be more in keeping with the Polhamus suction analogy.

NET LEADING-EDGE SUCTION COEFFICIENT

A two-part examination was undertaken to see if a possible relationship existed between the net leading-edge suction coefficient and the incremental net pressures. The first part of the examination used the more obvious approach, which was to relate these pressures to the leading-edge suction at the same spanwise location, with sections as defined in figure 13. The second approach (considering the flow on such a highly swept wing is frequently described as conical) was to relate the pressures to leading-edge suction at the same body station as shown in figure 14. In both cases, the leading-edge suction coefficient was evaluated using pressures in the streamwise sections that are typical of wing paneling for FLEXSTAB.

KEY ASSUMPTION

This empirical method assumes that the net incremental nonlinear pressures are a function of the net leading-edge suction coefficient $C_{s,net}$ as calculated from the theoretical FLEXSTAB pressures. This would imply that the normal force and pitching moment coefficients resulting from these pressure distributions are also a unique function of $C_{s,net}$. These assumptions hold for either the streamwise or constant body station method.

APPLICABILITY FOR USE IN AN AEROELASTIC ANALYSIS

An aeroelastic method based on this type of relationship would be implemented as shown in figure 15. Aeroelastic loads would be predicted in the following manner:

1. Establish a data base, as shown in figure 16, using experimental pressure data and FLEXSTAB-generated theoretical pressures for the same model.
 - o Obtain incremental, nonlinear net pressure coefficients (difference between experiment and linear theory) as a function of angle of attack.
 - o Calculate (see app. C) net leading-edge suction coefficients as a function of spanwise location and angle of attack.
 - o Relate incremental, nonlinear net pressure coefficients to net leading-edge suction coefficient at the same angle of attack.
2. Set external pressure field for FLEXSTAB to zero.

3. Execute FLEXSTAB – a trimmed, flexible airplane solution – for the required load factor. Include the appropriate external pressure field.
 - o Evaluate theoretical pressure distributions for this deformed shape.
 - o Calculate net leading-edge suction coefficients using these pressures.
4. Obtain the incremental, nonlinear net pressure distribution from the data base for the net leading-edge suction coefficients calculated in step 3 to use as the external pressure field in the FLEXSTAB solution.
5. Repeat steps 3 and 4 until the following converge:
 - o airplane angle of attack and,
 - o elevator angle required to trim.

EVALUATION

Streamwise Sections

The nonlinear portions of the local net pressures for the flat, the twisted, and the cambered-twisted wings were displayed versus the square root of the net leading-edge suction coefficient at several streamwise sections. The plots tended to coincide, especially for the inboard sections in the vicinity of the leading edge; but no measure of goodness in this relationship could be shown using that particular mode.

Section C_n and $C_{m.25c}$ for the cambered-twisted wing were predicted, using the data base generated from the flat wing data, in the following manner:

- o Integrate the FLEXSTAB-generated linear pressure distribution to obtain section C_n and $C_{m.25c}$ for the cambered-twisted wing.
- o Calculate the net leading-edge suction coefficient using these pressure distributions.
- o Obtain the incremental, nonlinear section C_n and $C_{m.25c}$ from the data base for these suction coefficients.
- o Combine the coefficients from linear theory and from the data base.

The predicted section C_n and $C_{m.25c}$ were then compared to the actual test values at the seven streamwise sections along the span at which pressures were measured on the test models. This comparison of the section coefficients as a function of $C_{s,net}$ is shown in figure 17. These coefficients are also shown as a function of angle of attack in figure 18, with those predicted by FLEXSTAB added to show the results of a typical linear theory.

As shown in figure 19, the procedure was repeated for the twisted wing – again using the data base for the flat wing in order to isolate the twist effect. To isolate the camber effect, the cambered-twisted wing section coefficients were predicted by using the data base for the twisted wing. The results are shown in figure 20.

Significant errors between predicted and actual section C_n and $C_{m.25c}$ occur on the outboard half of the wing. Such results are clearly unsatisfactory.

Crossflow Sections

The evaluation procedure for crossflow sections was similar to that for streamwise sections. In this case, however, the net pressures were related to the leading-edge suction coefficients at the same body station (crossflow section). Plots of $C_{p,NL}$ versus $C_{s,net}$ were made for a matrix of stations and x/c locations for the three wings using the procedure shown in figure 16. Typical results for the three wings are shown in figure 21.

Experimental normal force and moment coefficients versus angle of attack for the flat, the twisted, and the cambered-twisted arrow wings are shown in figure 22 for a typical wing section that is perpendicular to the model plane of symmetry. The normal force coefficient is separated into linear and nonlinear parts; it was then plotted as a function of the square root of the predicted net leading-edge suction coefficient for that wing. In this angle-of-attack range, the leading-edge suction coefficient is essentially linear with the square of α .

We then considered the problem of predicting wing loads for the aeroelastically distorted wing. This would have to be done using experimental data for a base wing of the same planform, thickness distribution, and leading-edge radius. The linear portion of the load could be predicted for the distorted wing using a theoretical method such as FLEXSTAB. The nonlinear portion of the load would be obtained for the distorted wing from the base wing data at the appropriate leading-edge suction coefficients. The sum of these two parts is the predicted load. Figures 23 through 25 show, for nine crossflow sections, a comparison of the predicted values versus the actual test values of section C_n and C_m . Respectively, the figures show the ability to predict the effects of wing twist, camber, and combined twist and camber. The results shown in these figures are better than those shown in figures 19, 20 and 17, where the evaluation of the method using streamwise sections was shown.

Figure 26 shows the comparison of predicted section coefficients for the cambered-twisted wing to test data and theoretical predictions as a function of angle of attack. These predicted section coefficients are based on the data base for the flat wing. At an angle of attack of 12° , the associated pressure distribution at a streamwise, midspan section is shown in figure 27. Again, this approach shows very promising results.

The crossflow section correlation of local lift with theoretical leading-edge suction is a promising method for predicting the effects of aeroelastic twist and camber for an arrow wing that is in the presence of separated flow and a leading-edge vortex.

CONCLUSIONS

PRESSURES RELATED TO SECTION NORMAL FORCE

The net chordwise pressures for the flat wing and the twisted wing were virtually identical when compared at the same section normal force. This suggested the use of section normal force as a parameter to account for the effect of aeroelastic twist. However, the comparison of the twisted wing pressures and the cambered-twisted wing pressures was not nearly as good. This could be expected, since an airfoil camber change does affect the shape of the chordwise pressure distribution and as a result, affects wing torsion and aeroelastic deformation. Also, the pressure distributions were not unique with section C_n . These and other limitations led to abandoning this method in favor of using the leading-edge suction coefficient.

NONLINEAR PRESSURE INCREMENTS RELATED TO NET LEADING-EDGE SUCTION

Work performed in this contract (see refs. 18 and 19) expanded the Polhamus leading-edge suction analogy derived for sharp leading-edge wings to include the effects of leading-edge radius and of airfoil thickness and camber on the development and growth of leading-edge vortices.

STREAMWISE SECTIONS

It appeared that linking the lift nonlinearities to the local net leading-edge suction coefficient, which was calculated using FLEXSTAB theoretical pressures (see refs. 14 through 17), was the most logical and promising approach. As suggested by Polhamus, the pressure nonlinearities at a given streamwise wing section were related to the net suction at the leading edge of that same section. The loads predicted for the cambered-twisted wing, using a data base created from flat wing pressure data, did not satisfactorily match the actual loads for the cambered-twisted wing. Since the flow around an arrow wing is conical with respect to the wing apex, it appeared that relating the loads to the suction at crossflow (constant body station) sections, rather than in streamwise sections, would work better.

CROSSFLOW SECTIONS

Using this approach, the predicted pressures and resulting crossflow section lift and moments accounted well for the effects of twist change, camber change, and for the combined effect of both twist and camber when compared to measured data. These results represented a quantum improvement over pure theoretical predictions. The use of suction coefficients at crossflow sections was, therefore, selected as the best approach for using wind tunnel pressure data from a representative model to predict the load distribution on an elastic airplane in the presence of separated flows.

RECOMMENDATIONS

Further substantiation of the method using net leading-edge suction at crossflow sections for the arrow wing should be carried out. Test data are available for these evaluations at Mach numbers of 0.40 to 2.50.

The effect of moderate leading-edge deflection, regarded as local camber change, was thought to be predictable using this method; but a closer look at the discontinuities introduced at the hinge line in the theoretical FLEXSTAB pressure distribution, makes this approach doubtful. However, a continuous-curvature leading-edge deflection, like that of the mission-adaptive wing of the AFTI-111 airplane, should be a good candidate for further study.

The applicability of the method to other wing configurations is of great interest, and the AFTI-111 variable sweep wing could provide more insight in the effects of:

- wing sweep angle
- cranked leading edge

The use of far-field theory to improve the leading-edge suction calculation should be examined. The procedure would be to scale the local leading-edge suction as calculated using the FLEXSTAB pressures, so that its summation along the leading edge matches the global suction predicted by far-field theory.

Boeing Commercial Airplane Company
P.O. Box 3707
Seattle, Washington 98124
May 1982

APPENDIX A

DESCRIPTION OF DATA BASE

WIND TUNNEL MODELS

The configuration chosen for this study was a thin, low aspect-ratio, highly swept wing mounted below the centerline of a high fineness-ratio body. The general arrangement and characteristics of the model are shown in figure A-1. Two complete wings were constructed for contract NAS1-12875, one with no camber or twist and one with no camber but with a spanwise twist variation. A third wing with camber and twist was constructed for contract NAS1-14962. Deflectable control surfaces were available on all three of these wings.

FLAT WING

The mean surface of the flat wing is the wing reference plane. The nondimensional wing thickness distributions (shown in table A-1) deviate slightly from a constant for all streamwise sections to satisfy a manufacturing requirement for a finite thickness of 0.0254 cm (0.01 in.) at the trailing edge. The wing was designed with a full-span, 25-percent chord, trailing-edge control surface. Sets of fixed angle brackets allowed streamwise deflections of $\pm 4.1^\circ$, $\pm 8.3^\circ$, $\pm 17.7^\circ$, and $\pm 30.2^\circ$, as well as 0.0° . A removable full-span leading-edge control surface (15 percent of streamwise chord) could be placed in an undeflected position and also drooped 5.1° and 12.8° with fixed angle brackets. Both the leading- and trailing-edge control surfaces extended from the side of the body ($0.087 b/2$) to the wingtip and were split near midspan ($0.570 b/2$). The inboard and outboard portions of the control surfaces were able to be deflected separately and were rotated about points in the wing reference plane. An additional leading-edge control surface for this wing was constructed with a sharp (20° included angle) leading edge to examine the effects of leading-edge shape. The surface ordinates and slopes of this leading-edge segment were continuous with those of the flat wing at the leading-edge hingeline (table A-1). The sharp leading edge was smoothly faired from $0.180 b/2$ into the fixed portion of the rounded leading edge at $0.090 b/2$.

TWISTED WING

The mean surface of the twisted wing was generated by rotating the streamwise section chord lines about the 75-percent local chord points (trailing-edge control surface hingeline). The spanwise variation of twist is shown in figure A-2. The hingeline was straight and located in the wing reference plane at its inboard end ($0.087 b/2$) and 2.261 cm (0.890 in.) above the wing reference plane at the wingtip. The airfoil thickness distribution (table A-1) and the trailing-edge control surface location and available deflections were identical to those of the flat wing.

CAMBERED-TWISTED WING

The mean surface of the cambered-twisted wing was generated by superimposing a camber on the twisted-wing definition but keeping the coordinates of the leading edge and trailing edge of the cambered-twisted wing the same as those of the twisted wing.

Table A-1.—Wing Half-Thickness Distribution, Percent Chord

x/c, percent chord	0 b/2	0.09 b/2	0.20 b/2	0.35 b/2	0.50 b/2	0.65 b/2	0.80 b/2	0.93 b/2	1.00 b/2
Flat wing with rounded leading edge, twisted wing, and cambered-twisted wing									
.0000	.0000	.0000	.0000	.0000	.0000	.0000	.0000	.0000	.0000
.1250	.3359	.3359	.3359	.3359	.3360	.3360	.3360	.3362	.3364
.2500	.4506	.4506	.4506	.4506	.4507	.4507	.4508	.4509	.4512
.5000	.6064	.6064	.6064	.6064	.6065	.6065	.6066	.6068	.6072
.7500	.7247	.7247	.7247	.7248	.7248	.7248	.7250	.7253	.7258
1.0000	.8182	.8182	.8182	.8183	.8183	.8184	.8185	.8188	.8194
1.5000	.9520	.9520	.9520	.9521	.9522	.9523	.9525	.9530	.9538
2.5000	1.1191	1.1191	1.1192	1.1192	1.1194	1.1195	1.1199	1.1206	1.1219
5.0000	1.3448	1.3448	1.3449	1.3450	1.3453	1.3456	1.3462	1.3475	1.3497
8.5000	1.4809	1.4809	1.4811	1.4813	1.4816	1.4822	1.4832	1.4855	1.4892
10.0000	1.5195	1.5196	1.5197	1.5200	1.5204	1.5210	1.5222	1.5250	1.5293
12.5000	1.5444	1.5445	1.5447	1.5450	1.5456	1.5463	1.5479	1.5514	1.5568
15.0000	1.5630	1.5631	1.5634	1.5638	1.5644	1.5654	1.5673	1.5715	1.5781
17.5000	1.5720	1.5722	1.5724	1.5729	1.5737	1.5748	1.5770	1.5821	1.5898
20.0000	1.5813	1.5815	1.5818	1.5823	1.5832	1.5845	1.5871	1.5929	1.6018
30.0000	1.6214	1.6217	1.6222	1.6230	1.6242	1.6262	1.6301	1.6389	1.6522
40.0000	1.6398	1.6402	1.6408	1.6419	1.6435	1.6462	1.6514	1.6630	1.6807
45.0000	1.6282	1.6286	1.6293	1.6305	1.6324	1.6354	1.6413	1.6544	1.6742
50.0000	1.5901	1.5906	1.5914	1.5927	1.5948	1.5981	1.6046	1.6192	1.6412
60.0000	1.4344	1.4350	1.4359	1.4375	1.4400	1.4440	1.4518	1.4692	1.4956
65.0000	1.3121	1.3127	1.3137	1.3155	1.3181	1.3225	1.3310	1.3498	1.3784
70.0000	1.1627	1.1634	1.1644	1.1663	1.1692	1.1739	1.1831	1.2034	1.2341
72.5000	1.0792	1.0799	1.0810	1.0830	1.0860	1.0908	1.1003	1.1213	1.1532
75.0000	.9921	.9928	.9940	.9960	.9991	1.0041	1.0139	1.0357	1.0686
80.0000	.9006	.9013	.9025	.9046	.9078	.9129	.9231	.9456	.9796
85.0000	.8069	.8077	.8089	.8111	.8143	.8197	.8302	.8534	.8885
90.0000	.6132	.6140	.6153	.6176	.6211	.6268	.6379	.6626	.6999
95.0000	.4156	.4165	.4178	.4203	.4240	.4300	.4418	.4679	.5074
99.0000	.2153	.2162	.2177	.2202	.2241	.2305	.2430	.2706	.3122
100.0000	.0113	.0123	.0138	.0165	.0206	.0273	.0405	.0695	.1134
Sharp leading edge									
.0000	.0000	.0000	.0000	.0000	.0000	.0000	.0000	.0000	.0000
.1250	.3359	.3359	.0293	.0307	.0329	.0364	.0433	.0585	.0815
.2500	.4506	.4506	.0557	.0580	.0614	.0670	.0781	.1024	.1392
.5000	.6064	.6064	.0998	.1021	.1055	.1111	.1221	.1465	.1833
.7500	.7247	.7247	.1439	.1462	.1496	.1552	.1663	.1906	.2274
1.0000	.8182	.8182	.1880	.1903	.1937	.1993	.2103	.2347	.2715
1.5000	.9520	.9520	.2761	.2784	.2818	.2875	.2985	.3229	.3596
2.5000	1.1191	1.1191	.4524	.4547	.4581	.4638	.4748	.4992	.5359
5.0000	1.3448	1.3448	.8933	.8956	.8990	.9046	.9156	.9400	.9768
8.5000	1.4809	1.4809	1.3413	1.3429	1.3453	1.3493	1.3570	1.4001	1.4001
10.0000	1.5195	1.5196	1.4547	1.4559	1.4578	1.4609	1.4669	1.4803	1.5007
12.5000	1.5444	1.5445	1.5203	1.5210	1.5221	1.5238	1.5272	1.5347	1.5461
15.0000	1.5630	1.5631	1.5634	1.5638	1.5644	1.5654	1.5673	1.5715	1.5781

The camber is defined analytically in two parts: a typical cruise airfoil (basic) camber; and, an estimate of the aeroelastic deformation at a moderate positive angle of attack. The aeroelastic deformation was based on calculations – using a typical configuration – of deformation under load. This definition was modified slightly to provide zero camber at the model centerline so this wing would fit on the existing model body. This was achieved by using a factor k (fig. A-3) on the basic camber term, which provides a transition from no camber at the model centerline to the definition camber at $0.25 b/2$. The defined wing is smoother than indicated in this figure as section geometry was directly calculated at only those sections marked in figure A-3. The full equation for the camber is:

$$\frac{z}{c} = \left(\frac{z}{c} \right)_{\text{Basic}} + \left(\frac{z}{c} \right)_{\text{Aero}}$$

$$\left(\frac{z}{c} \right)_{\text{Basic}} = k \left(\frac{4.0}{3.0} \right) \left(0.078 + \frac{\alpha_{\text{sec}}}{57.3} \right) \left(\frac{x}{c} \right) \left(\frac{x}{c} - 1.0 \right) \left(\frac{x}{c} - 0.75 - \frac{1.0}{4.0} \left(\frac{2y}{b} \right) \right)$$

$$k = \left(\frac{2y}{b} \right) \left(1.0 + 12.0 \left(\frac{2y}{b} \right) \right) \quad \text{for } \left(\frac{2y}{b} \right) \leq 0.25$$

$$k = 1.0 \quad \text{for } \left(\frac{2y}{b} \right) \geq 0.25$$

$$\left(\frac{z}{c} \right)_{\text{Aero}} = - \frac{57.3}{3.0} \left(\frac{9.0}{4.0} \right) \left(\frac{2y}{b} \right) \left(1.0 - 0.75 \left(\frac{2y}{b} \right)^2 \right) \left(\sec \left(\frac{3.0}{57.3} \right) - \sec \left(\frac{(3.0) \left| 1.0 - 2.0 \left(\frac{x}{c} \right) \right|}{57.3} \right) \right)$$

The resulting nondimensional camber is shown in table A-2. The camber at the tip is approximately a 6° arc of a circle with the leading and trailing edges up. Sections at the root, midspan, and tip (fig. A-3) show not only the camber but the position of the sections of the cambered-twisted wing and the twisted wing relative to the wing reference plane (flat wing). The airfoil thickness distribution (table A-1) and the trailing-edge control surface location and available deflections were identical to those of the flat wing.

BODY

The body was circular in cross section and had a straight centerline. The body geometry is shown in figure A-1. The sting was an integral part of the model body.

RELATIVE WING AND BODY LOCATION

The wing reference plane was located 3.149 cm (1.240 in.) below and parallel to the body centerline (zero incidence). The apex (extension of the wing leading edge to the centerline) of the wing was located 33.496 cm (13.187 in.) aft of the model nose.

Table A-2.—Wing Section Camber Definition, Percent Chord

x/c, percent chord	0 b/2	0.09 b/2	0.20 b/2	0.35 b/2	0.50 b/2	0.65 b/2	0.80 b/2	0.93 b/2	1.00 b/2
.0000	.0000	.0000	.0000	.0000	.0000	.0000	.0000	.0000	.0000
.1250	-.0005	-.0014	.0015	.0000	-.0048	-.0076	-.0064	-.0042	-.0200
.2500	-.0005	-.0023	.0024	-.0017	-.0120	-.0177	-.0159	-.0118	-.0256
.5000	-.0005	-.0038	.0033	-.0067	-.0277	-.0394	-.0367	-.0297	-.0403
.7500	-.0005	-.0054	.0043	-.0115	-.0433	-.0608	-.0573	-.0473	-.0547
1.0000	-.0005	-.0071	.0054	-.0164	-.0591	-.0823	-.0780	-.0651	-.0695
1.5000	-.0005	-.0107	.0072	-.0263	-.0897	-.1240	-.1184	-.1003	-.0993
2.5000	-.0005	-.0174	.0080	-.0474	-.1480	-.2025	-.1946	-.1673	-.1567
5.0000	-.0005	-.0332	.0027	-.1035	-.2870	-.3878	-.3740	-.3233	-.2888
8.5000	-.0004	-.0577	-.0117	-.1876	-.4826	-.6449	-.6200	-.5312	-.4581
10.0000	-.0004	-.0695	-.0201	-.2257	-.5677	-.7552	-.7249	-.6184	-.5275
12.5000	-.0004	-.0910	-.0378	-.2922	-.7102	-.9377	-.8979	-.7613	-.6407
15.0000	-.0004	-.1139	-.0607	-.3624	-.8510	-.1.1147	-.1.0654	-.8991	-.7497
17.5000	-.0004	-.1375	-.0892	-.4359	-.9869	-.1.2823	-.1.2239	-.1.0296	-.8530
20.0000	-.0004	-.1613	-.1229	-.5115	-.1.1162	-.1.4385	-.1.3716	-.1.1511	-.9493
30.0000	-.0004	-.2542	-.2941	-.8168	-.1.5559	-.1.9432	-.1.8468	-.1.5368	-.1.2525
40.0000	-.0003	-.3359	-.4894	-.1.0939	-.1.8638	-.2.2613	-.2.1419	-.1.7666	-.1.4261
45.0000	-.0003	-.3695	-.5830	-.1.2098	-.1.9658	-.2.3531	-.2.2248	-.1.8263	-.1.4670
50.0000	-.0003	-.3968	-.6677	-.1.3048	-.2.0313	-.2.4002	-.2.2652	-.1.8504	-.1.4791
60.0000	-.0002	-.4273	-.7928	-.1.4143	-.2.0430	-.2.3551	-.2.2147	-.1.7922	-.1.4189
65.0000	-.0002	-.4275	-.8242	-.1.4182	-.1.9819	-.2.2577	-.2.1195	-.1.7074	-.1.3456
70.0000	-.0002	-.4154	-.8280	-.1.3806	-.1.8708	-.2.1068	-.1.9746	-.1.5836	-.1.2424
72.5000	-.0001	-.4041	-.8179	-.1.3444	-.1.7955	-.2.0108	-.1.8831	-.1.5068	-.1.1796
75.0000	-.0001	-.3892	-.7990	-.1.2959	-.1.7067	-.1.9008	-.1.7787	-.1.4201	-.1.1093
77.5000	-.0001	-.3704	-.7707	-.1.2344	-.1.6039	-.1.7768	-.1.6613	-.1.3235	-.1.0315
80.0000	-.0001	-.3476	-.7324	-.1.1593	-.1.4870	-.1.6386	-.1.5308	-.1.2169	-.9464
85.0000	-.0001	-.2893	-.6236	-.9864	-.1.2095	-.1.3190	-.1.2304	-.9737	-.7541
90.0000	-.0001	-.2127	-.4683	-.7126	-.8714	-.9409	-.8762	-.6903	-.5324
95.0000	-.0000	-.1166	-.2622	-.3928	-.4697	-.5021	-.4668	-.3661	-.2811
100.0000	.0000	.0000	.0000	.0000	.0000	.0000	.0000	.0000	.0000

WING FIN

The wing fin is a 3-percent biconvex airfoil placed streamwise and perpendicular to the wing reference plane on the upper surface of the cambered-twisted wing at 0.725 semispan. The dimensions of the fin and its relationship to the wing are shown in figure A-4. To obtain configurations with the outboard trailing-edge control surface deflected, the fin is extended down to touch the top of the control surface. (See fig. A-4.)

PRESSURE ORIFICE LOCATIONS

All pressure orifices were located on the left side of the model and distributed as shown in figure A-5 and tables A-3 and A-4. The flat wing with rounded leading edge, the twisted wing, and the cambered-twisted wing each had 214 orifices distributed in streamwise pressure stations of 31 (or 30) orifices at each of seven spanwise locations. One of these orifices was located at the leading edge; the remainder were distributed so that upper- and lower-surface orifices were located at the same chordwise locations. The orifice locations on the sharp leading edge were identical except for the omission of the leading-edge orifice at each spanwise station. The 83 orifices on the body were located at 15 stations along the length of the model. At each station, orifices were located at angles of 0° , 45° , 90° , 135° , and 180° measured from the top of the body. In the area of the wing-body intersection, the orifices that are nominally identified as being at 135° and 180° were located on the wing lower surface at the same lateral location as the orifices at 45° and 0° , respectively. Eight additional orifices were placed on the body, close to the juncture of the body with the wing upper surface.

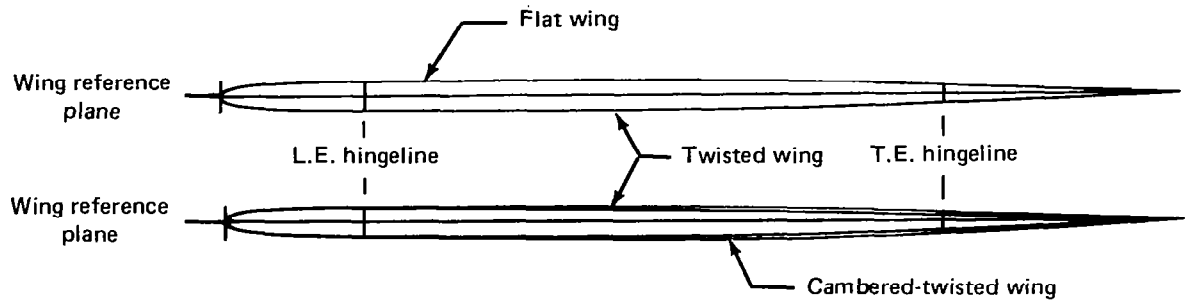
DESIGN AND CONSTRUCTION

The objectives of this study dictated that the contours and physical characteristics of the flat wing, the twisted wing, and the cambered-twisted wing be as nearly identical as possible. The model was constructed of steel to minimize aeroelastic deflections and to provide strength for testing to a Mach number of 3.0. The aft body was flared approximately 4° from 194.310 cm (76.500 in.) aft of the nose to provide the required safety factor on predicted loads (fig. A-1). The model size was selected as the best compromise between minimizing potential tunnel blockage and providing adequate room to install orifices in the model.

A computerized lofting program was used to provide the wing definition. This definition was then used to machine the model components using numerically controlled machines. The tolerance on the contour was $+0.1524$, -0.0 mm ($+0.006$, -0.0 in.). The leading- and trailing-edge control surfaces were cut from the wings after they had been machined to final contour. A cut along the 15-percent chord line of the twisted wing removed enough material to simulate the elastic characteristics of the flat wing (fig. A-6). As a result of the previous tests it was determined that it was not necessary to remove this material on the cambered-twisted wing as the wings were very rigid. Fixed angle brackets (arranged as shown in fig. A-6) were used to obtain the required control surface deflections with all pivot points located midway between the upper and lower surfaces at the hingelines. The brackets were also machined on numerically controlled machines. The same sets of trailing-edge brackets were used on all three wings, and the same sets of leading-edge brackets were used for both the rounded and sharp leading edges.

Table A-3.—Wing Pressure Orifice Locations, Percent Local Chord

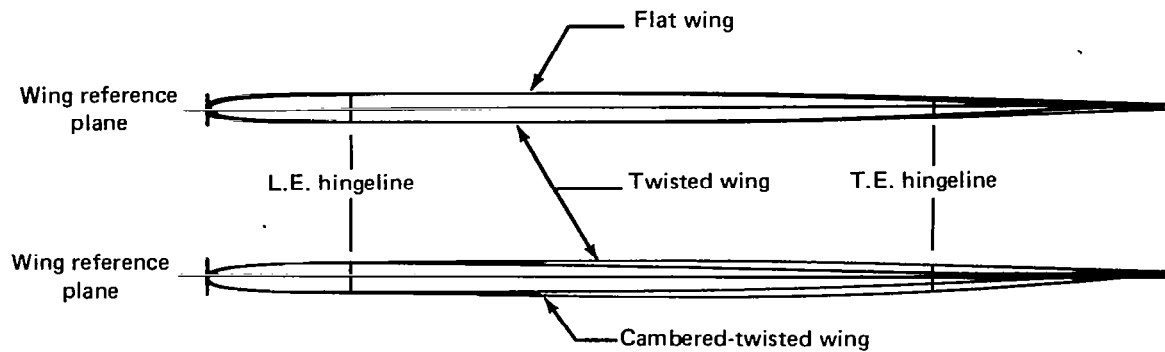
(a) Section at $0.09 \frac{b}{2}$, chord = 102.89 cm



Nominal	Flat wing, $\alpha_{\text{sec}} = 0.0^\circ$				Twisted wing, $\alpha_{\text{sec}} = -0.01^\circ$		Cambered-twisted wing, $\alpha_{\text{sec}} = -0.01^\circ$	
	Rounded leading edge		Sharp leading edge		Rounded leading edge		Rounded leading edge	
	Upper surface	Lower surface	Upper surface	Lower surface	Upper surface	Lower surface	Upper surface	Lower surface
0.00	0.00		—	—	0.00		0.00	
2.50	2.45	2.59	2.61	2.54	2.26	2.26	2.58	2.51
5.00	4.95	5.07	5.06	5.03	4.76	4.76	5.10	5.04
8.50	8.45	8.53	8.59	8.58	8.40	8.26	8.64	8.56
11.30	—	—	—	11.31	—	—	—	—
12.25	—	—	—	—	12.23	12.27	—	—
12.50	12.45	12.55	12.58	—	—	—	12.63	12.54
17.50	17.49	17.62			17.59	17.66	17.64	17.55
20.00	19.94	20.08			20.03	20.03	20.14	20.00
30.00	29.92	30.09			29.98	29.89	30.14	30.00
45.00	45.00	45.07			44.96	44.89	45.12	45.03
60.00	59.98	60.08			60.01	59.97	60.11	60.00
70.00	70.03	70.13			70.05	69.95	70.09	70.04
72.50	72.55	72.60			72.58	72.51	72.62	72.54
77.50	77.53	77.62			77.56	77.51	77.63	77.52
85.00	85.11	85.14			85.03	85.00	85.12	85.04
90.00	90.10	90.10			90.04	89.98	90.12	90.00
95.00	95.09	95.05			94.96	94.98	95.10	95.03

Table A-3.—(Continued)

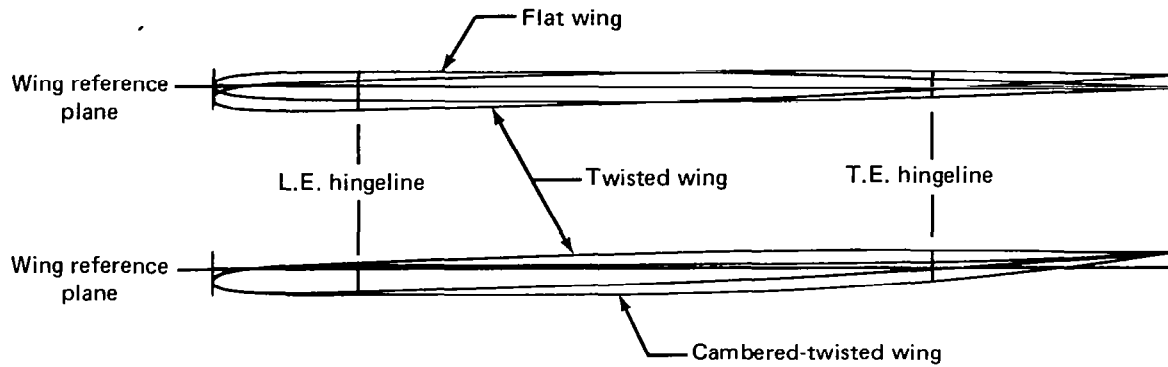
(b) Section at $0.20 \frac{b}{2}$, chord = 91.80 cm



Nominal	Flat wing, $\alpha_{\text{sec}} = 0.0^\circ$				Twisted wing, $\alpha_{\text{sec}} = -0.47^\circ$		Cambered-twisted wing, $\alpha_{\text{sec}} = -0.47^\circ$	
	Rounded leading edge		Sharp leading edge		Rounded leading edge		Rounded leading edge	
	Upper surface	Lower surface	Upper surface	Lower surface	Upper surface	Lower surface	Upper surface	Lower surface
0.00	0.00		—	—	0.00		0.00	
2.50	2.59	2.69	2.62	2.65	2.52	2.42	2.63	2.59
5.00	5.05	5.00	5.14	5.14	5.00	4.93	5.09	5.05
8.50	8.54	8.59	8.67	8.62	8.52	8.40	8.61	8.64
11.40	—	—	—	11.37	—	—	—	—
12.50	12.54	12.49	12.63	—	12.53	12.42	12.51	12.62
17.50	17.63	17.61			17.65	17.52	17.59	17.63
20.00	20.08	20.07			20.00	19.90	19.95	20.05
30.00	30.04	30.09			30.02	29.89	30.05	29.97
45.00	45.08	45.09			45.03	44.92	45.04	45.01
60.00	60.02	60.13			60.03	59.91	60.02	60.06
70.00	70.11	70.13			70.06	69.96	70.03	70.01
72.50	72.63	72.61			72.55	72.50	72.59	72.67
77.50	77.59	77.65			77.59	77.52	77.53	77.57
85.00	85.07	85.13			85.02	85.00	85.09	85.10
90.00	90.14	90.11			90.07	89.97	90.04	89.98
95.00	95.14	95.10			95.05	95.08	95.06	94.98

Table A-3.—(Continued)

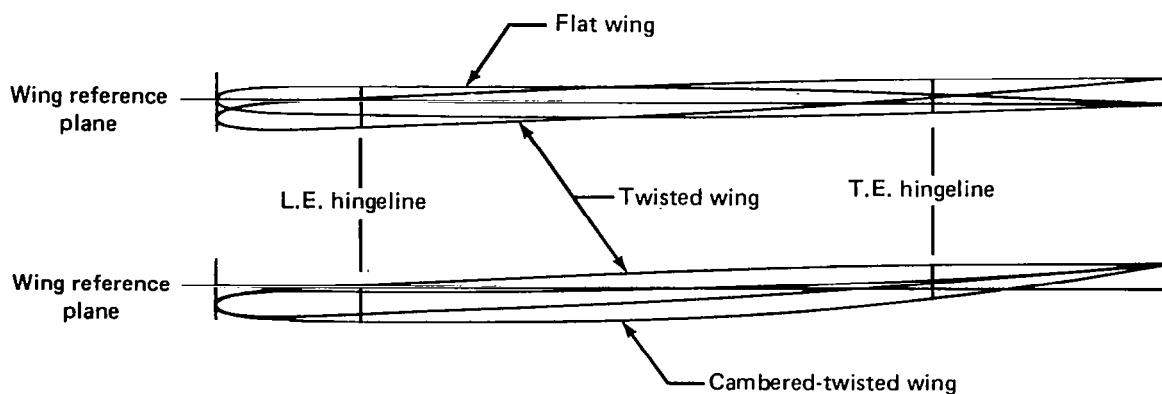
(c) Section at $0.35 \frac{b}{2}$, chord = 76.69 cm



Nominal	Flat wing, $\alpha_{\text{sec}} = 0.0^\circ$				Twisted wing, $\alpha_{\text{sec}} = -1.70^\circ$		Cambered-twisted wing, $\alpha_{\text{sec}} = -1.70^\circ$	
	Rounded leading edge		Sharp leading edge		Rounded leading edge		Rounded leading edge	
	Upper surface	Lower surface	Upper surface	Lower surface	Upper surface	Lower surface	Upper surface	Lower surface
0.00	0.00		—	—	0.00		0.00	
2.50	2.45	2.59	2.59	2.58	2.39	2.33	2.76	2.60
5.00	4.93	5.07	5.11	5.04	5.12	4.78	5.05	5.10
8.50	8.60	8.54	8.65	8.63	8.49	8.32	8.68	8.70
10.50	—	—	—	10.46	—	—	—	—
11.00	—	11.03	—	—	—	—	—	—
12.50	12.37	—	12.57	—	12.50	12.33	12.59	12.68
17.50	17.64	17.63			17.54	17.53	17.64	17.62
20.00	20.00	20.09			19.94	19.84	20.03	20.07
30.00	30.01	30.10			29.88	29.87	30.00	29.93
45.00	44.99	45.09			44.96	44.79	45.00	45.13
60.00	60.03	60.08			59.97	59.89	60.00	60.10
70.00	70.07	70.08			70.03	69.90	70.04	70.03
72.50	72.55	72.58			72.56	72.44	72.61	72.52
77.50	77.60	77.61			77.54	77.51	77.50	77.60
85.00	85.11	85.14			85.08	84.96	85.09	84.93
90.00	90.06	90.09			89.89	89.89	89.98	90.04
95.00	95.07	95.09			94.95	94.86	94.98	95.10

Table A-3.—(Continued)

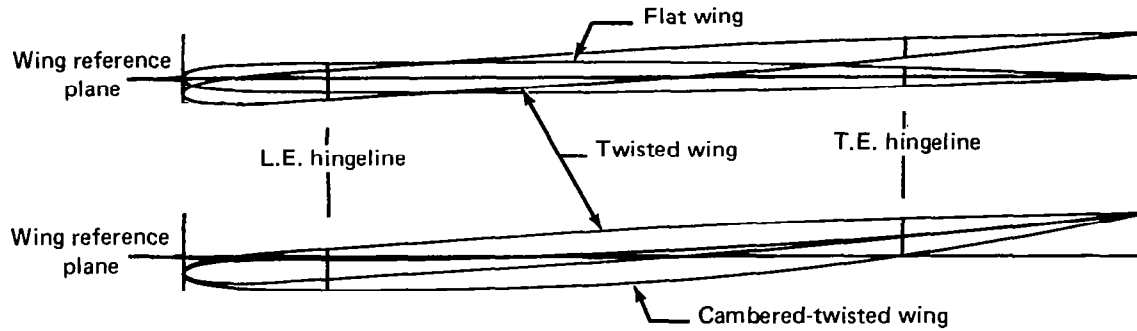
(d) Section at $0.50 \frac{b}{2}$, chord = 61.57 cm



Nominal	Flat wing, $\alpha_{\text{sec}} = 0.0^\circ$				Twisted wing, $\alpha_{\text{sec}} = -2.85^\circ$		Cambered-twisted wing, $\alpha_{\text{sec}} = -2.85^\circ$	
	Rounded leading edge		Sharp leading edge		Rounded leading edge		Rounded leading edge	
	Upper surface	Lower surface	Upper surface	Lower surface	Upper surface	Lower surface	Upper surface	Lower surface
0.00	0.00		—	—	0.00		0.00	
2.50	2.47	2.53	2.69	2.60	2.44	2.38	2.78	2.62
5.00	4.99	4.95	5.13	5.06	4.92	4.80	5.13	5.15
8.50	8.48	8.38	8.66	8.61	8.46	8.38	8.64	8.56
10.10	—	—	—	10.14	—	—	—	—
11.10	—	11.08	—	—	—	—	—	—
12.50	12.39	—	12.61	—	12.50	12.31	12.71	12.55
17.50	17.64	17.52			17.54	17.24	17.71	17.44
20.00	19.98	19.97			19.92	19.83	20.15	19.89
30.00	30.07	30.06			29.91	29.85	30.04	29.72
45.00	44.98	45.06			45.00	44.85	44.95	44.97
60.00	59.97	60.00			59.95	59.92	59.96	59.94
70.00	70.07	70.10			70.03	69.88	69.93	69.86
72.50	72.65	72.61			72.56	72.44	72.53	72.34
77.50	77.66	77.65			77.61	77.43	77.58	77.43
85.00	85.19	85.18			84.85	84.90	84.96	84.92
90.00	90.22	90.12			89.93	89.93	89.94	89.91
95.00	95.05	94.94			94.88	94.93	94.98	94.88

Table A-3.—(Continued)

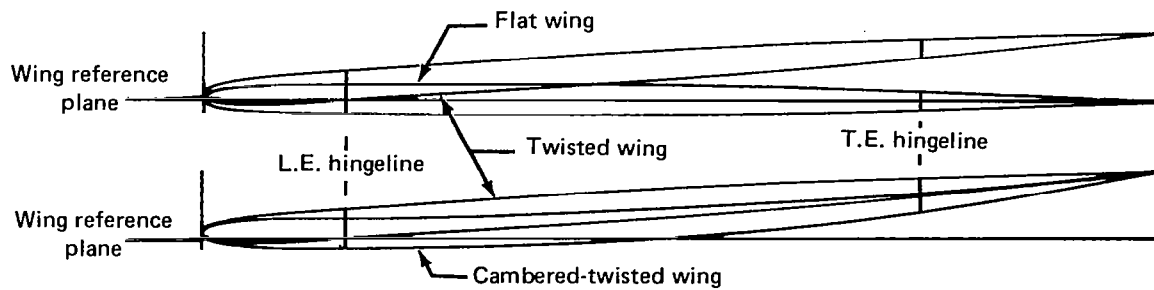
(e) Section at $0.65\frac{b}{2}$, chord = 46.46 cm



Nominal	Flat wing, $\alpha_{\text{sec}} = 0.0^\circ$				Twisted wing, $\alpha_{\text{sec}} = -3.59^\circ$		Cambered-twisted wing, $\alpha_{\text{sec}} = -3.59^\circ$	
	Rounded leading edge		Sharp leading edge		Rounded leading edge		Rounded leading edge	
	Upper surface	Lower surface	Upper surface	Lower surface	Upper surface	Lower surface	Upper surface	Lower surface
0.00	0.00		—	—	0.00		0.00	
2.50	2.56	2.66	2.49	2.38	2.18	2.49	2.76	2.79
5.00	5.06	5.12	4.94	4.95	4.76	5.01	5.35	5.40
8.50	8.55	8.55	8.46	8.40	8.32	8.45	8.85	8.74
12.20	—	—	12.12	—	12.21	—	—	—
12.60	12.57	—	—	—	—	—	12.71	12.77
17.50	17.60	17.65			17.24	17.44	17.74	17.58
20.00	20.17	20.11			19.70	19.88	20.19	19.96
30.00	30.05	30.11			30.26	29.73	30.13	29.85
45.00	45.16	45.23			44.75	44.89	45.03	44.75
60.00	60.13	60.13			59.81	59.87	60.02	59.99
70.00	69.89	70.12			69.92	69.90	70.09	69.88
72.50	72.59	72.69			72.38	72.49	72.83	72.15
77.50	77.74	77.76			77.22	77.49	77.56	77.43
85.00	85.25	85.32			84.79	84.93	84.93	84.76
90.00	90.22	90.21			89.70	89.92	89.95	89.98
95.00	95.13	95.27			95.12	94.86	94.97	94.98

Table A-3.—(Continued)

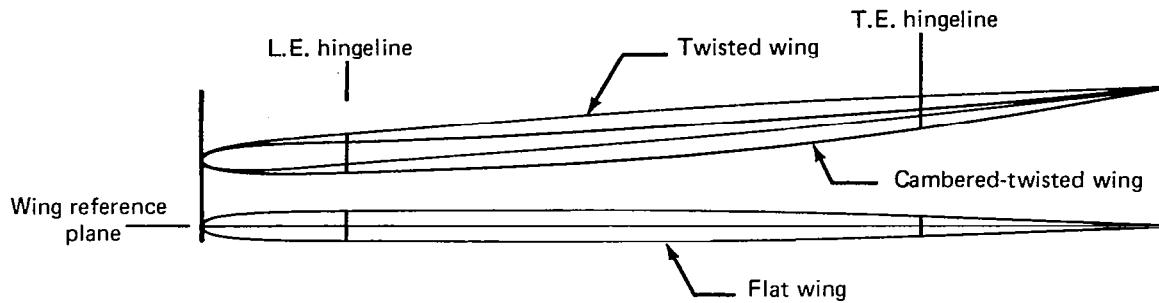
(f) Section at $0.80 \frac{b}{2}$, chord = 31.35 cm



Nominal	Flat wing, $\alpha_{\text{sec}} = 0.0^\circ$				Twisted wing, $\alpha_{\text{sec}} = -3.84^\circ$		Cambered-twisted wing, $\alpha_{\text{sec}} = -3.84^\circ$	
	Rounded leading edge		Sharp leading edge		Rounded leading edge		Rounded leading edge	
	Upper surface	Lower surface	Upper surface	Lower surface	Upper surface	Lower surface	Upper surface	Lower surface
0.00	0.00		—	—	0.00		0.00	
2.50	2.55	2.47	2.50	2.46	2.33	2.43	2.76	2.62
5.00	5.01	5.02	5.01	4.93	4.86	4.74	5.27	5.21
8.50	8.55	8.59	8.58	8.41	8.32	—	8.78	8.54
12.50	12.50	—	12.58	—	12.47	12.43	12.69	12.58
17.50	17.53	17.57			17.36	17.47	17.83	17.34
20.00	20.16	20.13			19.79	19.82	20.11	19.79
30.00	30.00	30.11			29.83	29.83	30.15	29.48
45.00	44.91	45.15			44.81	44.91	44.81	44.75
60.00	59.94	60.10			59.80	59.92	59.84	59.79
70.00	70.06	70.11			69.89	69.87	69.77	69.94
72.50	72.61	72.60			72.22	72.39	72.50	72.33
77.50	77.73	77.72			77.29	77.41	77.22	77.40
85.00	85.25	85.18			84.80	84.95	84.92	84.92
90.00	90.20	90.34			90.62	90.03	90.19	90.09
95.00	95.41	95.49			95.71	95.00	95.05	94.94

Table A-3.—(Concluded)

(g) Section at $0.93 \frac{b}{2}$, chord = 18.25 cm



Nomina	Flat wing, $\alpha_{\text{sec}} = 0.0^\circ$				Twisted wing, $\alpha_{\text{sec}} = -4.14^\circ$		Cambered-twisted wing, $\alpha_{\text{sec}} = -4.14^\circ$	
	Rounded leading edge		Sharp leading edge		Rounded leading edge		Rounded leading edge	
	Upper surface	Lower surface	Upper surface	Lower surface	Upper surface	Lower surface	Upper surface	Lower surface
0.00	0.00		—	—	0.00		0.00	
2.51	1.70	1.81	2.12	1.86	1.74	2.59	2.77	2.26
5.00	4.38	4.68	4.72	4.52	4.41	4.65	5.11	4.79
8.50	7.89	8.24	8.21	8.06	7.92	8.23	8.64	8.13
11.59	—	—	—	—	11.59	—	—	—
12.25	12.33	—	12.19	—	—	—	12.64	12.16
17.50	17.36	16.60			16.60	17.49	18.03	16.83
20.00	19.78	19.81			19.58	19.96	19.94	19.44
30.00	29.67	29.00			29.17	29.62	30.22	28.66
45.00	44.70	44.80			44.12	44.44	44.33	44.77
60.00	59.68	59.47			59.18	59.71	59.47	59.38
70.00	69.69	70.33			68.99	69.31	69.10	70.07
72.50	72.15	71.89			71.59	72.01	71.78	72.74
77.50	77.38	77.31			76.80	77.12	76.49	77.36
85.00	84.62	84.90			84.54	84.82	84.93	85.29
90.00	89.51	89.81			89.21	89.74	90.72	90.35
95.00	94.46	94.68			94.41	94.56	95.26	94.87

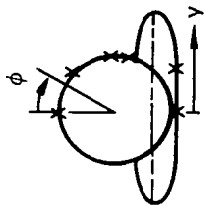


Table A-4.—Body Pressure Orifice Locations

x/L, percent body length															
Nominal locations	4.5	7.5	11.0	14.5	21.8	25.0	33.0	39.0	50.0	55.0	60.0	64.0	70.0	75.5	80.0
$\phi = 0.0^\circ$	0.0	0.0	0.0	0.0	0.0	0.0	0.0	0.0	0.0*	0.0*	0.0*	0.0	0.0	0.0	0.0
$\phi = 45.0^\circ$	44.3	44.3	44.5	44.7	44.4	44.8	45.0	44.8	45.0	44.8	44.8	45.0	44.8	45.0	44.8
$\phi = 90.0^\circ$	90.0	89.9	90.5	90.3	90.4	89.9	90.1	90.2	90.2	90.0	89.9	89.9	89.8	90.1	89.8
$\phi \approx 110.0^\circ$	---	---	---	---	110.2	110.0	110.1	110.1	110.2	116.8	119.9	124.2	---	---	---
Body, $\phi = 135.0^\circ$ Flat wing, $y = 3.094$ cm Twisted wing, $y = 3.094$ cm Cambered-twisted wing, $y = 3.094$ cm	136.1	135.3	135.0	135.2	3.025 3.132 3.040	3.028 3.106 3.056	3.028 3.048 3.075	3.056 3.048 3.072	3.071 3.005 3.079	3.056 2.926 3.067	3.043 3.094 3.084	3.045 3.094 3.069	134.6	134.5	134.8
Body, $\phi = 180.0^\circ$ Flat wing, $y = 0.0$ cm Twisted wing, $y = 0.0$ cm Cambered-twisted wing, $y = 0.0$ cm	180.0	180.0	180.0	180.0	-.018 .020 -.046	-.030 -.008 -.060	-.064 -.041 -.027	.081 -.043 .002	-.048 -.056 -.032	180.0*	180.0*	180.0	180.0	180.0	180.0

*For the first 149 runs of the first test in the BTWT, pressure readings at these orifices did not always stabilize.

Pressure tubing used in this model was 1.016 mm (0.040 in.) o.d. Monel with a 0.1524 mm (0.006 in.) wall thickness. The major channels for wing pressure tubing were machined into the surface. The detailed grooves required to route tubing from the orifices to these channels were cut by hand. The pressure orifices were installed normal to and flush with the local surface. After installation of the pressure tubing, the grooves were filled with solder and brought back to contour by hand-filing to match templates prepared by numerically controlled machining.

Quick disconnects were used at the wing-body junction to reduce the time required for installing a different wing. Unfortunately, by the time the cambered-twisted wing was installed in the test section, one quick-disconnect block had become worn out due to the two previous tests and model checkout. The connection did not seal properly and measurements at a series of orifices (x/c from 0.125 through 0.600) on the lower surface at $0.80 b/2$ were not sufficiently accurate to be used. Data values to be used in the integration were obtained by linear spanwise interpolation between adjacent sections.

The tubing for body pressure orifices was run through the hollow center of the model body rather than running it in grooves in the outside contour. Tubing from all the orifices was routed through the hollow body to the scanivalves located in the body nose. Wiring from the scanivalves was routed through the body to the sting.

The nose portion of the body was removable to provide access to the fifteen 24-position scanivalves. Figure A-1 shows the aft body location of the strain gages that were used to measure normal force and pitching moment.

PRESSURE INSTRUMENTATION

The model was instrumented with fifteen 24-position scanivalves. Each scanivalve contained a 103.42-kN/m^2 (15-psi) differential Statham, variable resistance, unbonded strain gage transducer. These transducers are calibrated against a high accuracy standard and, if placed in a temperature-controlled environment, will read within an accuracy of 0.1 percent of full scale. The transducers were located inside the model and subjected to large temperature excursions. During testing in the Boeing Transonic Wind Tunnel (BTWT), temperatures recorded at the scanivalves indicated that the accuracy of the readout was 0.75 percent of full-scale capability based on the calibration data. For tests in the 9- by 7-ft supersonic leg of the NASA Ames Unitary Wind Tunnel, the accuracy of pressure measurements was better than ± 0.3 percent, based on the maximum temperature measured in the test section.

During the first test in the BTWT (NAS1-12875), two problems were encountered. For the first 149 runs, the data filter for one of the scanivalves was inadvertently set at too low of a cutoff frequency. This caused a lag that affected five body pressure measurements, which produced a maximum error of approximately 0.684 kN/m^2 (0.1 psi) at an angle of attack of 16° and $M = 0.95$. Table A-4 identifies the specific data affected. During the first half (approximately) of the test, the scanivalve that recorded lower surface pressures between the hingelines for the sections at $2y/b = 0.09, 0.20, 0.35$, and 0.50 was intermittent at an angle of attack of 16° . This problem was eventually traced to an electrical problem in the strut. Rather than sacrifice all of these data, the incorrect measurements were replaced by extrapolating the data from angles of attack of 12° and 14° .

In the second test in the BTWT (NAS1-14962), damage to one of the quick disconnects for the wing caused the loss of measurements at a series of orifices (x/c from 0.125 through 0.600) on the lower surface at 0.80 b/2. Replacement values were obtained by a linear-spanwise interpolation between the adjacent sections.

WIND TUNNEL FACILITIES AND CAPABILITIES

The majority of testing (NASA contracts NAS1-12875 and NAS1-14962) of this model was conducted in the Boeing Transonic Wind Tunnel (BTWT). There was also limited testing (NASA contract NAS1-14141) of the flat and twisted wings in the 9- by 7-ft supersonic leg of the NASA Ames Unitary Wind Tunnel. These two facilities are described in some detail.

BOEING TRANSONIC WIND TUNNEL (BTWT)

The BTWT is a continuous-flow, closed-circuit, single-return facility with an operating range of Mach number from 0.0 to nearly 1.1. The test section is 2.438 by 3.658 by 4.420 m (8 by 12 by 14.5 ft) with 11.0 percent of the wall area in slots.

The tunnel layout is shown in figure A-7. The tunnel stagnation pressure is atmospheric with a total temperature range of 300 K to 356 K (540° to 640° R). The variation with Mach number of Reynolds number based on the mean aerodynamic chord (M.A.C.) of this model is shown in figure A-8., which also shows the variation of dynamic pressure with Mach number. The 26 856-kW (36 000-hp) wound-rotor induction motor in tandem with a 13 428-kW (18 000-hp) synchronous motor provides the power to drive a 7.315-m (24-ft) diameter fan up to a maximum speed of 470 rpm. The fan is made up of a 5.486-m (18-ft) diameter hub with 72 fixed-pitch fiberglass blades 0.914 m (36 in.) long in two stages and directs circuit air through two stages of 67 hollow steel stators.

Data System

The BTWT data system provides the capabilities of real-time test data acquisition, feedback control computation, and display. The data system consists of an Astrodata acquisition subsystem and a computing subsystem that uses a Xerox data system (XDS 9300) digital computer. The Astrodata system acquires signals from the sensors, conditions them, and passes them directly to the computer. Test data (averaged from as many as 256 samples per test point) are recorded on a rapid-access data drum. As final computations are performed, selected on-line displays are provided on analog X-Y plotters and teletypewriters. Real-time computations and displays are performed every 200 milliseconds for control and test monitoring functions. Any test data may be retrieved from rapid-access drum storage and displayed on an oscilloscope. On-line programs also provide for the preparation of magnetic tapes for plotting or interfacing with off-line programs. Figure A-9 is a schematic of the data acquisition and reduction system.

Mach Number

Mach number in the BTWT is referenced to the horizontal and lateral center of the test section at tunnel station 1000, which was the pitch point of this model (40-percent M.A.C.).

The pressures used in determining the Mach number, p_s , and p_t are measured through permanently positioned sensors. Static pressure p_s is measured by a 103.42-kN/m² (15-psi) absolute transducer. A 103.42-kN/m² (15-psi) differential transducer is used to obtain total pressure by measuring $(p_t - p_s)$. These transducers are temperature compensated in addition to being in a $\pm 1.11^\circ\text{C}$ ($\pm 2^\circ\text{F}$) environment. Transducer performance is checked periodically, and both the static and differential transducers have shown a maximum deviation of ± 0.02 percent of full scale.

The static pressure tap is located out of the test section above the ceiling in the pressure cap plenum. A correction is made to adjust this static pressure reading to the measured test-section-centerline static pressure determined during calibrations at station 1000. The tunnel total pressure is obtained from a total pressure probe mounted near the tunnel ceiling in the bellmouth throat (fig. A-7).

Signals from the pressure sensors are fed to the XDS 9300 computer. The XDS system computes and updates the Mach display five times per second. Accounting for the entire system, calculated Mach number is accurate within ± 0.002 . Data are recorded only when the tunnel is within a preselected Mach tolerance. For this test, a tolerance of ± 0.003 was used.

Dynamic Pressure

The dynamic pressure q is computed from the Mach number and the corrected static pressure. The estimated tolerance on dynamic pressure is $\pm 95.8\text{ N/m}^2$ ($\pm 2.0\text{ psf}$).

Angle of Attack

The angle of attack of the reference point (0.25 M.A.C. for this model) for a sting-mounted model is a combination of the input angle measured at the base of the sting and several incremental corrections. The input angle of attack is determined by an encoder mounted in the strut. This angle is accurate within $\pm 0.02^\circ$. This angle is then modified by the effects of sting deflection, up-flow, and wall corrections.

Sting deflections due to load were determined during the calibrations of the strain gages, which are mounted on the integral sting body of the model. These deflections are known within $\pm 0.02^\circ$. The corrections for sting deflection are based on the normal force and pitching moment loads obtained during wind-on data acquisition. The sting deflection was taken into account when setting test angles of attack, to minimize the variation in final angle of attack for the various model configurations. The strain gages attached to the sting body of this model have an estimated accuracy of ± 5 percent of full-scale reading. This means that the sting deflections based on maximum model loads were known within $\pm 0.11^\circ$.

During run 55 of the second test in the BTWT, the wiring for the pitching moment gage broke, affecting both the normal force and pitching moment measurements and, therefore, the calculation of sting deflection under load. For the remainder of that test, the model angle was set using the angle of attack as determined by the encoder for the most similar previously run configuration. After the test, the normal force and pitching moment obtained by integrating the pressure data were used to correct the final angle of attack. To verify this procedure, a comparison of these two methods was made using data obtained prior to run 55; the results matched within $\pm 0.01^\circ$.

Up-flow corrections were made based on data obtained from upright and inverted runs on a calibration model of similar span. These corrections were less than 0.2° . It is generally accepted that the up-flow values are known within $\pm 0.05^\circ$.

A correction to model angle was made for the effect of lift interference for 11-percent slotted walls. The lift interference is a function of the ratio of model-to-test section size, test section shape, C_N , and wall geometry. For $C_N = 1.0$, this correction is on the order of -0.48° . Due to the limited amount of experimental substantiation, the wall correction could be in error by ± 20 percent.

NASA AMES UNITARY WIND TUNNEL, 9- BY 7-FT SUPERSONIC LEG

The 9- by 7-ft supersonic leg of the NASA Ames Unitary Wind Tunnel is a continuous-flow, closed-return, variable-density facility with an operating range of Mach number from 1.54 to 2.50. (A schematic is shown in fig. A-10.) The tunnel is equipped with an asymmetrical sliding-block nozzle and a flexible upper plate; variation of the test section Mach number is achieved by translating, in the streamwise direction, the fixed-contour block that forms the floor of the nozzle. For this test, the Reynolds number was selected as 8.65×10^6 based on the mean aerodynamic chord (\bar{c}) of this model. The test section is 2.74 by 2.13 by 5.49 m (9 by 7 by 18 ft).

The tunnel air is driven by an 11-stage axial-flow compressor that is powered by four variable-speed, wound-rotor induction motors with a combined output of 134 280 kW (180 000 hp). Four 850 m^3 (30 000 ft^3) spherical storage tanks provide dry air for tunnel pressurization. The temperature is controlled by aftercooling.

Data System

The data acquisition system is comprised of a Beckman 210 analog-digital recorder and a minicomputer. Output from the Beckman 210 is converted to an acceptable format and transmitted by the minicomputer to an IBM 360 computer, which is located in the AMES Research Center central computer facility for the processing and preparation of final data. This flow is illustrated in figure A-11.

Angle of Attack

The angle of attack of the reference point (0.25 M.A.C. for this model) for a sting-mounted model is a combination of the input angle at the base of the sting and an increment due to sting deflection. The input angle of attack at the base of the sting is accurate within 0.02° .

Sting deflections due to load were determined during the calibration of the strain gages mounted on the integral sting body of the model. The corrections for sting deflection are based on the normal force and pitching moment loads obtained during wind-on data acquisition. The sting deflection was taken into account when setting test angles of attack to minimize the variation in final angle of attack for the various model configurations. Only a crude calibration of the normal force and pitching moment gages was obtained since the force and pitching moment measurements were used primarily for calculating sting deflection. Comparison with the integrated pressure results indicates that both force and moment measurements may be about 10 percent low, which could yield a maximum error in final angle of attack of 0.1° .

TESTS AND DATA ACQUISITION

BOEING TRANSONIC WIND TUNNEL (BTWT)

Tests

As previously stated, tests were conducted in the BTWT under two NASA contracts. Table A-5 shows the 54 configurations that were tested under contract NAS1-12875. The 12 configurations tested under contract NAS1-14962 are shown in table A-6. Two of the configurations were included in both tests to ensure that data from the two tests are consistent. Photographs of some of the configurations are shown in figures A-12 through A-15; a diagram of the model installation in the BTWT is shown in figure A-16.

Pressure and total force data were obtained at Mach numbers of 0.40, 0.85, 0.95, and 1.05 for all configurations and at Mach numbers of 0.70, 1.00, and 1.11 for selected configurations. Test angles of attack were from -8° to $+16^\circ$ in 2° increments, however, not all angles of attack were included for all configurations and/or Mach numbers. Tables A-5 and A-6 show the run numbers for each Mach number and configuration for which these data were obtained.

During the first test, wingtip deflection pictures were taken for representative configurations at three Mach numbers to evaluate the stiffness of the wing. These were compared to wind-off reference pictures to determine the relative deflection and twist. Configurations included the flat and twisted wings, and trailing-edge control surfaces deflected $+30.2^\circ$, 0.0° , and -17.7° . Whereas the tip did deflect (less than 2 cm), the change in incidence was negligible even at $M = 1.05$; and, due to model flexibility, no corrections to the data were required.

Data Repeatability

Comparisons of data from both tests (NASA CR-165701), show that the data are within the tolerances expected for repeat runs during a single test. Therefore, data from both tests are compared without regard to the test in which the data were obtained.

Data Acquisition and Initial Processing

The pressure data were recorded through the use of fifteen 24-position scanivalves located in the fore body of the model. Pressure transducers in the scanivalves measured the differential pressure between the local surface pressures and tunnel total pressure. Signals from the scanivalves, force and moment data, tunnel parameters, and model attitude angle were recorded on the Astrodata system and reduced using the XDS 9300 computer.

NASA AMES UNITARY WIND TUNNEL, 9- BY 7-FT SUPERSONIC LEG

Tests

Table A-7 lists the 13 configurations that were tested. Photographs of two of these are shown in figures A-17 and A-18; a diagram of the model installation in the test section is shown in figure A-19. Pressure and total force data were obtained at Mach numbers of 1.70, 2.10 and 2.50 for all configurations. Table A-7 shows the run numbers for each Mach number and configuration for which these data were obtained. Test angles of attack were from -8° to $+14^\circ$ in 2° increments and $+15^\circ$.

Table A-5.—Summary of Subsonic/Transonic Test Conditions by Run Number
(NASA Contract NAS1-12875)

Leading-edge deflection, deg	Mach. no.	Trailing-edge deflection, deg															
		Full span								Outboard (inboard = 0.0)							
		30.2	17.7	8.3	4.1	0.0	-4.1	-8.3	-17.7	-30.2	17.7	8.3	-8.3	-17.7	17.7	8.3	Inboard (outboard = 0.0)
		Flat wing, rounded leading edge, trip strip off															
Full span = 0.0	0.40																
	0.70					10											
	0.85					15											
	0.95					7											
	1.05					16											
	1.11					14											
					9												
Flat wing, rounded leading edge, trip strip on																	
Full span = 0.0	0.40	37	32	46	48	21,269	55	78	66	75	280	275		252	259		
	0.70	34	29	43	50	23,263	57	80	63	72	277	271		248	255		
	0.85	36	31	45	52	25,267	59	82	65, 69	74	279	274		250	258		
	0.95	35	30	44	51	24,266	58	81	64, 68	73	278	273		249	257		
	1.00					268											
	1.05	33	28	42	49	22,264	56	79	62	71	276	272		247	256		
	1.11			40	47	20,262	54	77				270		254	254		
Inboard = 0.0 Outboard = 5.1	0.40					223					215	209	196	202	246	241	229
	0.70					218					211	205	192	198	243	237	228
	0.85					221					214	208	195	201	245	240	227
	0.95					220					213	207	194	200	244	239	226
	1.05					219					212	206	193	199	242	238	224
	1.11					217					210	204	191	197	236	230	224

Table A-5. — (Continued)

Leading-edge deflection, deg	Mach no.	Trailing-edge deflection, deg																
		Full span							Outboard (inboard = 0.0)									
		30.2	17.7	8.3	4.1	0.0	-4.1	-8.3	-17.7	-30.2	17.7	8.3	-8.3	-17.7	17.7	8.3	-8.3	-17.7
		Flat wing, rounded leading edge, trip strip on																
Inboard = 5.1 Outboard = 0.0	0.40																	
	0.70																	
	0.85																	
	0.95																	
	1.05																	
	1.11																	
Full span = 5.1	0.40		177	149	138	183												
	0.70		173	145	140	179												
	0.85		175	148	142	182												
	0.95		174	147	141	181												
	1.05		172	146	139	180												
	1.11			144	137	178												
Full span = 12.8	0.40		118	115	109	98												
	0.70		121	112	105	100												
	0.85		123	114	108	102												
	0.95		122	113	107	101												
	1.05		120	111	106	99												
	1.11		116		104	97												

Table A-5.—(Concluded)

Leading-edge deflection, deg	Mach no.	Trailing-edge deflection, deg																
		Full span								Outboard (inboard = 0.0)								
		30.2	17.7	8.3	4.1	0.0	-4.1	-8.3	-17.7	-30.2	17.7	8.3	-8.3	-17.7	17.7	8.3	-8.3	-17.7
Flat wing, sharp leading edge, trip strip on																		
Full span=0.0	0.40																	
	0.70																	
	0.85																	
	0.95																	
	1.00																	
	1.05																	
	1.11																	
Flat wing, twisted trailing edge, rounded leading edge, trip strip on																		
Full span=0.0	0.40																	
	0.70																	
	0.85																	
	0.95																	
	1.05																	
	1.11																	
Twisted wing, rounded leading edge, trip strip on																		
Full span=0.0	0.40	427	422	416	411	450		435	442									
	0.70	424	419	413	408	445		432	439									
	0.85	426	421	415	410	449		434	441									
	0.95	425	420	414	409	447		433	440									
	1.00					448												
	1.05	423	418	412	407	446		431	438									
	1.10				444													

*Table A-6.—Summary of Subsonic/Transonic Test Conditions by Run Number
(NASA Contract NAS1-14962)*

Mach number	Trailing-edge deflection, degrees			
	Full span		Outboard (inbd=0.0)	Inboard (outbd=0.0)
	0.0	8.3	8.3	8.3
Twisted wing				
0.40	15	25	30	20
0.70	14	24	29	19
0.85	13	23	28	18
0.95	12	22	27	17
1.00	11			
1.05	10	21	26	16
Cambered-twisted wing, fin off				
0.40	43	65	80	57
0.70	41			
0.85	40	62	78	59
0.95	39	64	79	58
1.00	38			
1.05	37	61	77	55
Cambered-twisted wing, fin on				
0.40	49	70	75	54
0.70	45			
0.85	48	68	73	52
0.95	47	69	74	53
1.00	46			
1.05	44	67	72	51

Table A-7.--Summary of Supersonic Test Conditions by Run Number. Reynolds Number = 8.65×10^6
(NASA Contract NAS1-14141)

Leading-edge deflection, deg	Mach no.	Trailing-edge deflection, deg							
		Full span				Outboard (inboard = 0.0)			
		8.3	4.1	0.0	-4.1	8.3	4.1	8.3	4.1
Flat wing, rounded L.E.									
Full span = 0.0	1.543			19					
	1.70	26	37	20	44	23	40	30	34
	2.10	27	38	21	45	24	41	31	35
	2.50	28	39	22	46	25	42	32	36
Full span = 5.1	1.70			16					
	2.10			17					
	2.50			18					
Flat wing, sharp L.E.									
Full span = 0.0	1.70			51					
	2.10			52					
	2.50			53					
Full span = 5.1	1.70			48					
	2.10			49					
	2.50			50					
Twisted wing, rounded L.E.									
Full span = 0.0	1.60			1					
	1.70	11		3					
	1.90			4, 6					
	2.10	12		9					
	2.50	13		10					

Data Acquisition and Initial Processing

The pressure data were recorded through the use of fifteen 24-position scanivalves located in the fore body of the model. Pressure transducers in the scanivalves measured the differential pressure between the local surface pressures and a known reference pressure. Signals from the scanivalves, force and moment data, tunnel parameters, and model attitude angle were recorded on the Beckman 210 analog-digital recorder and reduced by the Ames staff.

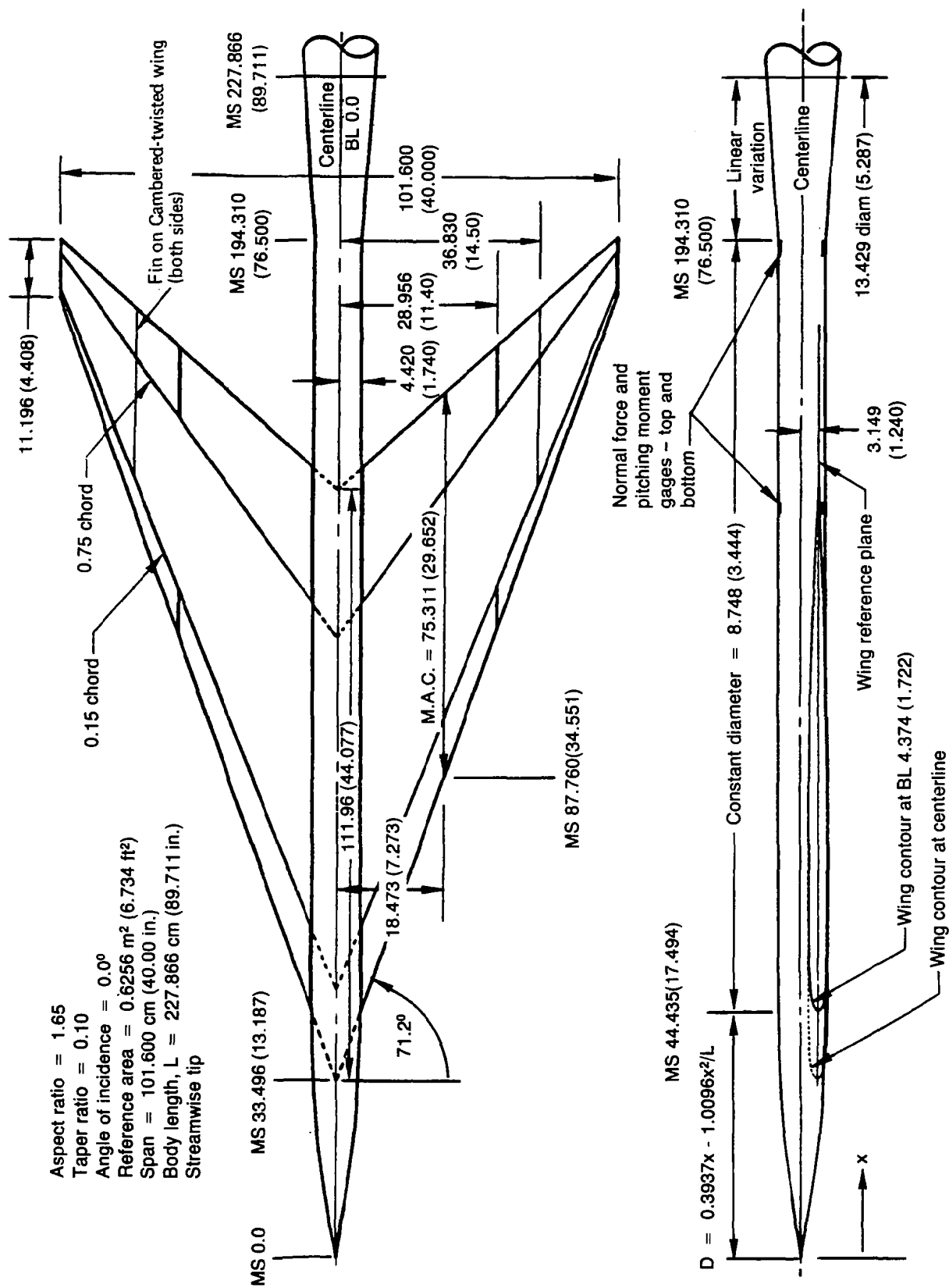
TRIP STRIP

A trip strip of no. 60 carborundum grit was used throughout the tests with the exception of one series. On the body, the trip strip was 0.32 cm (0.125 in.) wide and placed 2.54 cm (1 in.) from the nose. On the wing, it was 0.32 cm (0.125 in.) wide from the side of body to the midspan control surface break ($0.57 b/2$), and tapered to 0.16 cm (0.0625 in.) wide at the wingtip. On the upper surface of the wing, the trip strip was placed at 15-percent chord; and, on the lower surface, it was placed just aft of the location of the leading-edge control surface brackets on the flat wing (see fig. A-6). Density of the grit was 4 to 5 grains per quarter-inch (6 to 8 grains per cm) of trip strip length.

FINAL DATA

Final data (pressure coefficients, tunnel parameters, and model attitude) were merged on magnetic tapes with appropriate configuration and test point identification for integration and plotting of these data.

A detailed description of the data editing and integration procedure are included in appendix B.



All dimensions in centimeters (inches)

Figure A-1.—General Arrangement and Characteristics

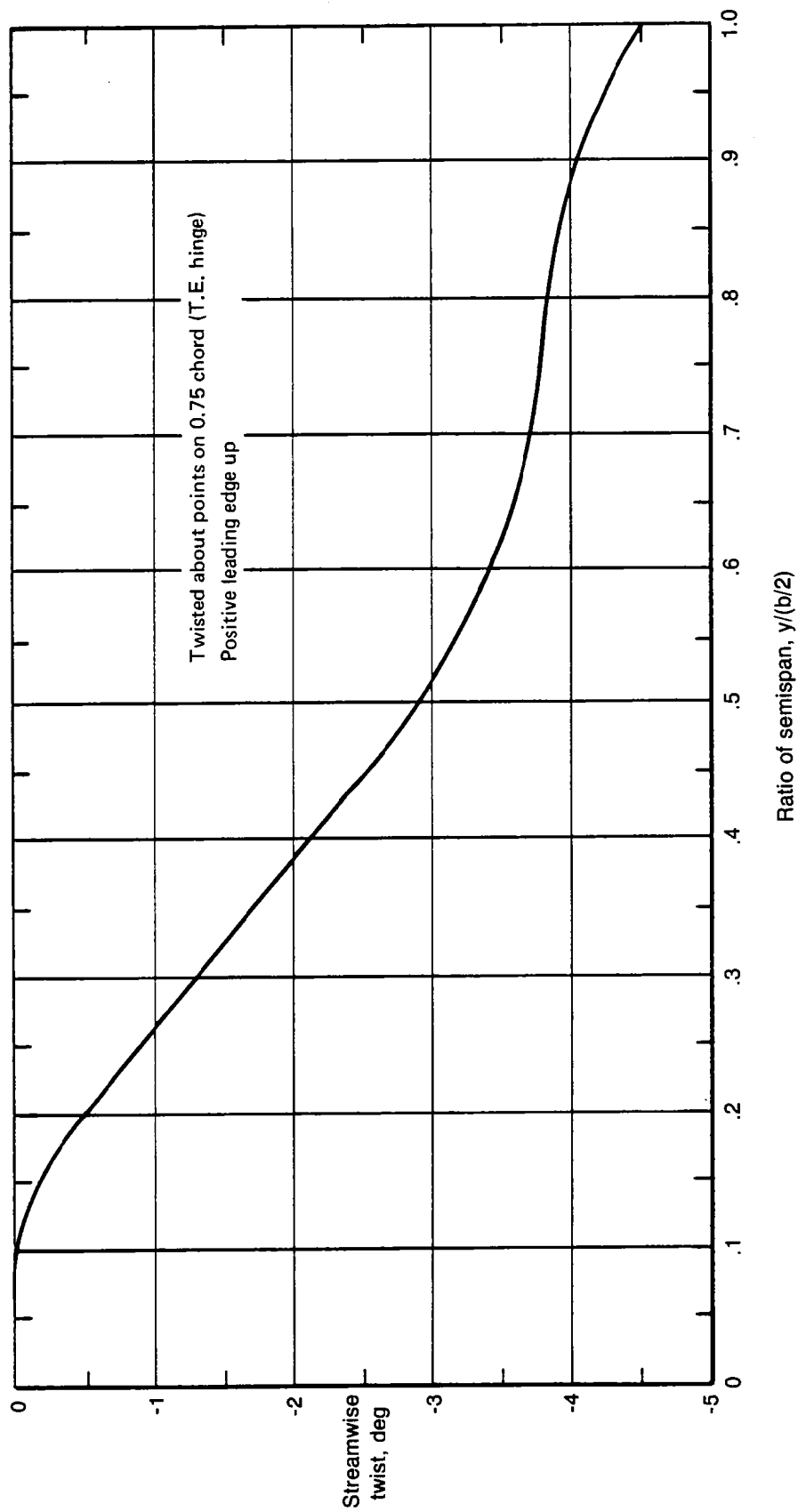
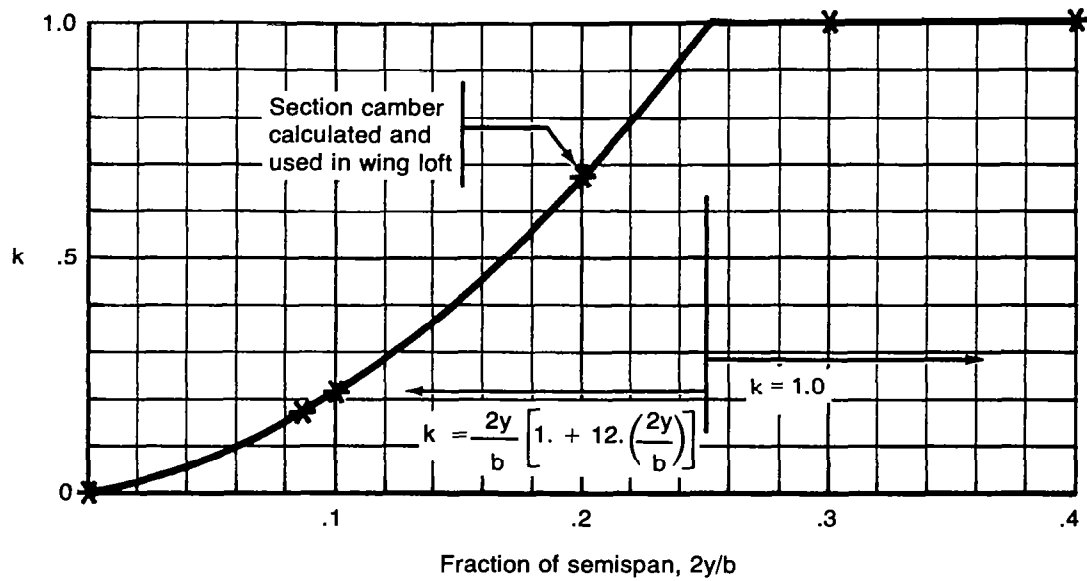
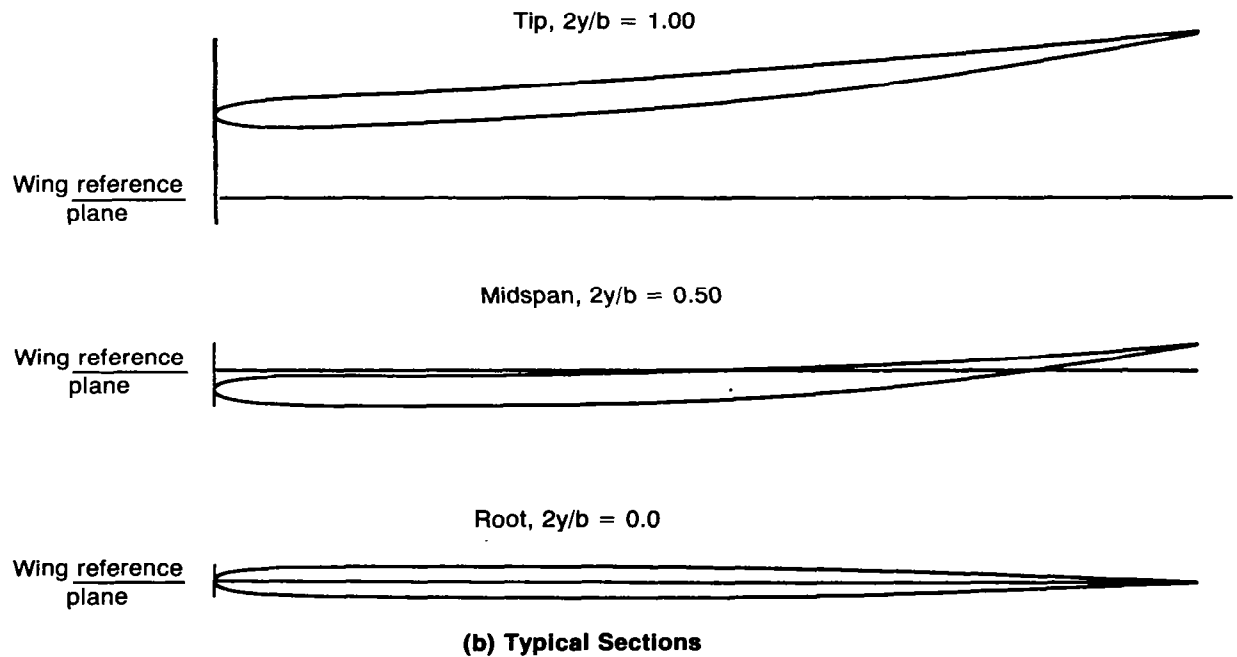


Figure A-2.—Spanwise Twist Distribution for the Model Wing

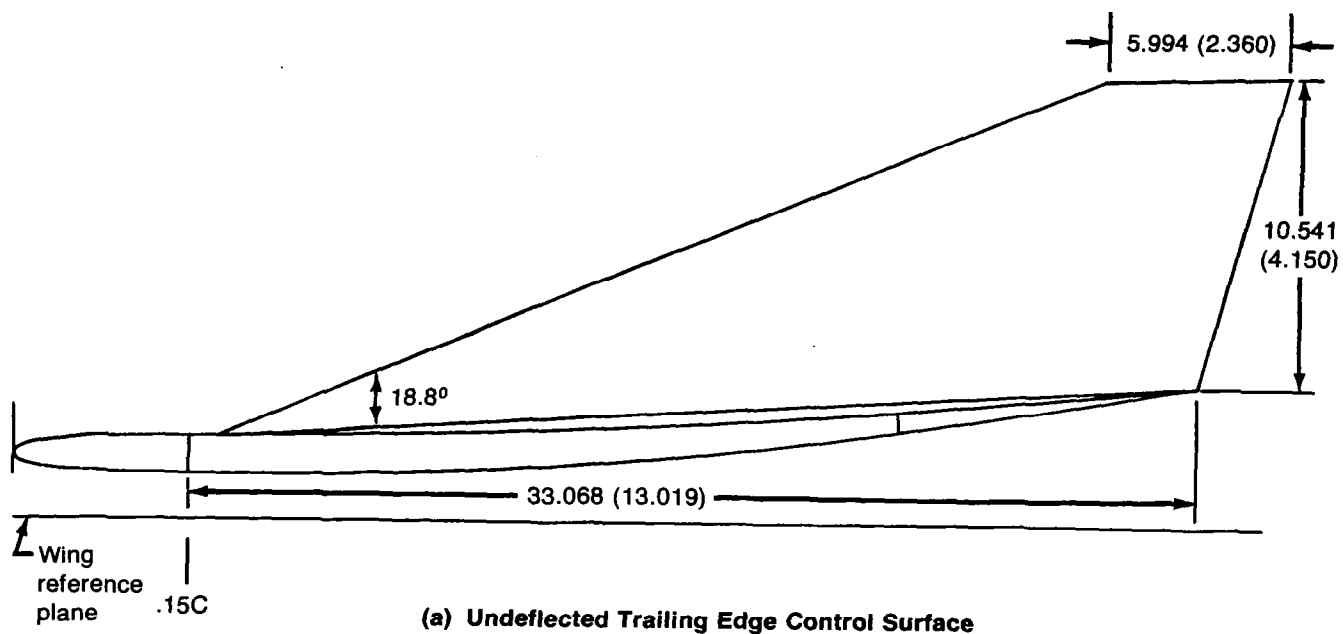


(a) Definition of k , Factor on Basic Camber



(b) Typical Sections

Figure A-3.—Cambered-Twisted Wing Section Geometry



All dimensions in centimeters (inches)

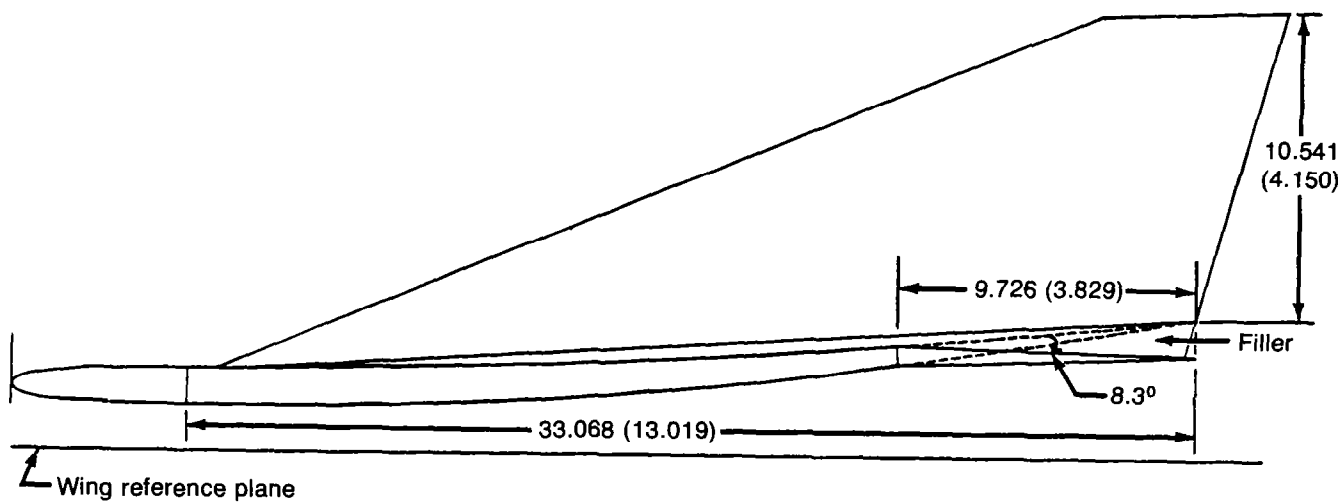


Figure A-4.—Fin Geometry, Section at 0.725 Semispan

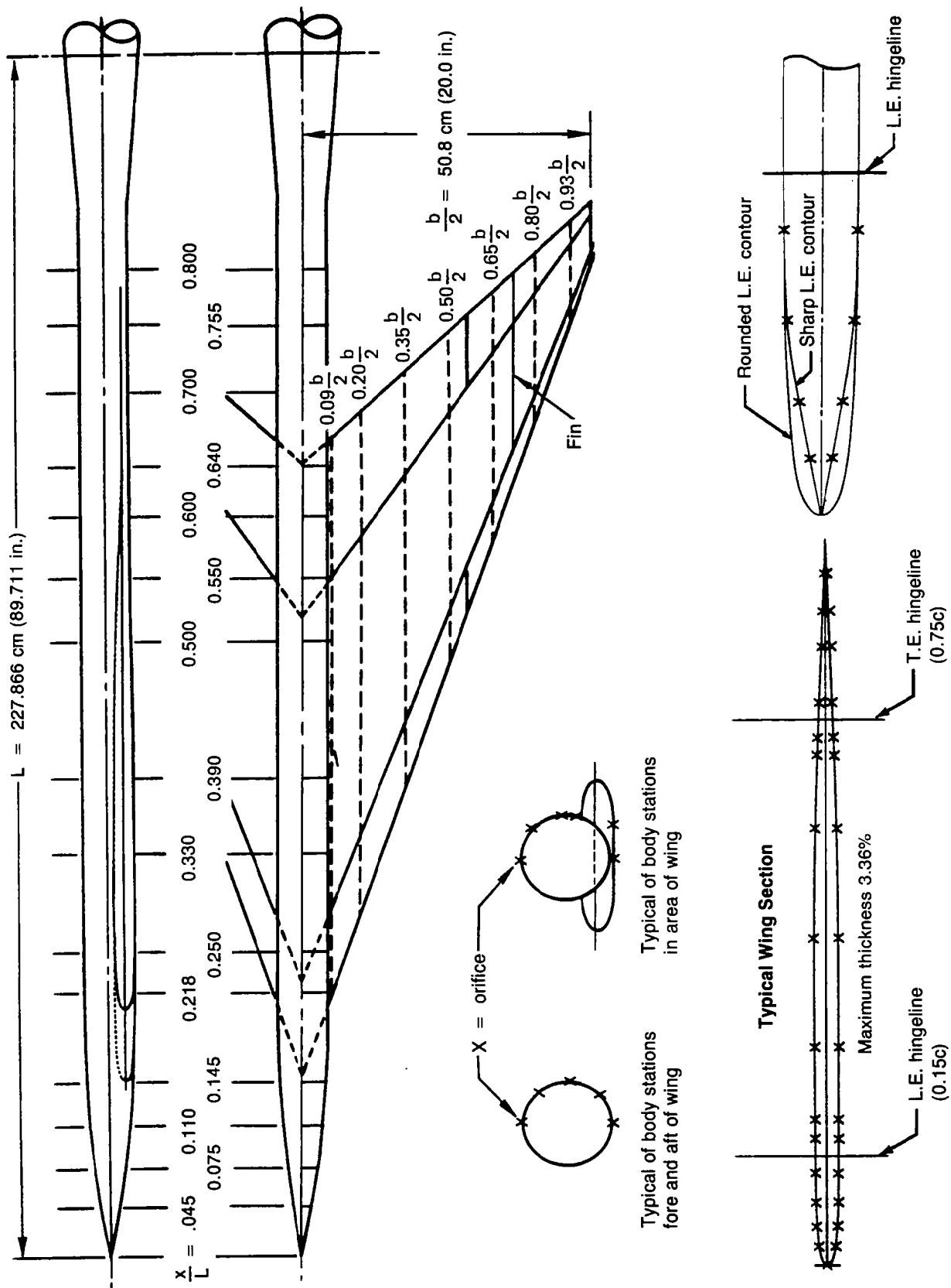


Figure A-5.—Pressure Orifice Locations

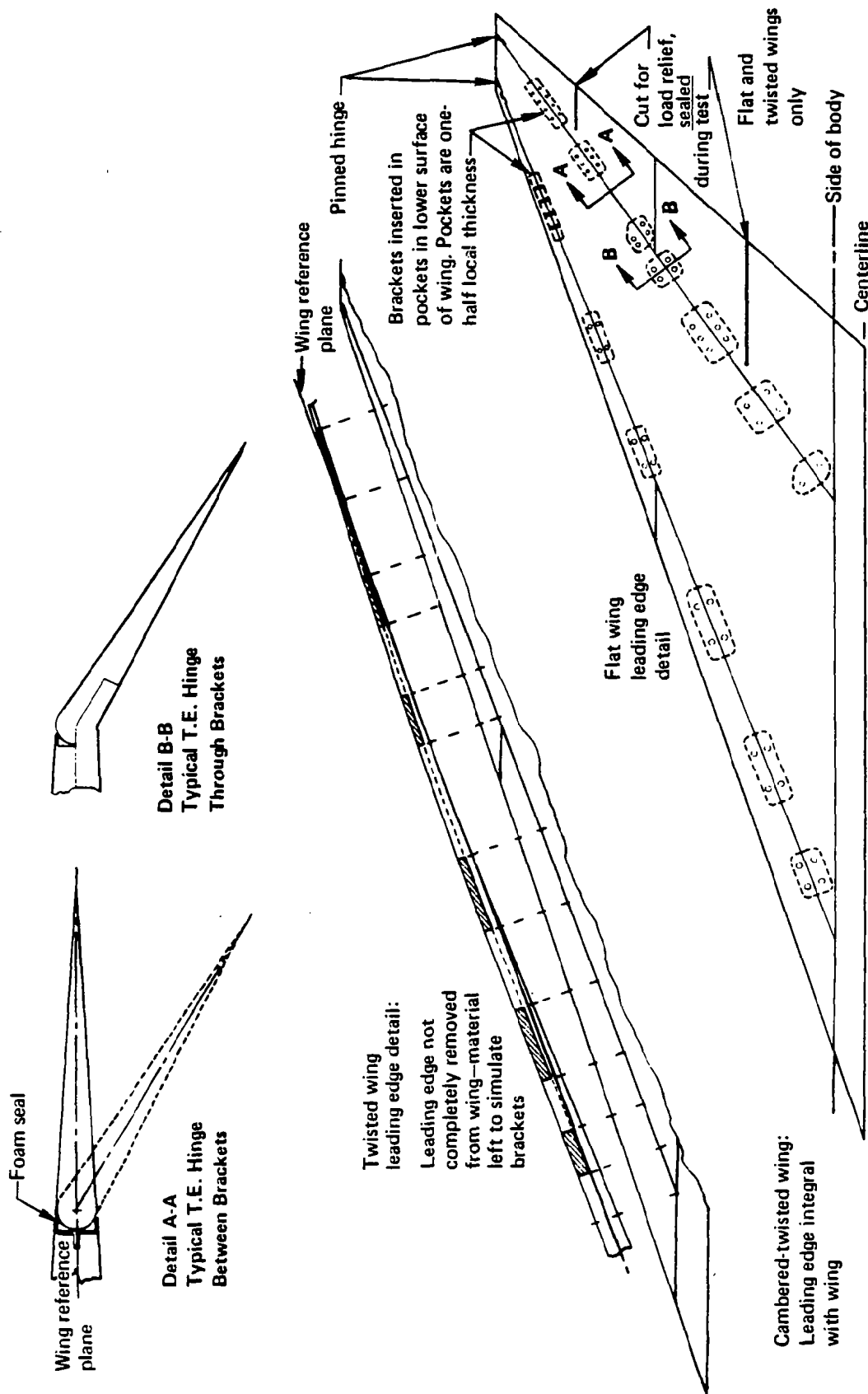
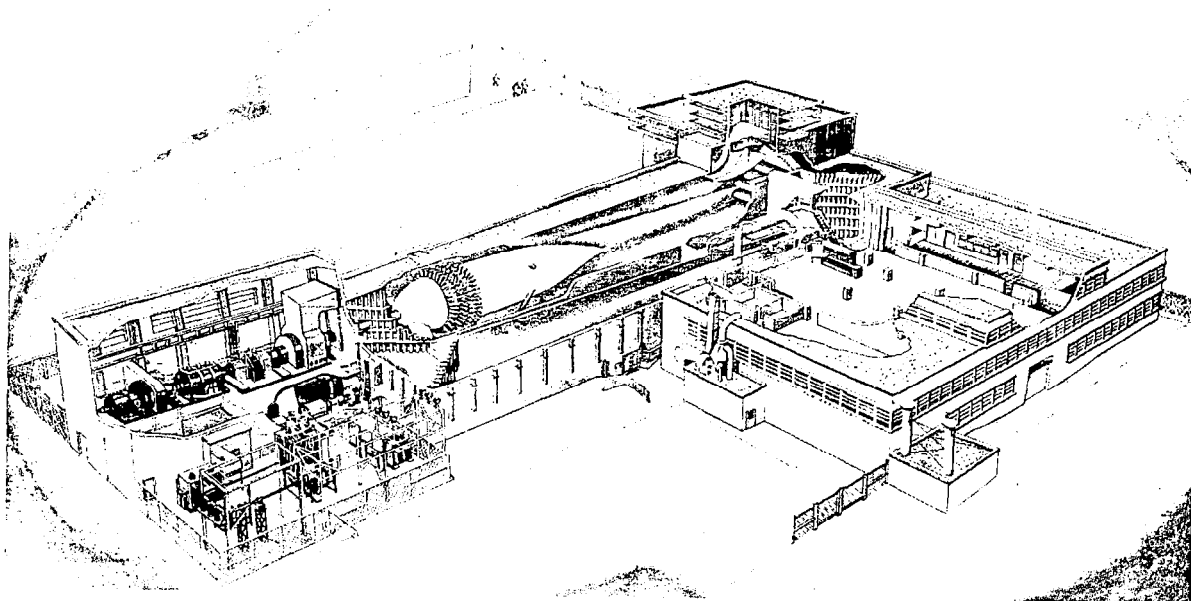
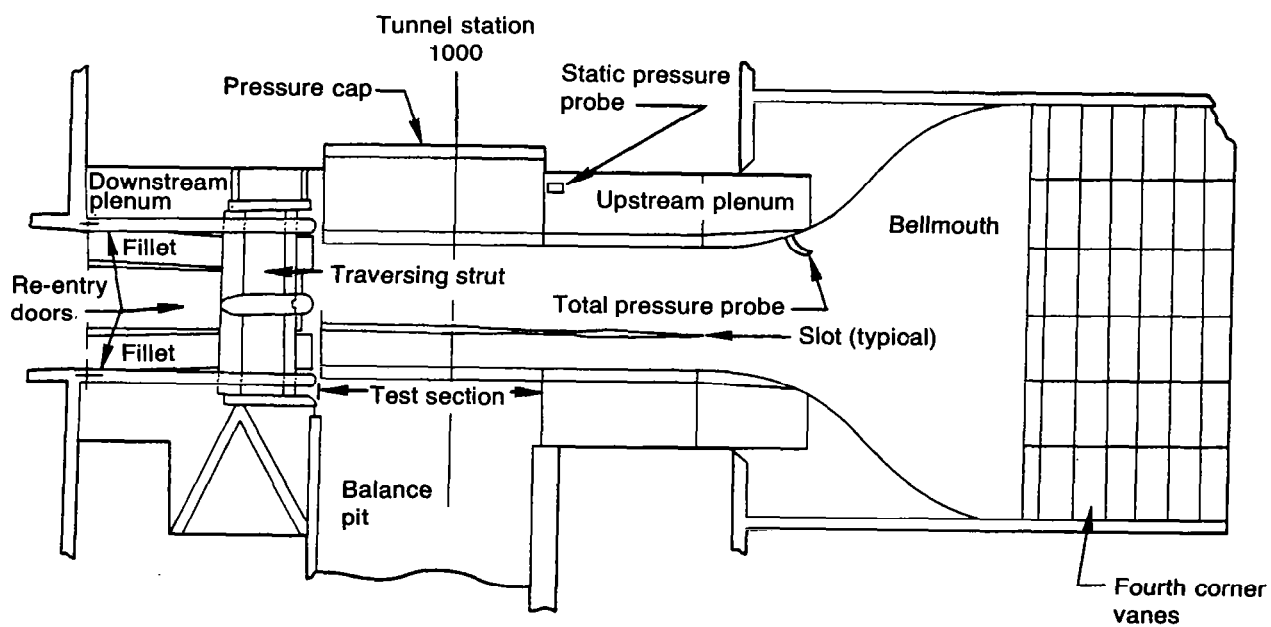


Figure A-6.—Control Surface Bracket Details



(a) Schematic



(b) Test Section

Figure A-7.—Boeing Transonic Wind Tunnel

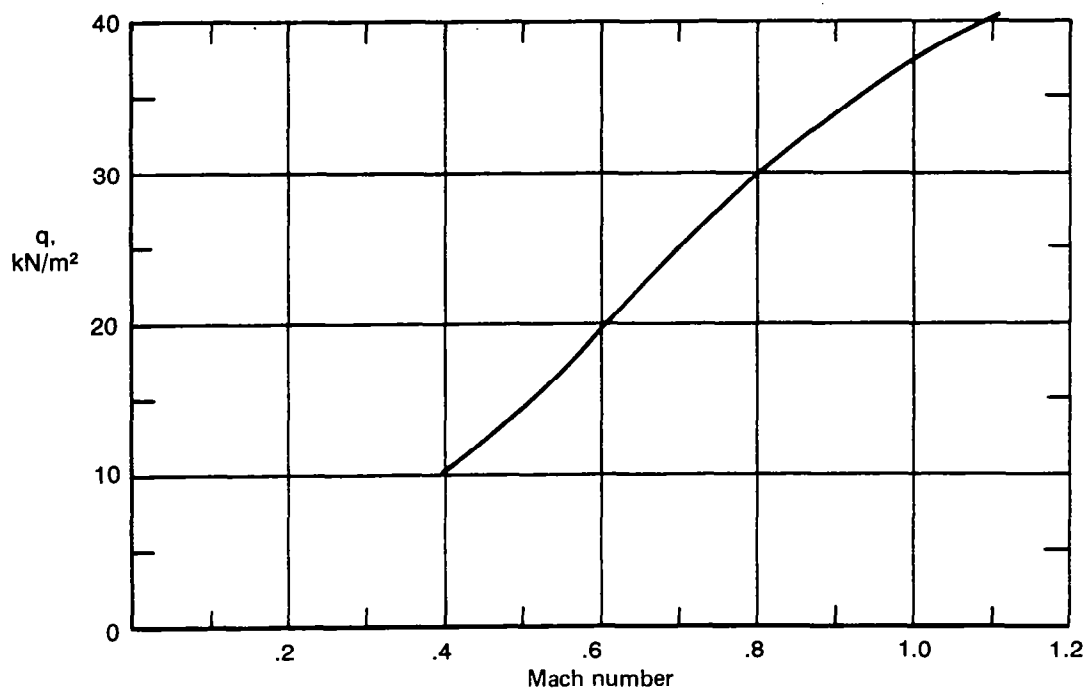
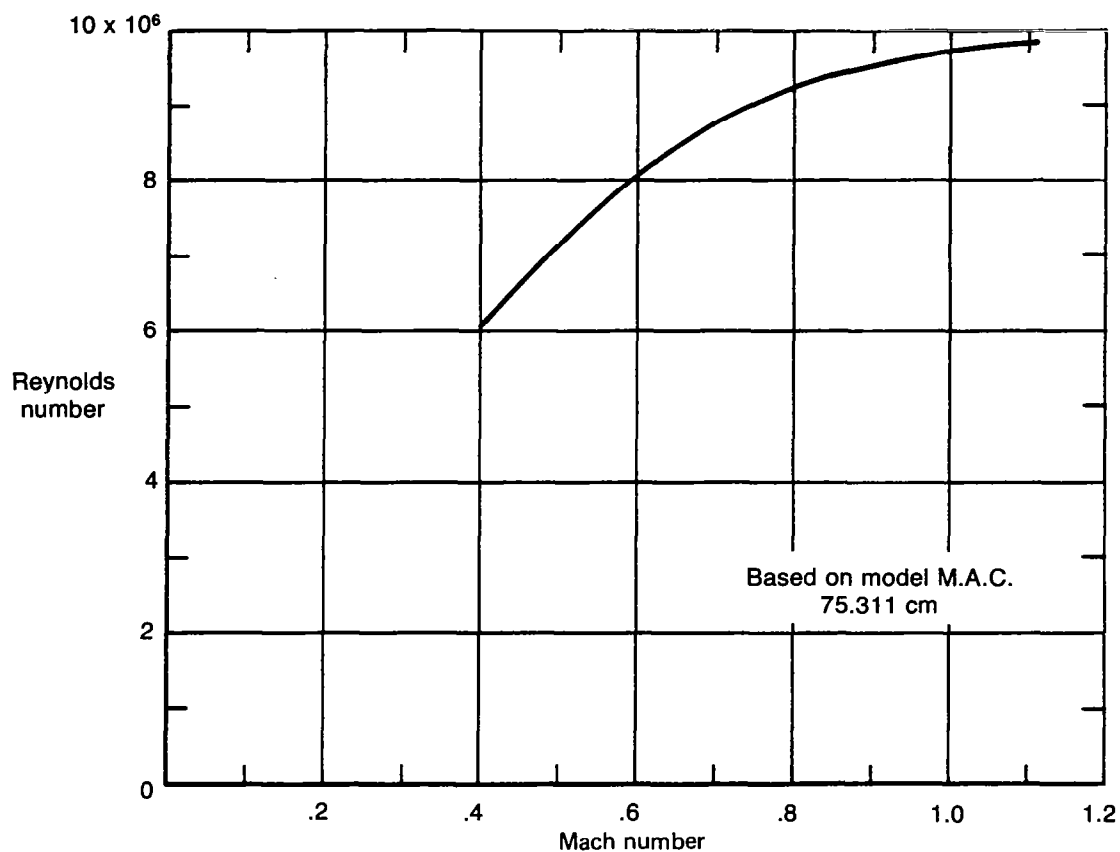


Figure A-8.—Variation of Reynolds Number and Dynamic Pressure With Mach Number

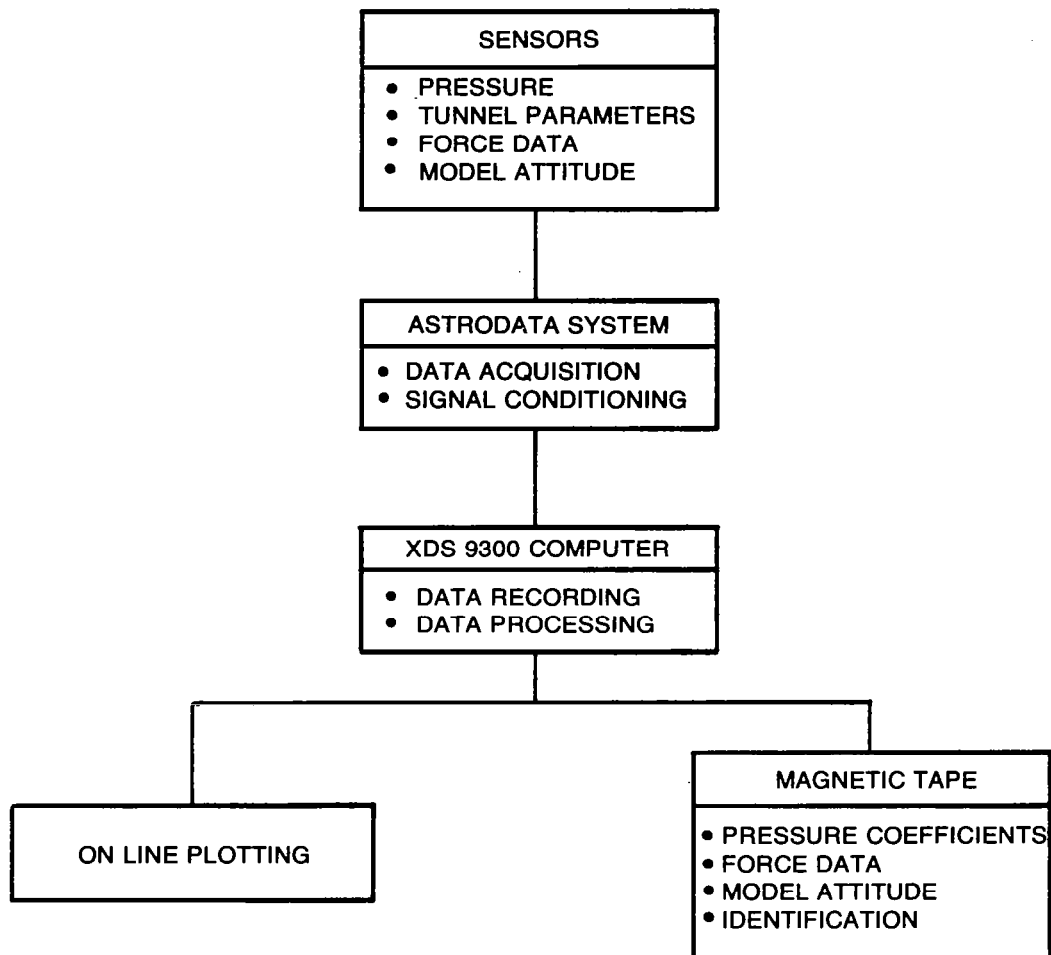


Figure A-9.—Data Acquisition and Reduction System—Boeing Transonic Wind Tunnel

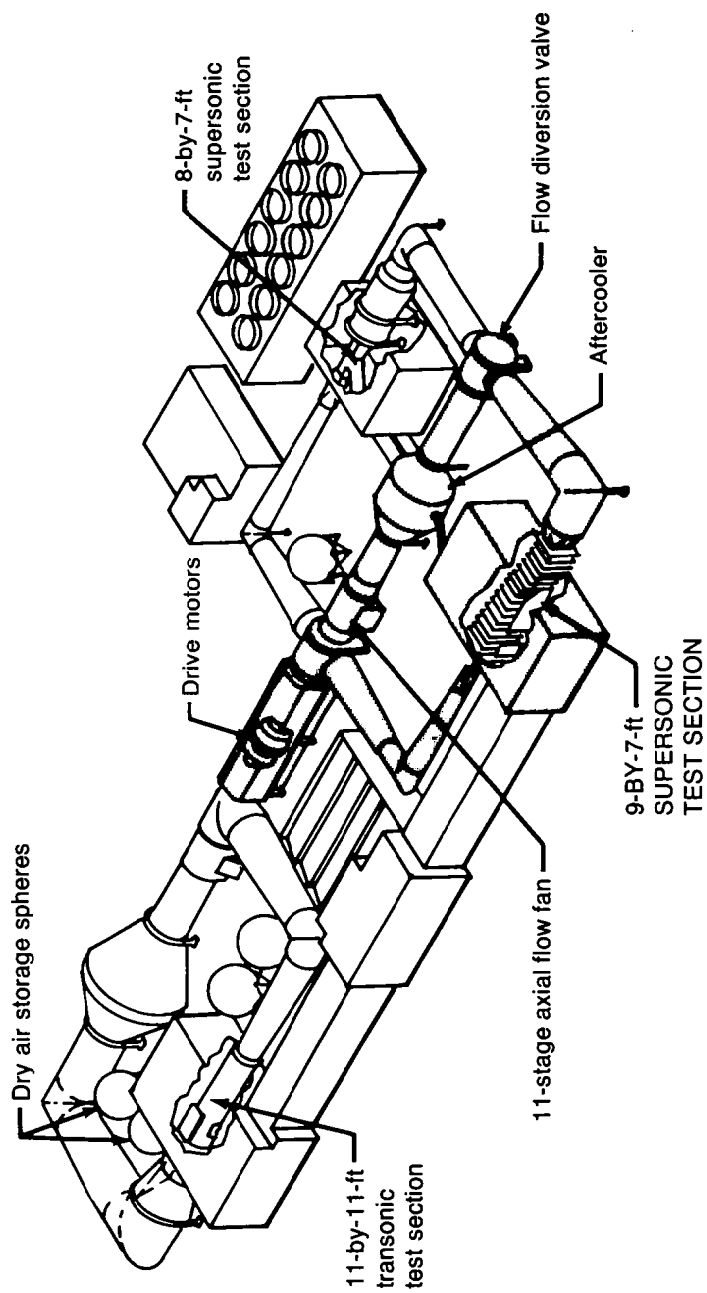


Figure A-10.—Schematic of 9- by 7-ft Supersonic Leg of NASA Ames Unitary Wind Tunnel

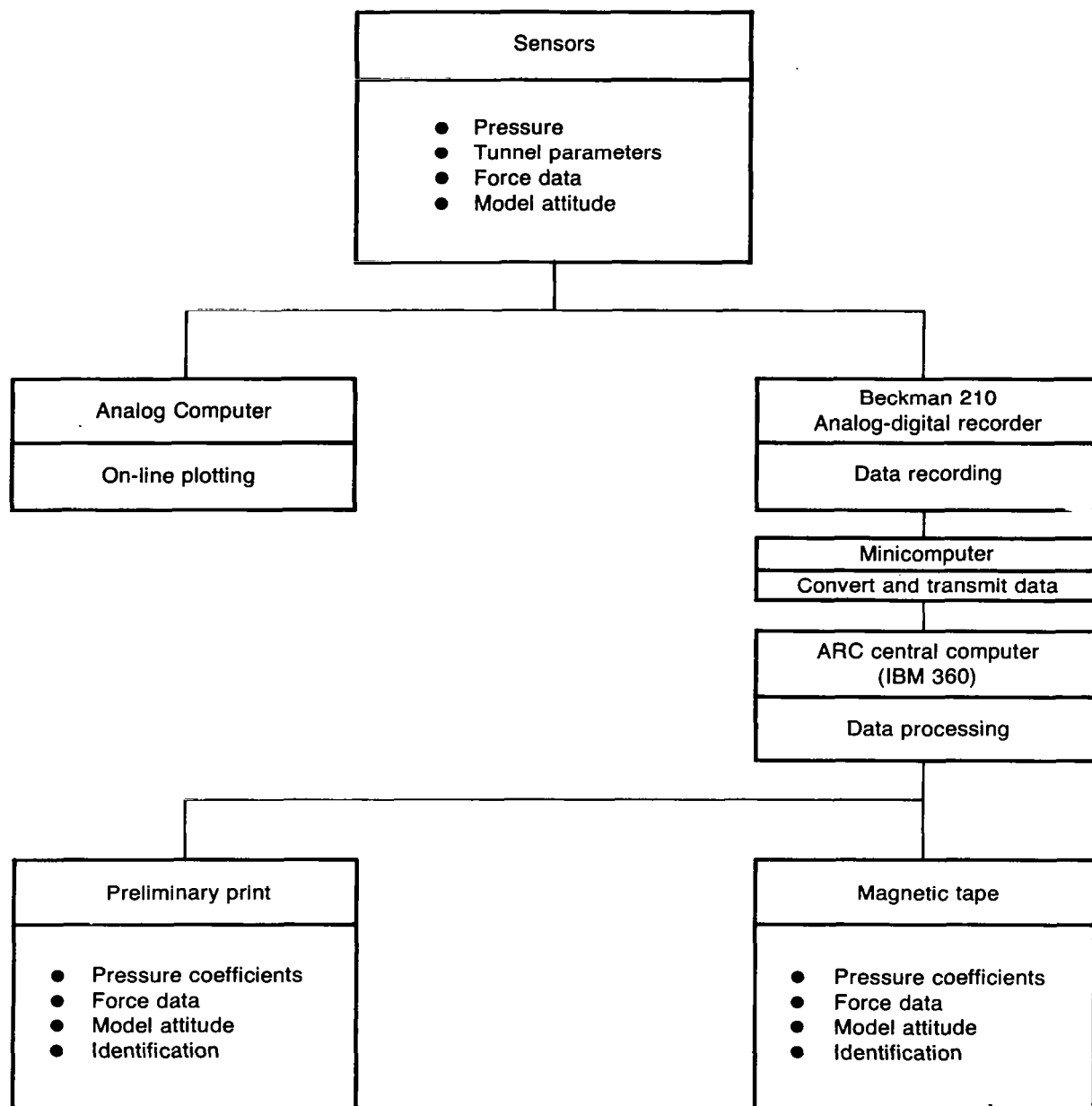


Figure A-11.—Data Acquisition and Reduction System—9- by 7-ft Supersonic Leg of NASA Ames Unitary Wind Tunnel

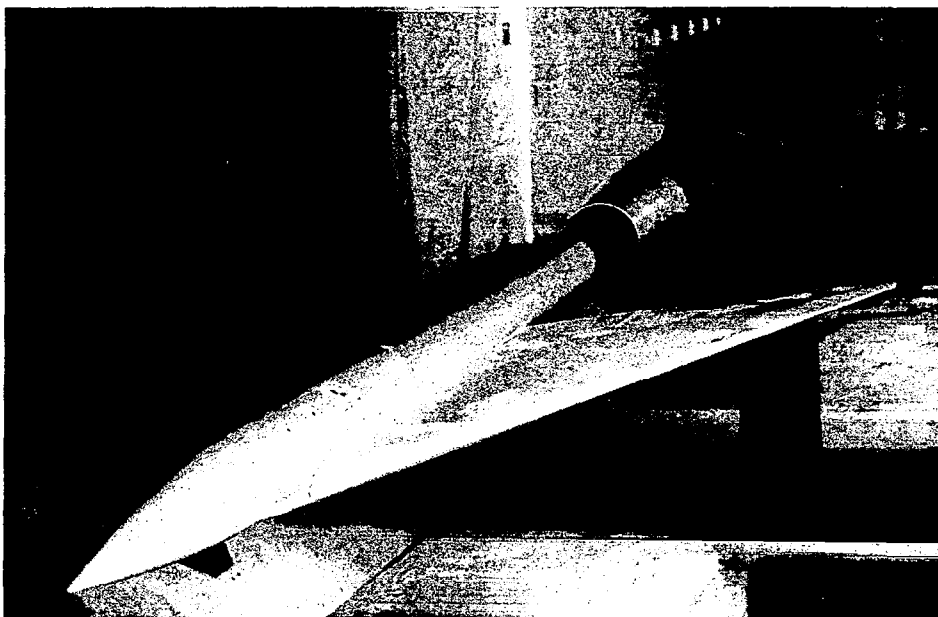
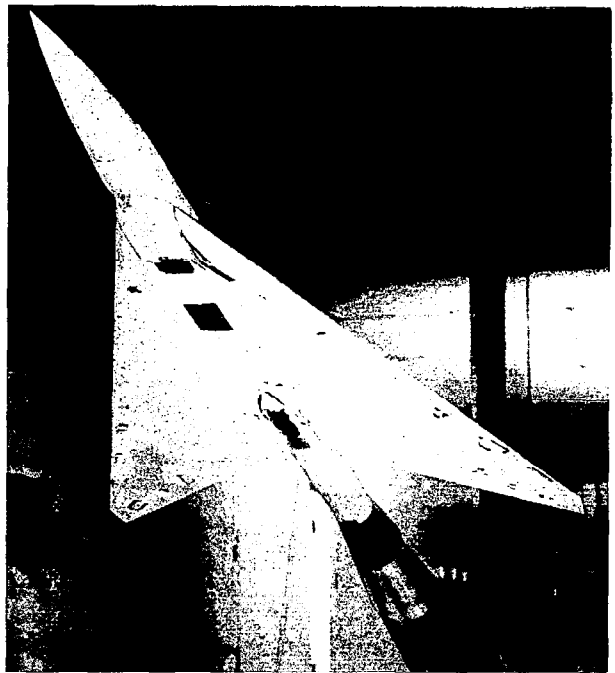
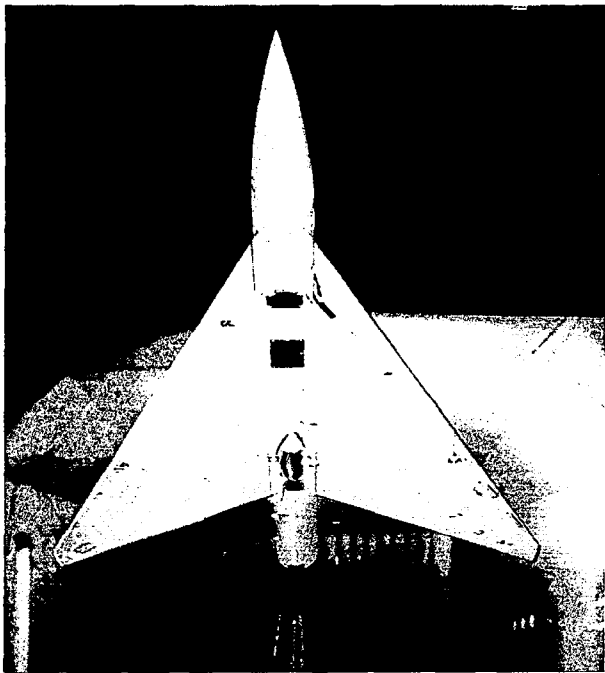


Figure A-12.—Model in Boeing Transonic Wind Tunnel—Flat Wing; L.E. Deflection, Full Span = 0.0° ; T.E. Deflection, Full Span = 0.0° (NASA Contract NAS1-12875)

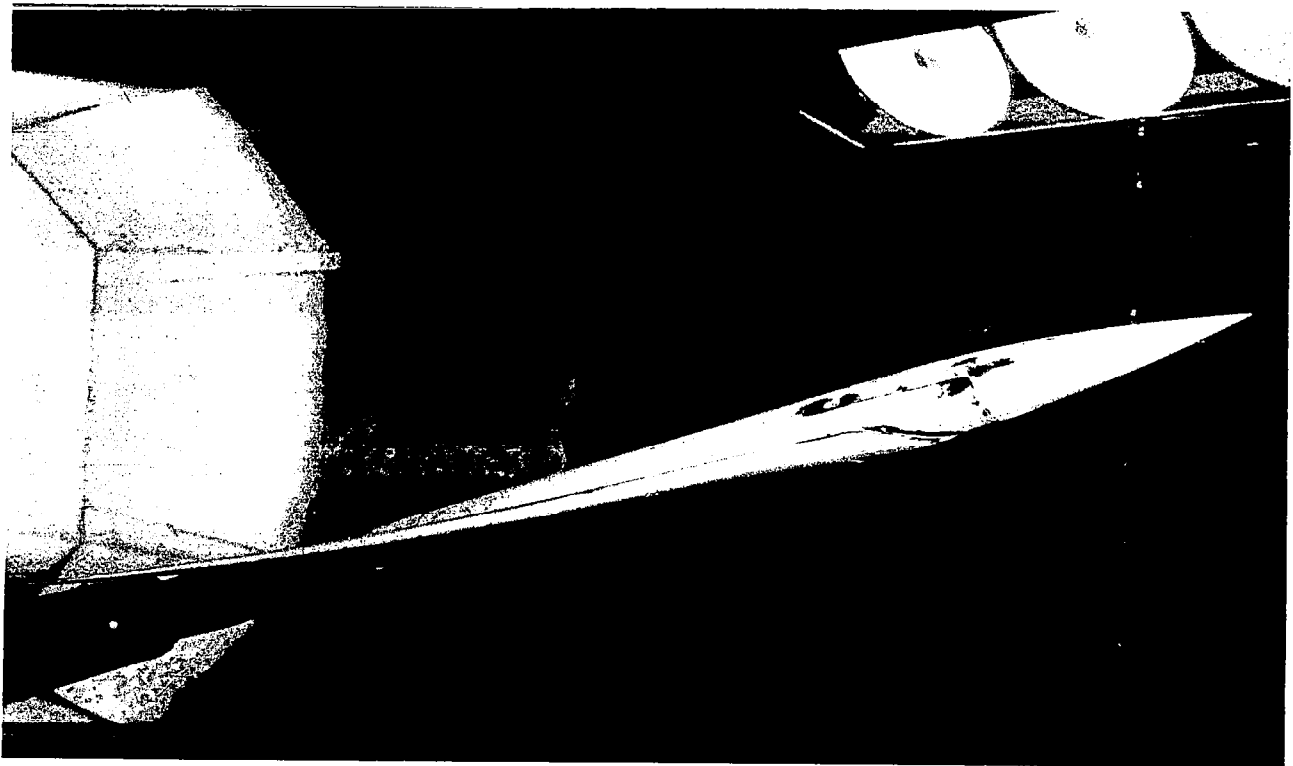
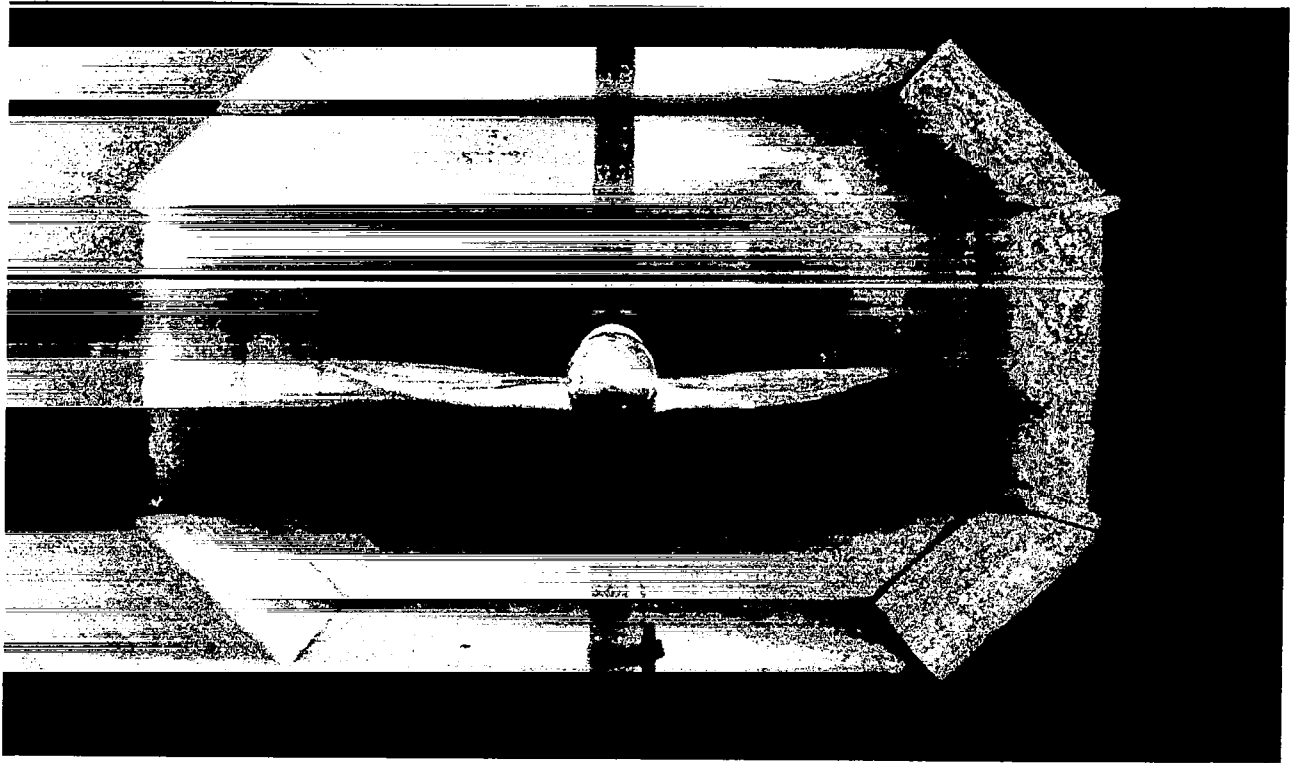


Figure A-13.—Model in Boeing Transonic Wind Tunnel—Twisted Wing; T.E. Deflection, Full Span = 0.0° ; (NASA Contract NAS1-14962)

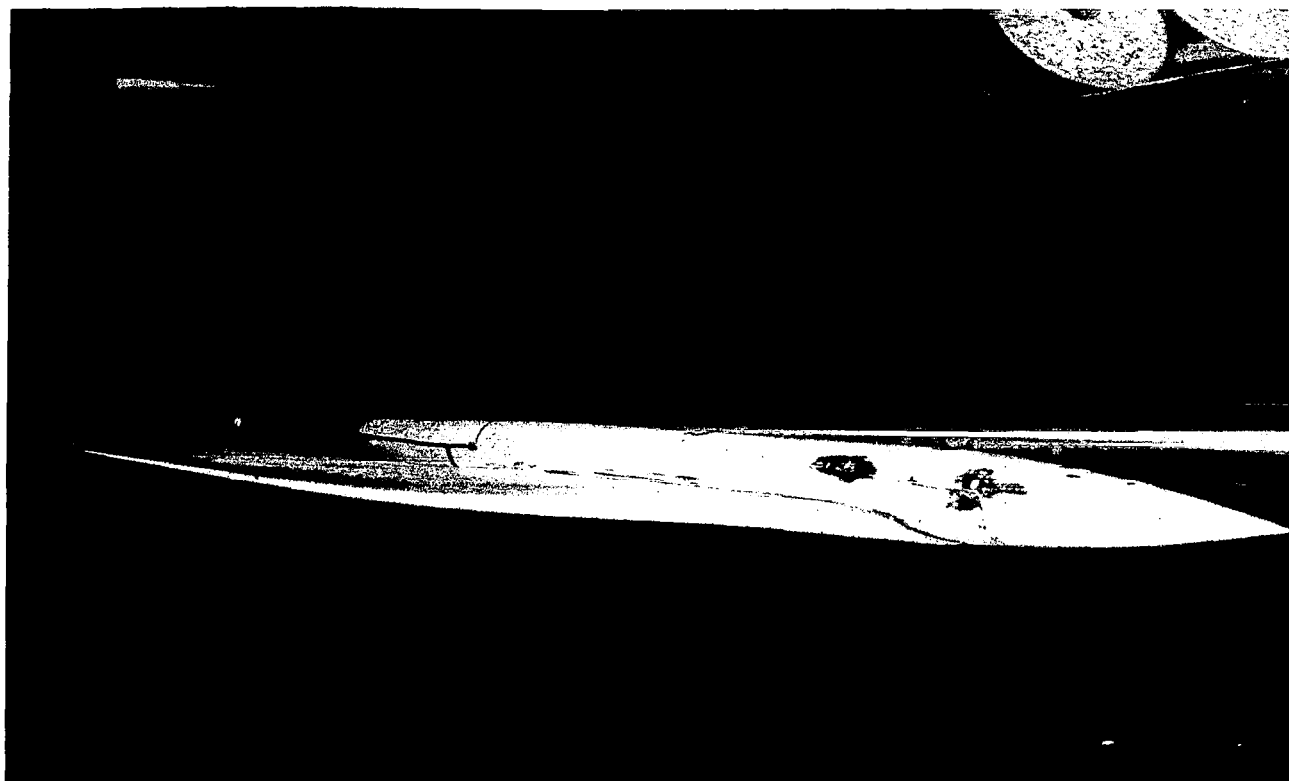
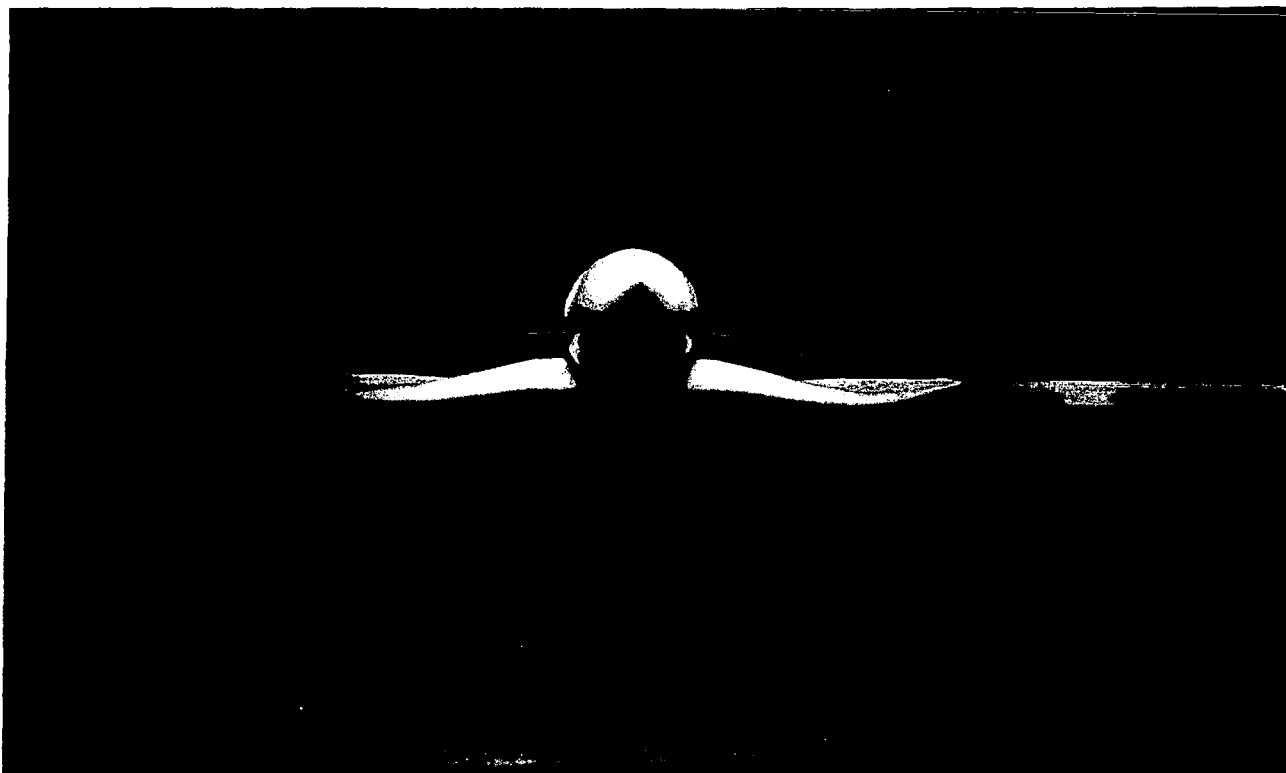
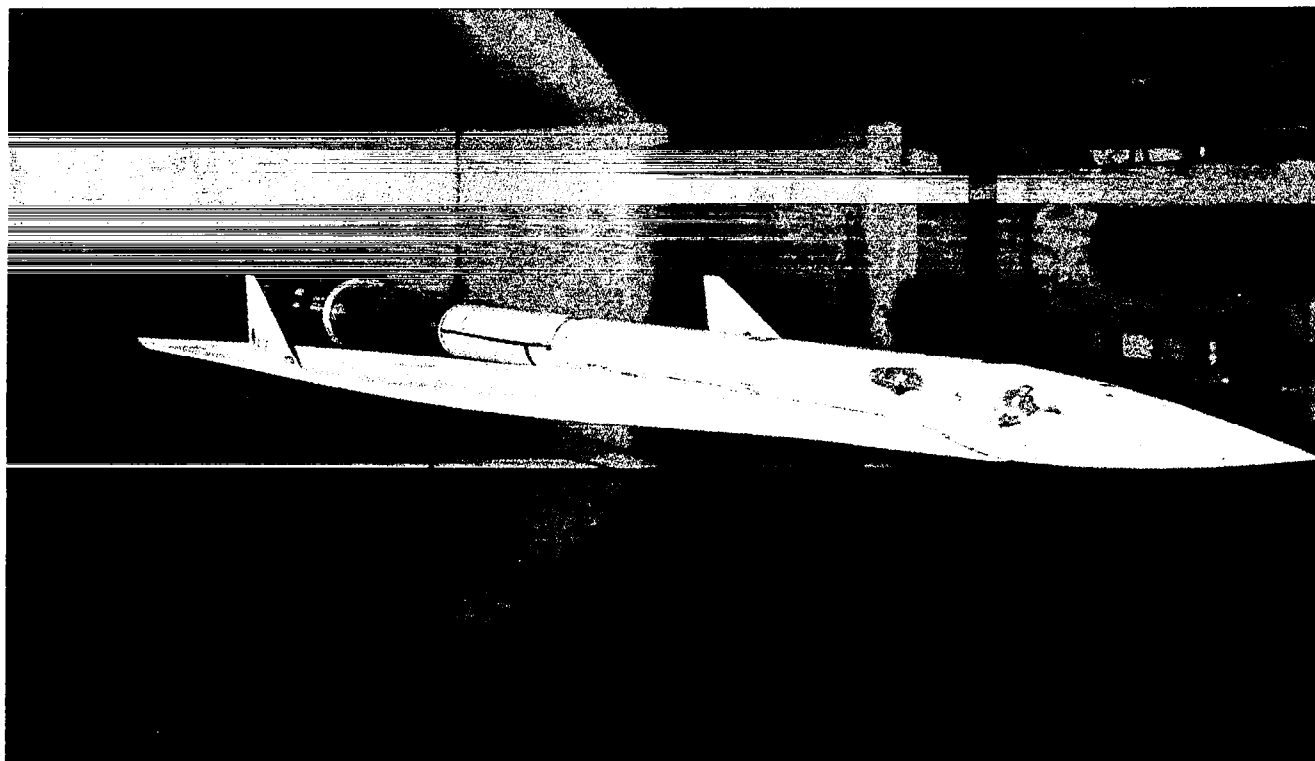
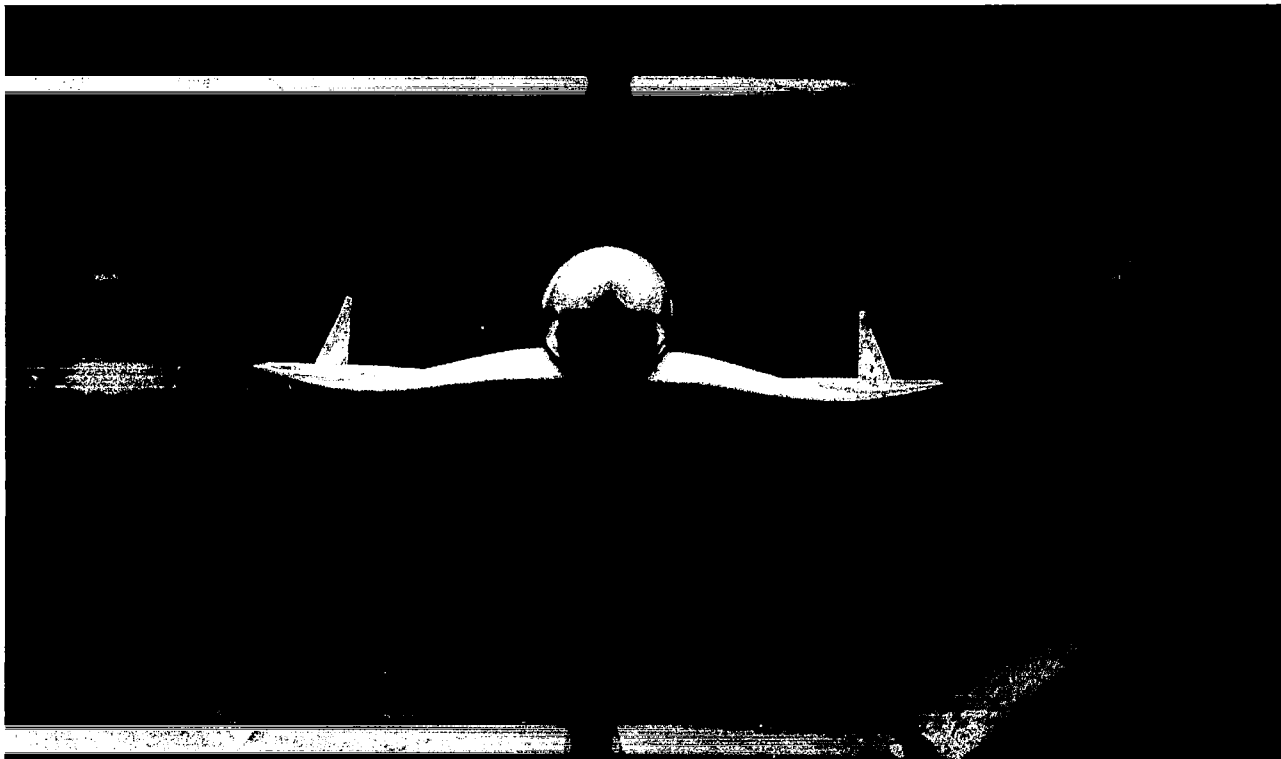


Figure A-14.—Model in Boeing Transonic Wind Tunnel—Cambered-Twisted Wing, Fin Off; T.E. Deflection, Full Span = 0.0° ; (NASA Contract NAS1-14962)



*Figure A-15.—Model in Boeing Transonic Wind Tunnel—Cambered-Twisted Wing, Fin On;
T.E. Deflection, Full Span = 0.0° (NASA Contract NAS1-14962)*

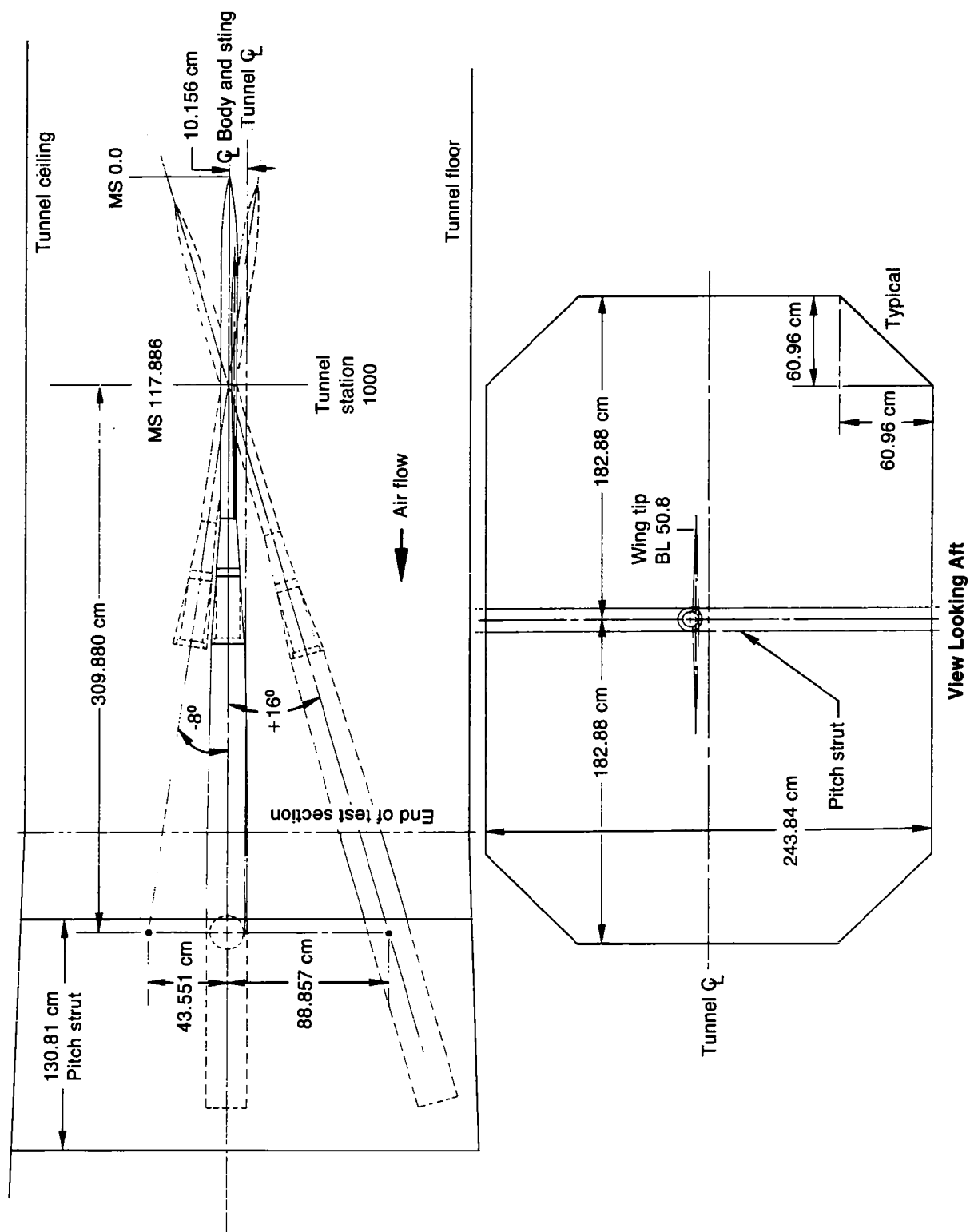


Figure A-16.—Model Installation in Boeing Transonic Wind Tunnel (NASA Contracts NAS1-12875 and NAS1-14962)

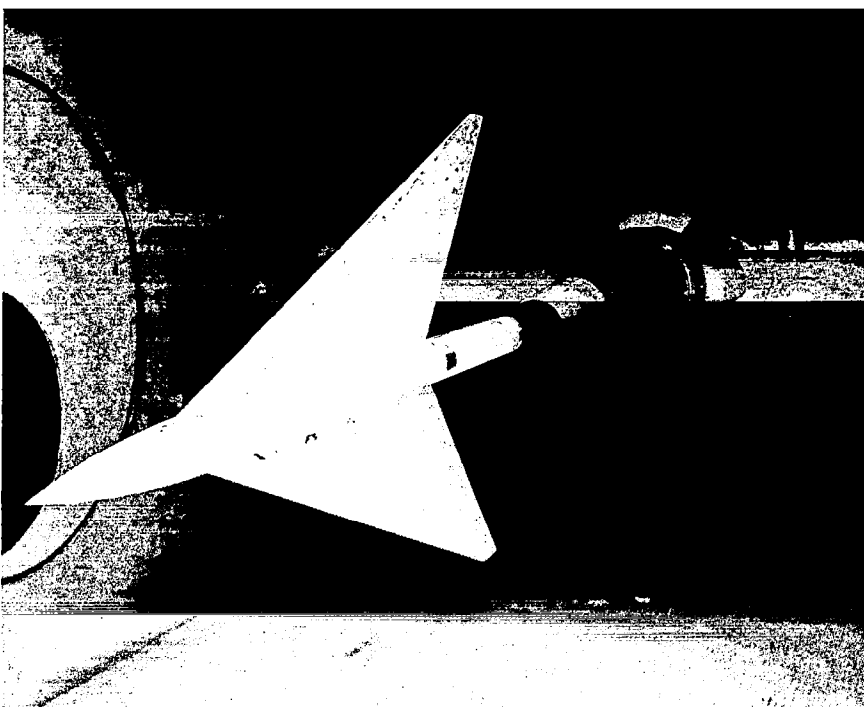
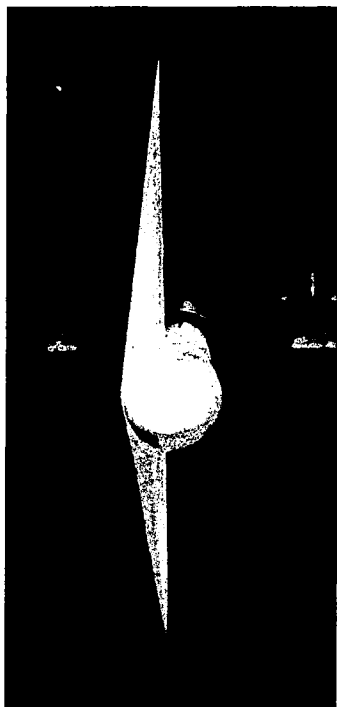


Figure A-17.—Model in 9- by 7-ft Supersonic Leg of NASA Ames Unitary Wind Tunnel—Flat Wing, Rounded L.E. (NASA Contract NAS1-14141)

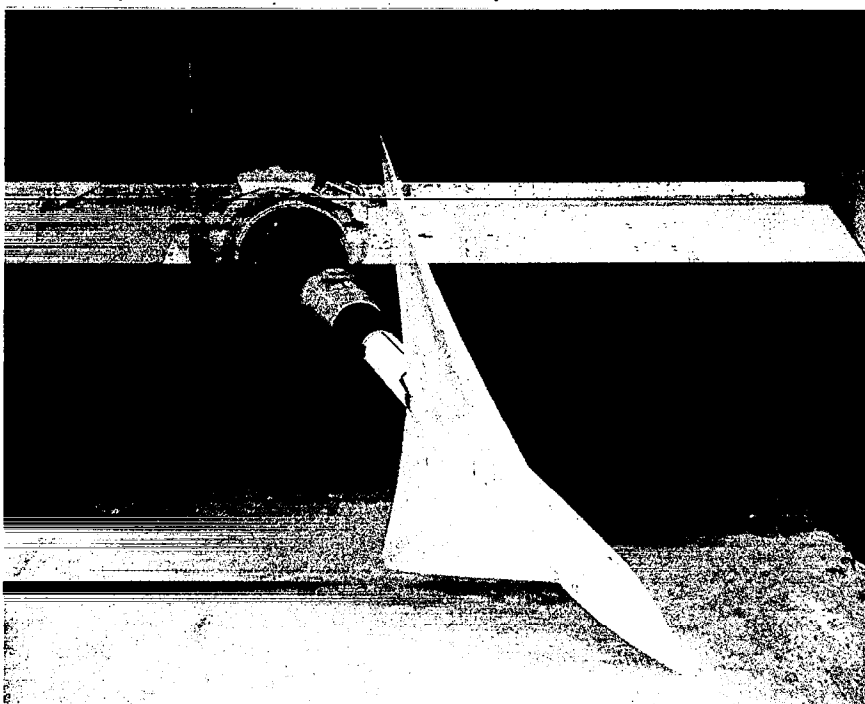
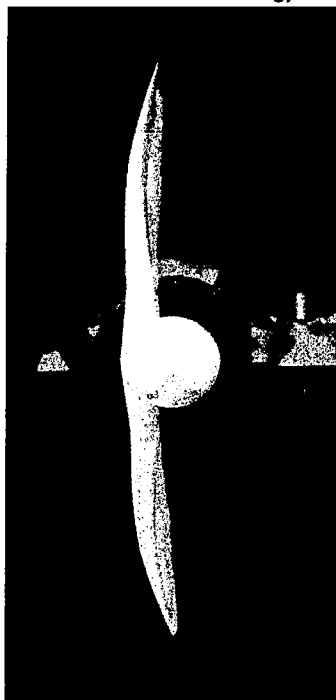


Figure A-18.—Model in 9- by 7-ft Supersonic Leg of NASA Ames Unitary Wind Tunnel—Twisted Wing (NASA Contract NAS1-14141)

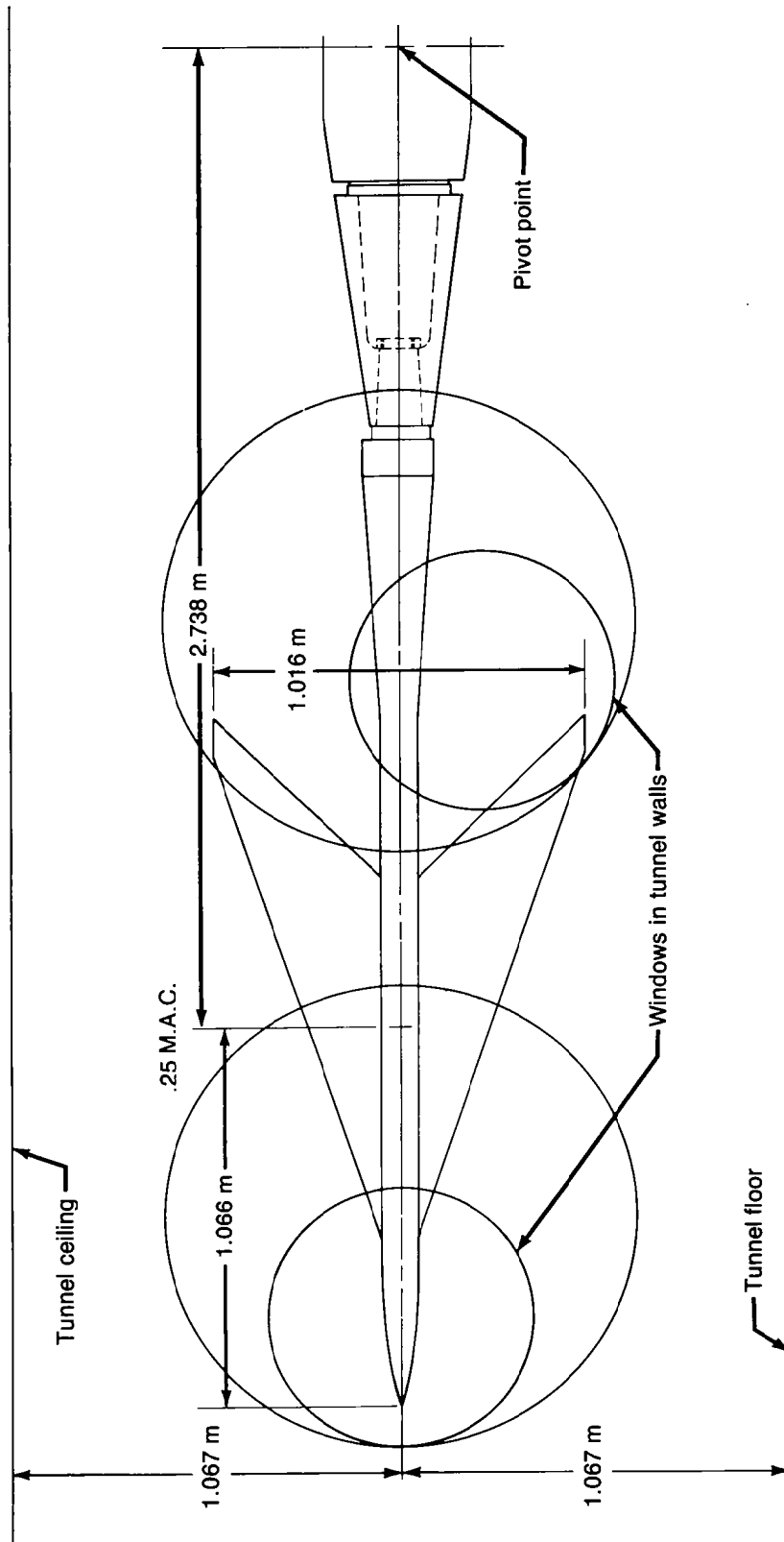


Figure A-19.—Model Installation in 9- by 7-ft Supersonic Leg of NASA Ames Unitary Wind Tunnel (NASA Contract NAS1-14141)

APPENDIX B

DATA REDUCTION

DATA EDITING

There were some cases encountered with these data where the methods of data editing available within the integration programs were not adequate. Because the plotting program assumes that the geometry is the same for all configurations, and the chordwise location of orifices on the various model parts was not absolutely identical, points were added as required. Therefore, some interpolations or extrapolations using selected orifices were done before the integration program was used. The row of orifices on the body at the wing-body intersection was extended in front of the wing and aft of the wing by interpolating between the orifices located at 90° and 135° .

Some specific problems with the data acquisition systems required the replacement of some data for parts of tests. These are identified in appendix A.

Several methods were introduced into the integration program to replace or add data points to account for:

- Plugged or leaking orifices, or bad data points
- Extrapolating the data to leading and trailing edges
- Hingeline discontinuities in the pressure data

These procedures were selected by code for each point. The codes are described in the following list and are illustrated in figure B-1. An additional use of these codes is to ensure that only measured pressure data ($CODE_i = 0$) are identified with symbols on the plots. The subscript i identifies the position of the point from the leading edge of the upper or lower surface of the section.

IF $CODE_i = 0$, use pressure as entered on tape (measured pressure)

= 20, use as entered on tape (previously replaced value)

= 1, interpolate from adjacent points

= 2, extrapolate from two preceding points

= 3, extrapolate from two following points

= 4, set equal to preceding point

= 5, set equal to following point

= 6, interpolate using points $(i-2)$ and $(i+1)$

= 7, interpolate using points $(i-1)$ and $(i+2)$

IF CODE_i = negative of above, evaluate as above but average with corresponding point on opposite surface; used for leading and trailing edges of section only

Editing of the pressure data is done in the following order:

1. Each section is done separately.
2. Each surface (upper or lower) per section is done in the following sequence:
 - a. Starting at leading edge, points with codes of 1, 2, and 4.
 - b. Starting at trailing edge, points with codes of 3, 5, 6, and 7.
3. Leading- and trailing-edge points with negative codes are evaluated. Both upper and lower surface codes need not be negative and need not be the same negative code.

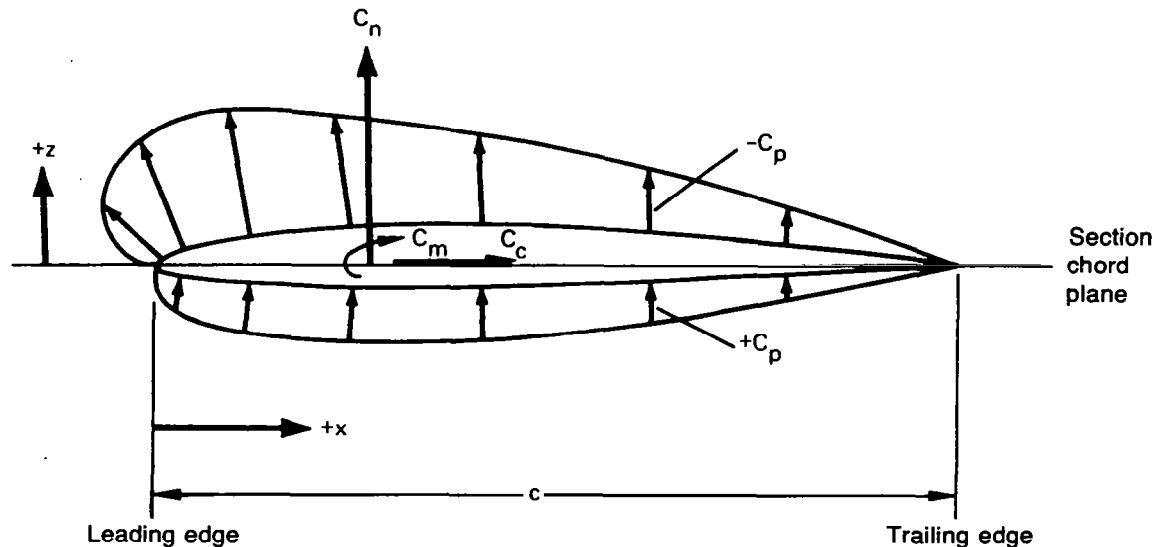
CALCULATION OF NET PRESSURE COEFFICIENTS

The net lift distribution on the section is calculated by:

$$C_{p,net} = C_{p,lower} - C_{p,upper} \quad (B-1)$$

INTEGRATION OF PRESSURE DATA

To account for the effects on integrated coefficients of the deflected control surfaces, each streamwise section (of which there are NSECT) is divided into segments (of which there are NSEG). These segments are the leading-edge control surface, wing box, and trailing-edge control surface. The upper and lower surfaces of each are integrated separately over the number of points available ((number of orifices + 2) = NP1), and are based on the segment chord length c . Sign conventions are shown in the following sketch. The equations, which use a rectangular integration process, follow.



SEGMENT COEFFICIENTS

Integration of the pressures for each segment per surface per section is the first step.

- o Normal force coefficient $C_{n,s}$

$$C_{n,s} = 0.5 \sum_{i=2}^{NP1} \left[(C_p)_i + (C_p)_{i-1} \right] \left[\left(\frac{x}{c} \right)_i - \left(\frac{x}{c} \right)_{i-1} \right] \quad (B-2)$$

$$C_{n,s,net} = C_{n,s,lower} - C_{n,s,upper} \quad (B-3)$$

- o Chord force coefficient $C_{c,s}$

$$C_{c,s} = 0.5 \sum_{i=2}^{NP1} \left[(C_p)_i + (C_p)_{i-1} \right] \left[\left(\frac{z}{c} \right)_i - \left(\frac{z}{c} \right)_{i-1} \right] \quad (B-4)$$

$$C_{c,s,net} = C_{c,s,upper} - C_{c,s,lower} \quad (B-5)$$

- o Pitching moment coefficient about segment leading edge $C_{m,s}$

$$\begin{aligned} C_{m,s} &= 0.5 \sum_{i=2}^{NP1} \left[(C_p)_i + (C_p)_{i-1} \right] \left[\frac{x}{c} \Big|_{i-1} + \frac{\left(\frac{x}{c} \right)_i - \left(\frac{x}{c} \right)_{i-1}}{2.0} \right] \left[\left(\frac{x}{c} \right)_i - \left(\frac{x}{c} \right)_{i-1} \right] \\ &= 0.25 \sum_{i=2}^{NP1} \left[(C_p)_i + (C_p)_{i-1} \right] \left[\left(\frac{x}{c} \right)_i^2 - \left(\frac{x}{c} \right)_{i-1}^2 \right] \end{aligned} \quad (B-6)$$

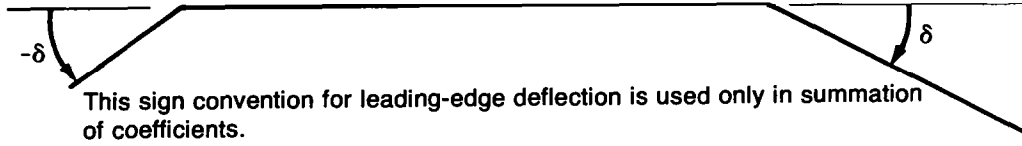
$$C_{m,s,net} = C_{m,s,upper} - C_{m,s,lower} \quad (B-7)$$

- o Pitching moment coefficient about 0.25 c of segment $C_{m.25c,s}$

$$C_{m.25c,s} = C_{m,s} + 0.25 C_{n,s} \quad (B-8)$$

SECTION COEFFICIENTS

Total section coefficients are obtained by summing the segment coefficients, taking into account both the segment deflections as defined in the following sketch and the segment chord lengths. These coefficients are based on the section chord length c .



- o Normal force coefficient C_n

$$C_n = \sum_{j=1}^{NSEG} (C_{n,s})_j \left(\frac{c_s}{c}\right)_j \cos \delta_j - \sum_{j=1}^{NSEG} (C_{c,s})_j \left(\frac{c_s}{c}\right)_j \sin \delta_j \quad (B-9)$$

- o Pitching moment coefficient about section leading edge C_m

$$C_m = \sum_{j=1}^{NSEG} (C_{m,s})_j \left(\frac{c_s}{c}\right)_j^2 + \left[(C_{n,s})_1 (1.0 - \cos \delta_1) + (C_{c,s})_1 \sin \delta_1 \right] \left(\frac{c_s}{c}\right)_1^2 - \sum_{j=2}^{NSEG} \left[(C_{n,s})_j \cos \delta_j - (C_{c,s})_j \sin \delta_j \right] \left(\frac{c_s}{c}\right)_j \left[\frac{x_{L.E.,s} - x_{L.E.}}{c} \right]_j \quad (B-10)$$

where

- c_s is segment chord length, cm
- c is section chord length, cm
- δ is deflection of segment relative to section chord plane, leading edge up, degrees
- $x_{L.E.,s}$ is leading edge of segment, cm
- $x_{L.E.}$ is leading edge of section, cm

- o Pitching moment coefficient about 0.25 c of section $C_{m.25c}$

$$C_{m.25c} = C_m + 0.25 C_n \quad (B-11)$$

TOTAL SURFACE COEFFICIENTS

To obtain total surface coefficients, the assumption is made that the section coefficients apply for a finite distance on both sides of each row of orifices. The equations for total surface coefficients are as follows:

- o Normal force coefficient C_N

$$C_N = \frac{1}{S} \sum_{k=1}^{N_{SECT}} (C_n)_k (S_h)_k \quad (B-12)$$

- o Bending moment coefficient C_B

$$C_B = \frac{1}{S(b/2)} \sum_{k=1}^{N_{SECT}} (C_n)_k (S_h^y)_k \quad (B-13)$$

- o Pitching moment coefficient about 0.25 M.A.C. C_M

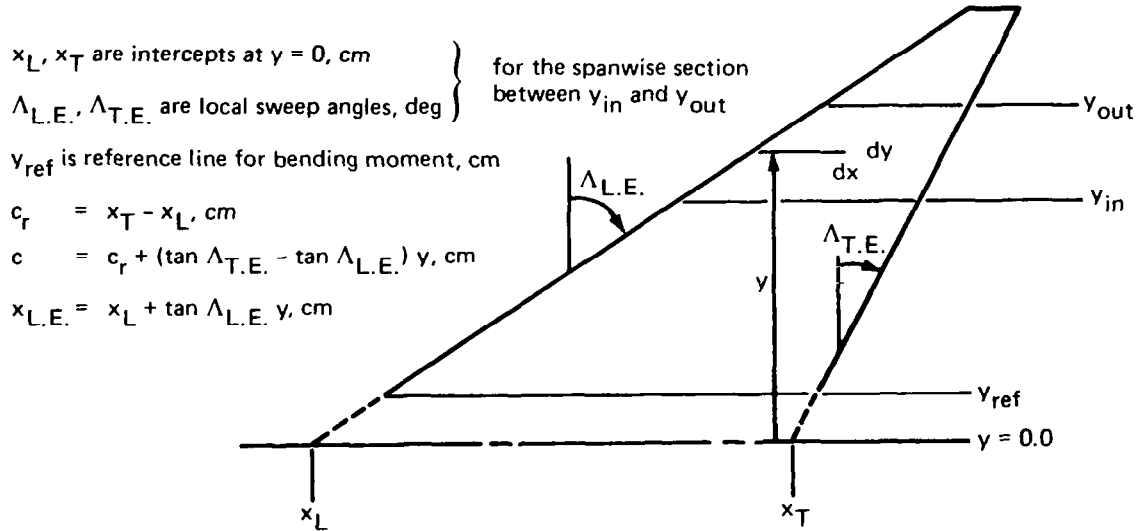
$$C_M = \frac{1}{S\bar{c}} \sum_{k=1}^{N_{SECT}} \left\{ (C_m)_k (S_h^c)_k + (C_n)_k (S_h)_k \left[x_{ref} - (x_{L.E.})_k \right] \right\} \quad (B-14)$$

where

- \bar{c} is reference chord for pitching moment, cm
- x_{ref} is reference station for pitching moment, cm (0.25 M.A.C.)
- $x_{L.E.}$ is leading edge of section chord, cm
- $b/2$ is reference length for bending moment, cm

DETERMINATION OF GEOMETRIC CONSTANTS REQUIRED FOR INTEGRATION

To obtain total surface coefficients, the assumption is made that the section coefficients apply for a finite distance on both sides of each row of orifices. The input geometry required to calculate the areas, and products of area and length required for the summation of total surface coefficients, is shown in the following sketch.



o Section area:

$$\begin{aligned}
 S_h &= \int_{y_{in}}^{y_{out}} \int_{x_L + \tan \Lambda_{L.E.} y}^{x_T + \tan \Lambda_{T.E.} y} dy dx \\
 &= c_r (y_{out} - y_{in}) + 0.5 (\tan \Lambda_{T.E.} - \tan \Lambda_{L.E.}) (y_{out}^2 - y_{in}^2) \quad (B-15)
 \end{aligned}$$

o Product of section area and mean chord:

$$\begin{aligned}
 S_{hc} &= \int_{y_{in}}^{y_{out}} \int_{x_L + \tan \Lambda_{L.E.} y}^{x_T + \tan \Lambda_{T.E.} y} c dy dx \\
 &= c_r^2 (y_{out} - y_{in}) + c_r (\tan \Lambda_{T.E.} - \tan \Lambda_{L.E.}) (y_{out}^2 - y_{in}^2) \\
 &\quad + \frac{(\tan \Lambda_{T.E.} - \tan \Lambda_{L.E.})^2}{3.0} (y_{out}^3 - y_{in}^3) \quad (B-16)
 \end{aligned}$$

- o Product of section area and bending moment arm:

$$\begin{aligned}
 S_{hy} &= \int_{y_{in}}^{y_{out}} \int_{x_L + \tan \Lambda_{L.E.} y}^{x_T + \tan \Lambda_{T.E.} y} (y - y_{ref}) dy dx \\
 &= \frac{c_r - (\tan \Lambda_{T.E.} - \tan \Lambda_{L.E.}) y_{ref}}{2.0} (y_{out}^2 - y_{in}^2) \\
 &\quad + \frac{\tan \Lambda_{T.E.} - \tan \Lambda_{L.E.}}{3.0} (y_{out}^3 - y_{in}^3) - c_r y_{ref} (y_{out} - y_{in}) \quad (B-17)
 \end{aligned}$$

- o Product of section area and leading-edge coordinate:

$$\begin{aligned}
 S_{hx} &= \int_{y_{in}}^{y_{out}} \int_{x_L + \tan \Lambda_{L.E.} y}^{x_T + \tan \Lambda_{T.E.} y} x_{L.E.} dy dx \\
 &= x_L c_r (y_{out} - y_{in}) + \frac{\tan \Lambda_{L.E.} c_r + x_L (\tan \Lambda_{T.E.} - \tan \Lambda_{L.E.})}{2.0} (y_{out}^2 - y_{in}^2) \\
 &\quad + \tan \Lambda_{L.E.} \frac{(\tan \Lambda_{T.E.} - \tan \Lambda_{L.E.})}{3.0} (y_{out}^3 - y_{in}^3) \quad (B-18)
 \end{aligned}$$

- o Total surface reference area:

$$S = \sum_{k=1}^{NSECT} (S_h)_k \quad (B-19)$$

- o M.A.C. and X coordinate of M.A.C. leading edge:

$$\bar{c} = \frac{1}{S} \sum_{k=1}^{NSECT} (S_h^c)_k \quad (B-20)$$

$$x_{L.E., M.A.C.} = \frac{1}{S} \sum_{k=1}^{NSECT} (S_h^x)_k \quad (B-21)$$

The required integration constants for the wing and body are shown in table B-1.

Table B-1.—Integration Constants

Reference area = 3128.45 cm²

M.A.C. = 75.311 cm

Half span = 50.80 cm

Pitching moment referenced to 0.25 M.A.C.

Bending moment referenced to $0.086 \frac{b}{2}$ ($y_{\text{ref}} = 4.374$ cm)

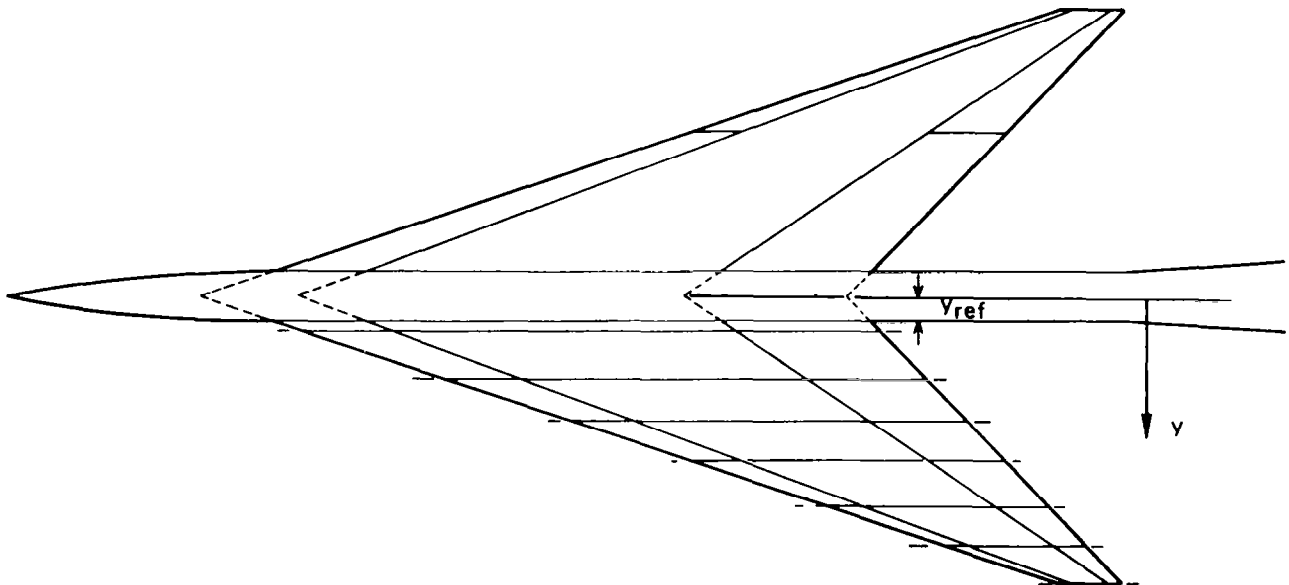
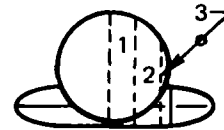
L.E. of M.A.C. at B.S. 87.760 cm

Wing

$2y/b$	$\frac{\Delta y}{(b/2)}$	Area cm ²	Area • chord cm ³	Area • ($y - y_{\text{ref}}$) cm ³
0.09	0.0425	219.69	22 357.	167.
0.20	0.1575	733.51	67 415.	4 206.
0.35	0.1500	580.54	44 374.	7 857.
0.50	0.1400	437.93	27 084.	9 148.
0.65	0.1600	377.64	17 722.	10 729.
0.80	0.1300	210.35	6 794.	7 528.
0.93	0.1400	129.79	2 487.	5 505.

Body

Longitudinal section	Area cm ²	Area • L cm ³
1	356.61	81 258.
2	504.32	114 916.
3	70.94	16 164.



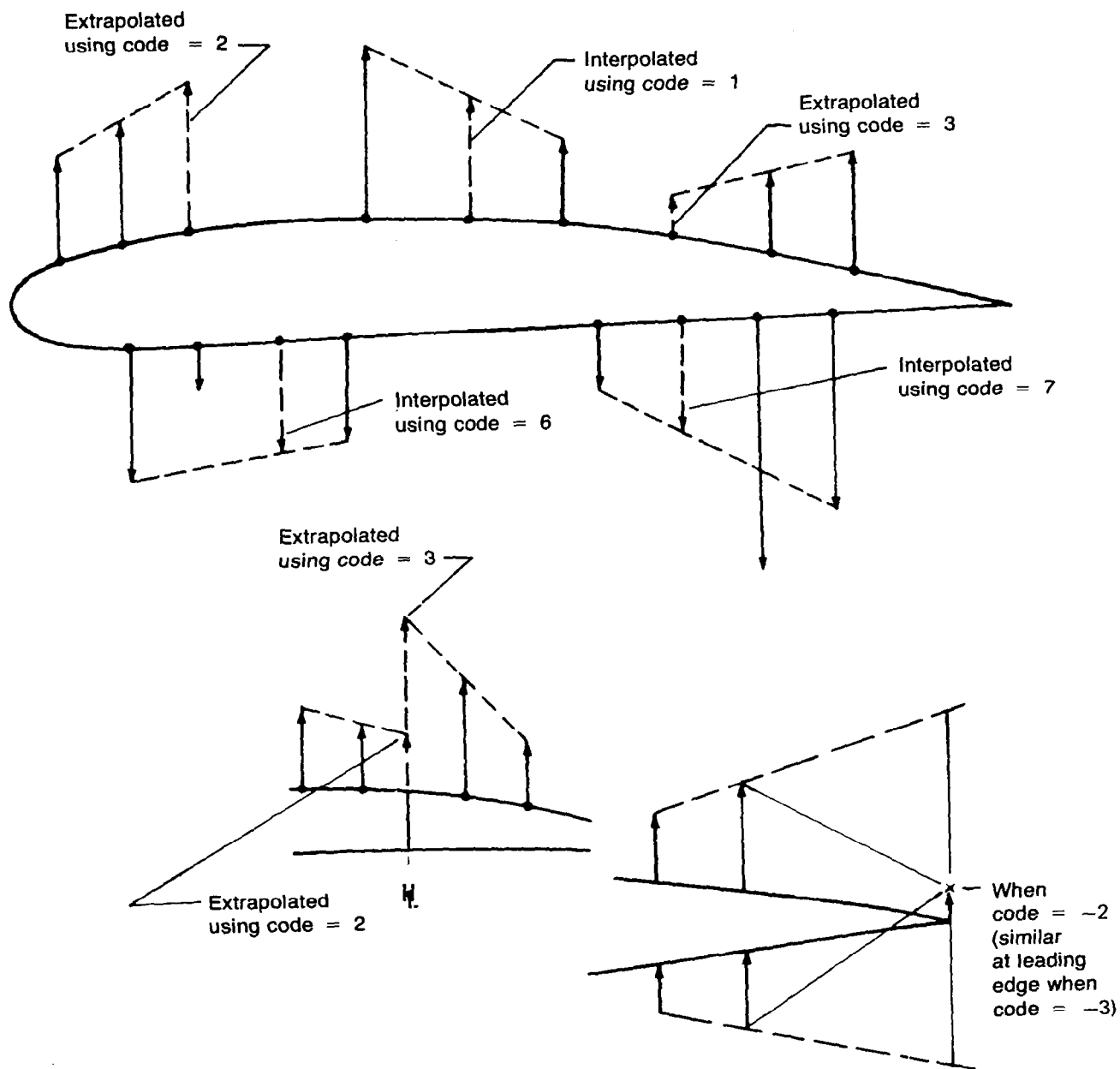


Figure B-1.—Codes Used to Interpolate and Extrapolate

APPENDIX C

METHOD FOR CALCULATING NET LEADING-EDGE SUCTION COEFFICIENTS

The procedure is described for obtaining leading-edge suction coefficients (and therefore leading-edge vortex strength) from the net pressure distribution that is predicted by the linear theory FLEXSTAB. Also explained is a procedure to account for the retarding effect of a rounded-leading edge.

As the pressures for a specific wing shape are used, the effect of wing warp and twist are automatically included.

GENERAL LEADING-EDGE SUCTION CALCULATION PROCEDURE

The leading-edge suction coefficient C_s at each spanwise location can be calculated from the local wing geometry and net lifting pressure distribution as:

$$C_s = \frac{2.0 \pi}{\cos \Lambda} \left[\frac{bc}{2.0 S_{ref}} \right] \left[\tan \Lambda k C_1^2 \right] \quad (C-1)$$

where

- Λ = the local leading-edge sweep angle
- b = wing span
- c = local chord length
- S_{ref} = reference wing area
- k = $\sqrt{1.0 - \left(\frac{M^2 - 1.0}{\tan^2 \Lambda} \right)}$
- M = Mach number
- C_1 = the strength of the net lifting pressure coefficient singularity near the leading edge of the wing
- = $\lim_{\xi \rightarrow 0} \frac{C_{p,net}}{4.0} \sqrt{\xi}$ (C-2)
- $C_{p,net}$ = net lifting pressure; wing lower surface pressure minus upper surface pressure
- ξ = $(x - x_{LE})/c$, fraction of local chord
- $x - x_{LE}$ = local streamwise distance from the wing leading edge

The net lifting pressure coefficient can be approximated by a simple fractional polynomial equation in terms of the fraction of local chord ξ as:

$$\frac{C_{p,net}}{4.0} = \frac{C_1}{\sqrt{\xi}} + C_2 \xi^{1/2} + C_3 \xi^{3/2} + \dots \quad (C-3)$$

This equation provides a direct relationship between the net lifting pressures and the leading-edge pressure singularity, C_1 .

In principle, C_1 could be determined by a least squares curve fit of equation (C-3) to the $C_{p,net}$ distribution calculated by the FLEXSTAB program. However, the FLEXSTAB-calculated pressures near the wing leading edge are uncertain because of the inability of a constant-pressure-panel method to properly represent the leading-edge singularity. The pressures do tend to converge to the exact values farther aft on the wing chord. The irregularities of the calculated pressures make it difficult to accurately determine C_1 by this procedure. The fact that integration tends to smooth numerical irregularities of a calculated function, is utilized to calculate C_1 .

Integrating equation (C-3) provides an approximate function for the local integrated load distribution as:

$$\int_0^{\xi} \frac{C_{p,net}}{4.0} d\xi = 2.0 C_1 \sqrt{\xi} + \frac{2.0}{3.0} C_2 \xi^{3/2} + \frac{2.0}{5.0} C_3 \xi^{5/2} + \dots \quad (C-4)$$

Define the function $g(C_p)$ as:

$$g(C_p) = \frac{\int_0^{\xi} \frac{C_{p,net}}{4.0} d\xi}{2.0 \sqrt{\xi}} = \frac{\int_0^{\xi} C_{p,net} d\xi}{8.0 \sqrt{\xi}} \quad (C-5)$$

Combining equations (C-4) and (C-5) provides an approximating function for $g(C_p)$ as:

$$g(C_p) = C_1 + \frac{1.0}{3.0} C_2 \xi + \frac{1.0}{5.0} C_3 \xi^2 + \dots \quad (C-6)$$

The leading-edge pressure singularity C_1 can be determined by integrating the FLEXSTAB pressures successively back to the aft edge of each panel to obtain the

distribution of $g(C_p)$ over the wing chord. The approximating equation (C-6) is then "fit" to the calculated values of $g(C_p)$ by a least squares approach.

Typically, if the values of $g(C_p)$ back to approximately 25-percent chord are used, a simple quadratic equation for $g(C_p)$ is adequate (i.e., use the first three terms on the right-hand side of equation (C-6)).

FLEXSTAB uses constant pressure panels to represent the wing pressure distribution. Therefore, the value of $g(C_p)$ back to the aft edge of panel j (that is, for ξ_j) can be represented by a summation:

$$g(C_p) = \frac{\int_0^{\xi_j} C_{p,net} d\xi}{8.0 \sqrt{\xi_j}} = \frac{\sum_{i=1}^{j-1} [C_{p,net}]_i [\xi_i - \xi_{i-1}]}{8.0 \sqrt{\xi_j}} \quad (C-7)$$

The procedure for this evaluation is illustrated in figure C-1. It should be noted that the fraction of local chord ξ used in this evaluation is that of the aft edge of each panel.

The leading-edge suction distribution for a specific combination of wing shape, Mach number, and angle of attack can be calculated as follows:

1. Calculate the net lifting pressures for the specified wing geometry at the desired Mach number and angle of attack.
2. Calculate the corresponding $g(C_p)$ values at each semispan station where the pressures are obtained, using equation (C-5) or (C-7).
3. "Least squares fit" equation (C-6) to the calculated $g(C_p)$ values on the forward 25 to 30 percent of each wing section to determine C_1 (at least five or six values of $g(C_p)$ should be used).
4. Use equation (C-1) to determine the local leading-edge suction coefficient.

ANGLE OF ATTACK SCALING

FLEXSTAB lifting pressures vary linearly with angle of attack. The local leading-edge singularity at any angle of attack can be obtained by linear interpolation from any two known data sets for the same wing shape and Mach number. The full leading-edge suction coefficient can then be calculated using equation (C-1).

LEADING-EDGE VORTEX DEVELOPMENT AND NET SUCTION CALCULATION

A method for predicting the retarding effect of rounded-nose airfoils on the progressive development of leading-edge vortices on highly swept wings is presented in references 18 and 19. The leading-edge vortex is assumed to be present at any station on the wing when the local leading-edge suction coefficient C_s is greater than the local airfoil nose pressure force coefficient.

It is shown in reference 19, that the leading-edge vortex starts at a particular spanwise station η when

$$C_1 = C_{1,R}$$

where:

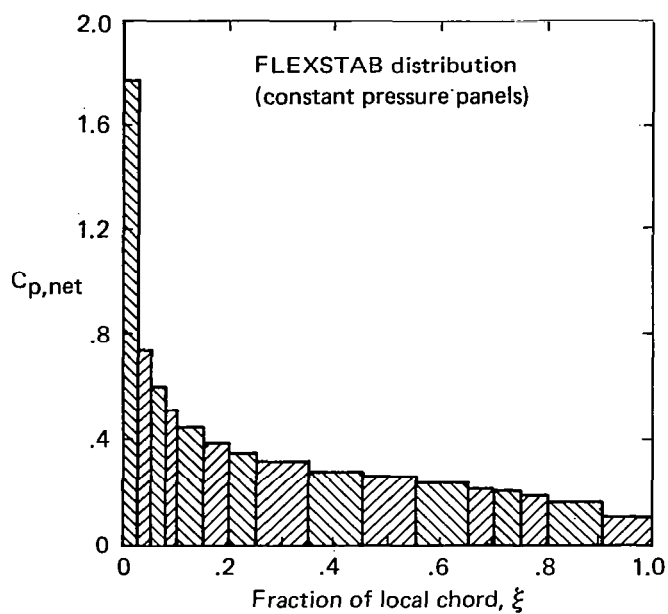
$$C_{1,R} = \frac{\pm \sqrt{\frac{R_{\perp}}{2.0 c}}}{k \tan \Lambda} \quad (C-8)$$

$\frac{R_{\perp}}{c}$ is the ratio of the airfoil nose radius (perpendicular to the wing leading edge), to the local streamwise chord.

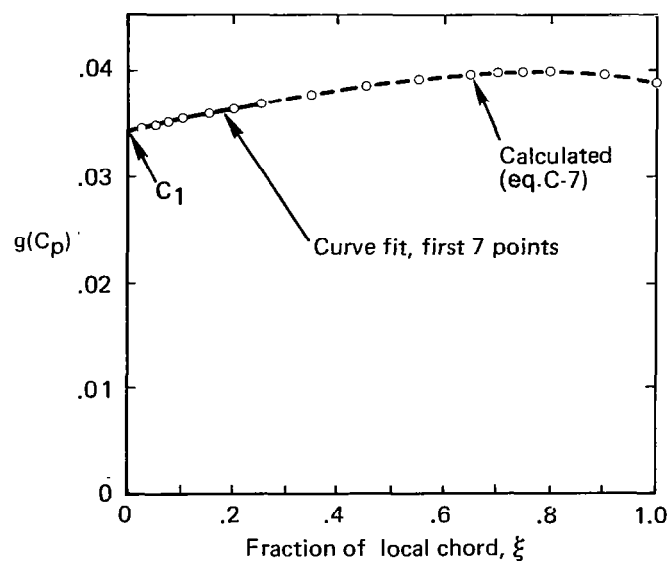
The perpendicular nose radius to streamwise chord ratio can be obtained approximately from the local streamwise chord ratio R_s/c as

$$\frac{R_{\perp}}{c} = \frac{1.0}{\cos \Lambda} \frac{R_s}{c} \quad (C-9)$$

The net leading-edge suction coefficient is calculated using equation (C-1) by replacing the term C_1 with the term $C_1 - C_{1,R}$.



Panel	ξ	$C_{p,net}$	$g(C_p)$
1	.025	1.7942	.035461
2	.050	.7461	.035502
3	.075	.6064	.035907
4	.100	.5126	.036162
5	.150	.4507	.036799
6	.200	.3865	.037270
7	.250	.3497	.037707
8	.350	.3204	.038638
9	.450	.2858	.039401
10	.550	.2619	.040054
11	.650	.2398	.040562
12	.700	.2180	.040715
13	.750	.2066	.040826
14	.800	.1897	.040855
15	.900	.1656	.040700
16	1.0	.1047	.039920



A least-squares curve fit of
equation (C-6) yields:

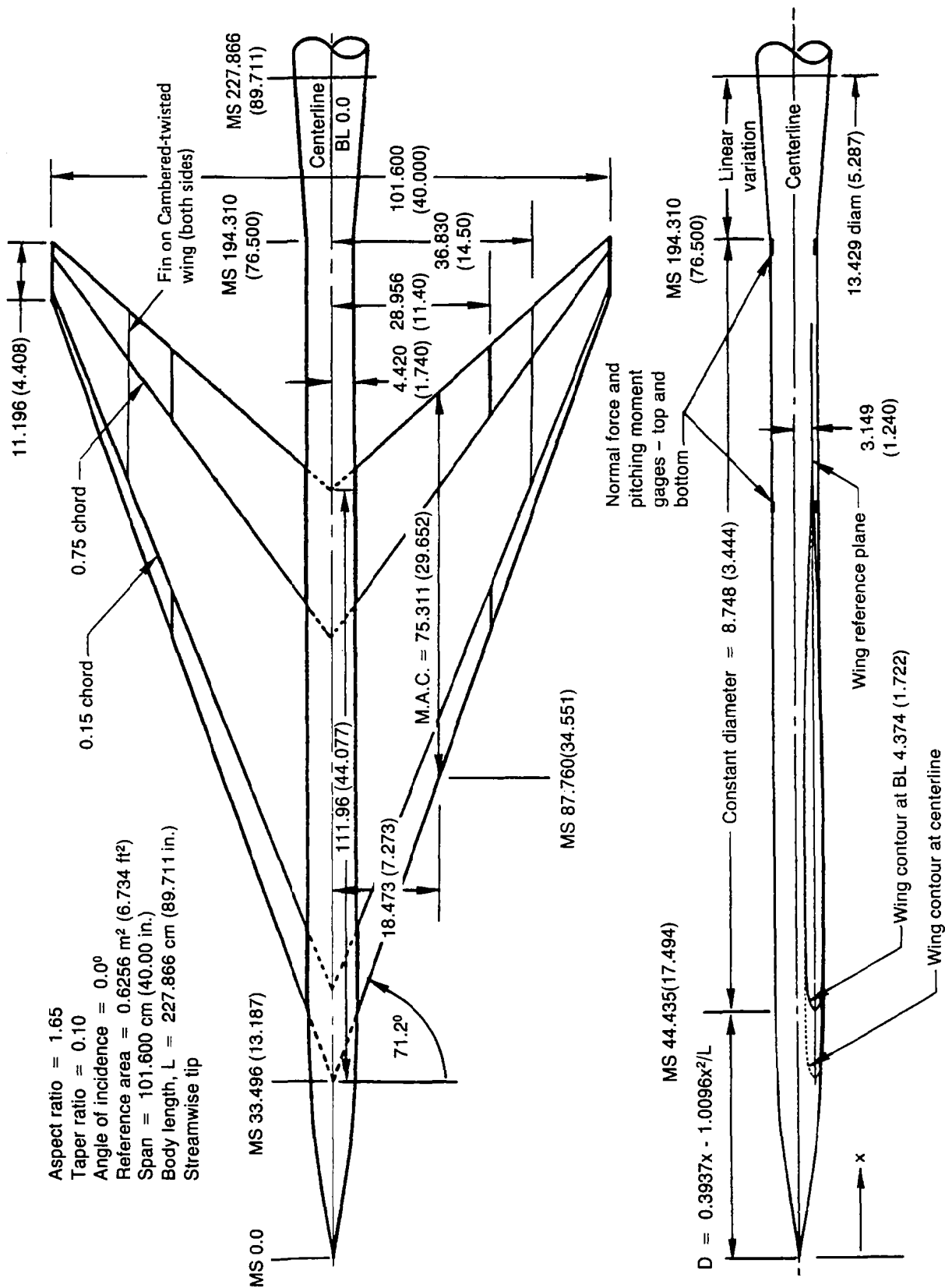
$$\begin{aligned} C_1 &= 0.035059 \\ C_2 &= 0.035244 \\ C_3 &= -0.020560 \end{aligned}$$

Figure C-1.—Sample Calculation of C_1 , Flat Wing, $M = 0.85$, $\alpha = 10^\circ$, $\eta = 0.319$

REFERENCES

1. Manro, Marjorie E.; Tinoco, Edward N.; Bobbitt, Percy J.; and Rogers, John T.: Comparisons of Theoretical and Experimental Pressure Distributions on an Arrow-Wing Configuration at Transonic Speeds. Aerodynamic Analyses Requiring Advanced Computers - Part II, NASA SP-347, 1975, pp. 1141-1188.
2. Manro, M. E.; Bobbitt, P. J.; and Rogers, J. T.: Comparisons of Theoretical and Experimental Pressure Distributions on an Arrow-Wing Configuration at Subsonic, Transonic, and Supersonic Speeds. Prediction of Aerodynamic Loading. AGARD CP-204, Feb. 1977, pp. 11-1 - 11-14.
3. Bobbitt, Percy J.; and Manro, Marjorie E.: Theoretical and Experimental Pressure Distributions for a 71.2° Swept Arrow-Wing Configuration at Subsonic, Transonic, and Supersonic Speeds. Proceedings of the SCAR Conference - Part 1, NASA CP-001, 1977, pp. 85-122.
4. Manro, Marjorie E.; Manning, Kenneth J. R.; Hallstaff, Thomas H.; and Rogers, John T.: Transonic Pressure Measurements and Comparison of Theory to Experiment for an Arrow-Wing Configuration - Summary Report. NASA CR-2610, 1976.
5. Manro, Marjorie E.; Manning, Kenneth J. R.; Hallstaff, Thomas H.; and Rogers, John T.: Transonic Pressure Measurements and Comparison of Theory to Experiment for an Arrow-Wing Configuration, Volume I: Experimental Data Report - Base Configuration and Effects of Wing Twist and Leading-Edge Configuration. NASA CR-132727, 1975.
6. Manro, Marjorie E.; Manning, Kenneth J. R.; Hallstaff, Thomas H.; and Rogers, John T.: Transonic Pressure Measurements and Comparison of Theory to Experiment for an Arrow-Wing Configuration, Volume II: Experimental Data Report - Effects of Control Surface Deflection. NASA CR-132728, 1975.
7. Manro, Marjorie E.; Manning, Kenneth J. R.; Hallstaff, Thomas H.; and Rogers, John T.: Transonic Pressure Measurements and Comparison of Theory to Experiment for an Arrow-Wing Configuration, Volume III: Data Report - Comparison of Attached Flow Theories to Experiment. NASA CR-132729, 1975.
8. Manro, M. E.: Supersonic Pressure Measurements and Comparison of Theory to Experiment for an Arrow-Wing Configuration. NASA CR-145046, 1976.
9. Manro, Marjorie E.: Transonic Pressure Measurements and Comparison of Theory to Experiment for Three Arrow-Wing Configurations - Summary Report. NASA CR-3434, 1982.
10. Manro, Marjorie E.: Transonic Pressure Measurements and Comparisons of Theory to Experiment for Three Arrow-Wing Configurations, Volume I: Experimental Data Report - Basic Data and Effect of Wing Shape. NASA CR-165701, 1981.

11. Manro, Marjorie E.: Transonic Pressure Measurements and Comparisons of Theory to Experiment for Three Arrow-Wing Configurations, Volume II: Experimental Data Report – Effect of Trailing-Edge Control Surface Deflection and a Wing Fin. NASA CR-165702, 1981.
12. Manro, Marjorie E.: Transonic Pressure Measurements and Comparisons of Theory to Experiment for Three Arrow-Wing Configurations, Volume III: Data Report – Comparison of Attached-Flow Theories to Experiment. NASA CR-165703, 1981.
13. Polhamus, E. C.: Predictions of Vortex Lift Characteristics by a Leading-Edge Suction Analogy. *Journal of Aircraft*, vol. 8, no. 4, April 1971, pp. 193-199.
14. Tinoco, E. N.; and Mercer, J. E.: FLEXSTAB – A Summary of the Functions and Capabilities of the NASA Flexible Airplane Analysis Computer System. NASA CR-2564, October 1975.
15. Woodward, F. A.; Tinoco, E. N.; and Larsen, J. W.: Analysis and Design of Supersonic Wing-Body Combinations, Including Flow Properties in the Near Field, Part I – Theory and Application. NASA CR-73106, 1967.
16. Woodward, F. A.: Analysis and Design of Wing-Body Combinations at Subsonic and Supersonic Speeds. *Journal of Aircraft*, vol. 5, no. 6, November-December 1968, pp. 528-534.
17. Dusto, A. R., et al.: A Method for Predicting the Stability Characteristics of an Elastic Airplane. Volume 1 – FLEXSTAB Theoretical Description. NASA CR-114712, 1974.
18. Kulfan, R. M.: Wing Airfoil Shape Effects on the Development of Leading-Edge Vortices. AIAA Paper No. 79-1675, August 1979.
19. Kulfan, R. M.: Wing Geometry Effects on Leading-Edge Vortices. AIAA Paper No. 79-1872, August 1979.



All dimensions in centimeters (inches)

Figure 1.-General Arrangement and Characteristics

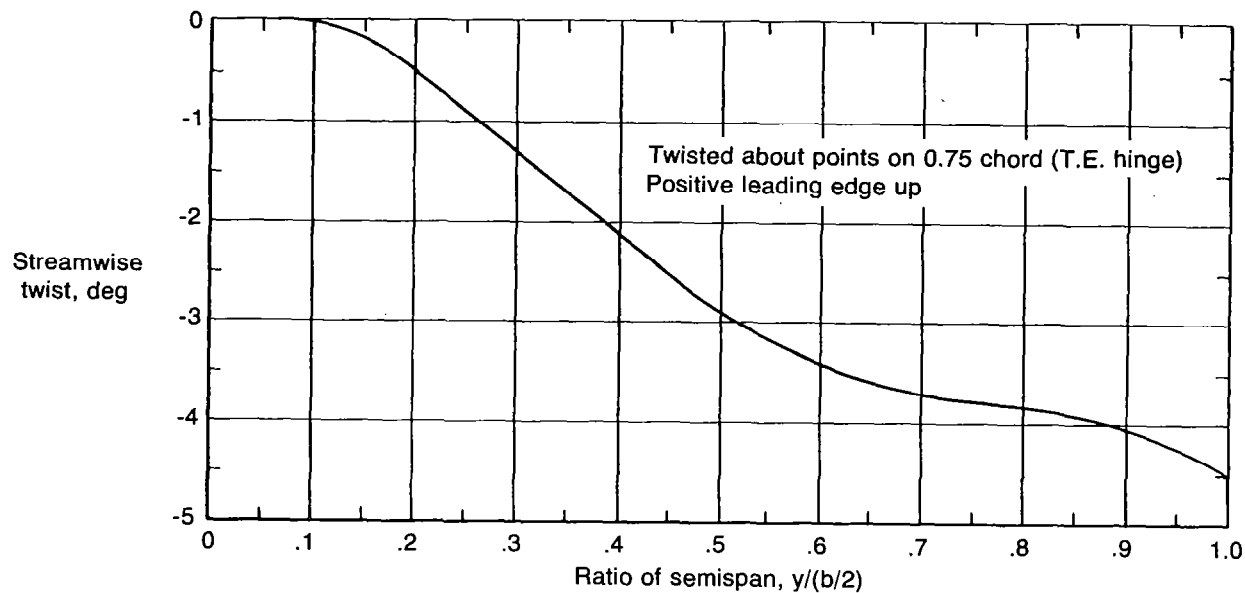


Figure 2.—Spanwise Twist Distribution for the Model Wing

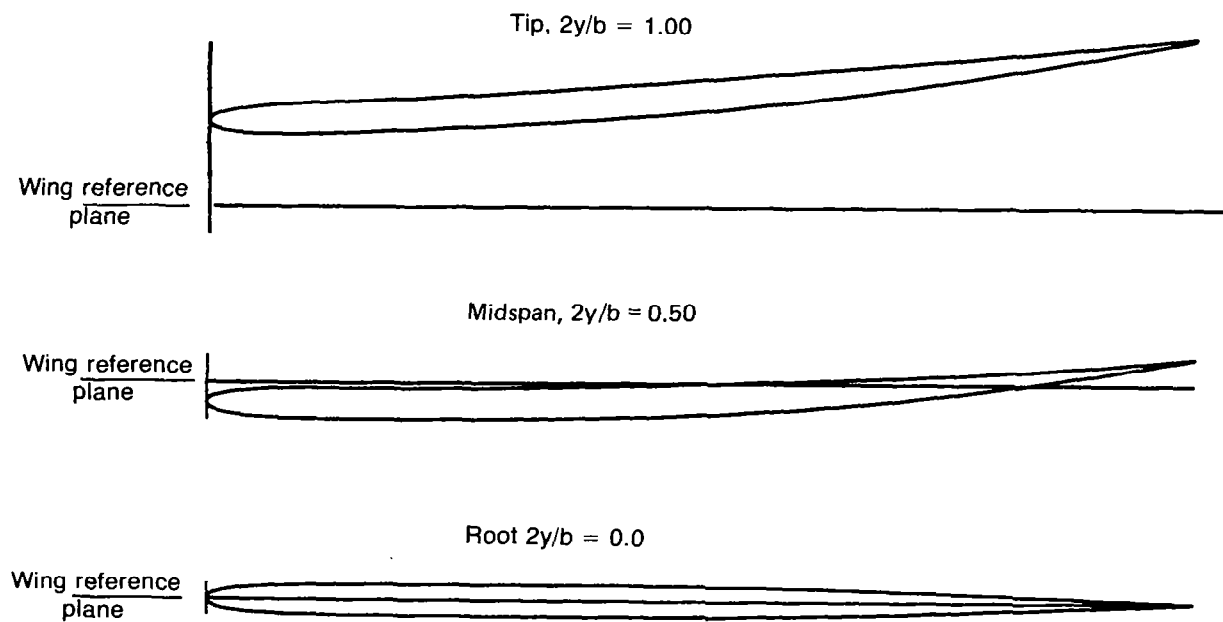


Figure 3.—Cambered-Twisted Wing Section Geometry

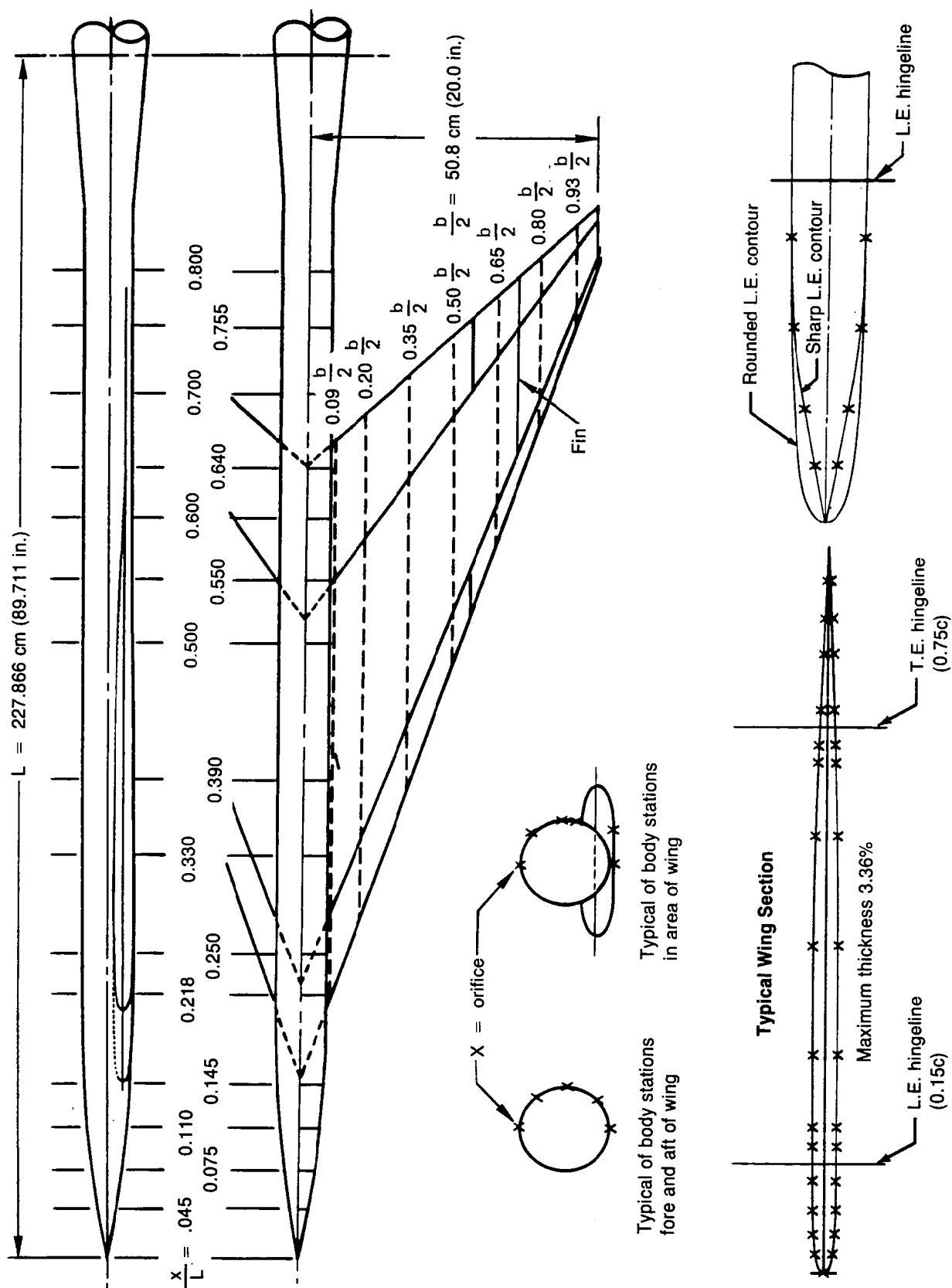


Figure 4.—Pressure Orifice Locations

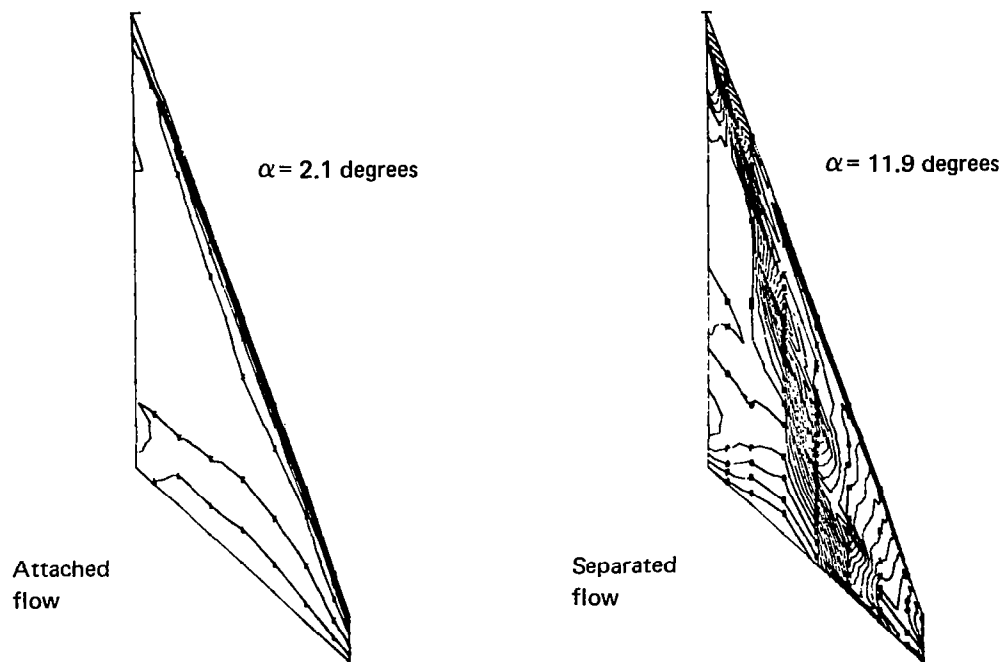


Figure 5.—Upper Surface Isobars, Flat Wing, Rounded Leading Edge, $M = 0.85$

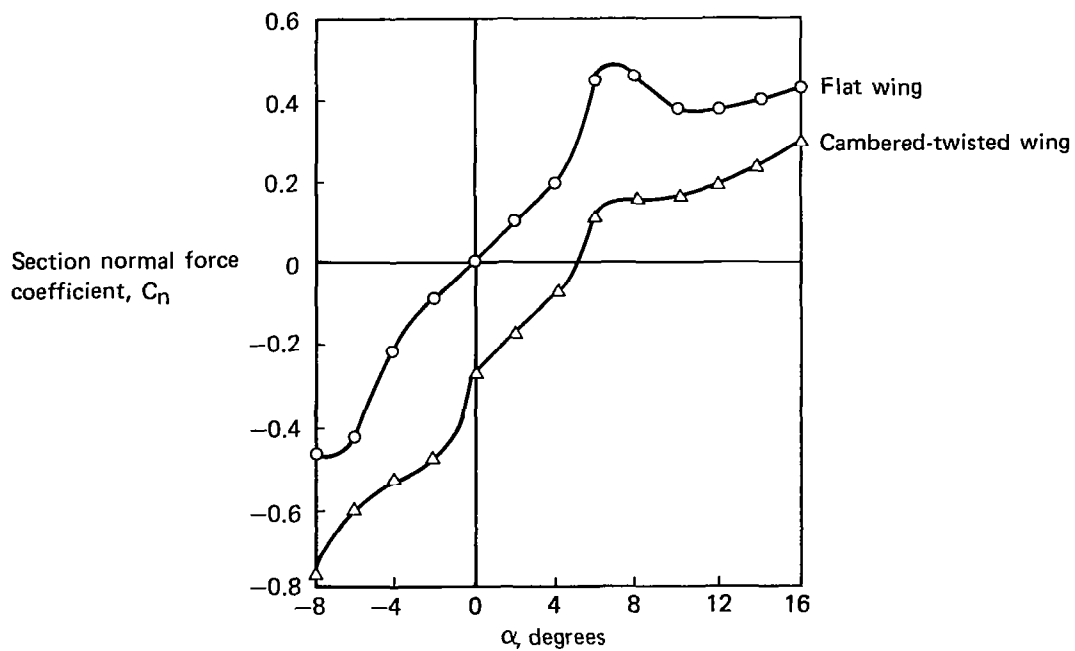
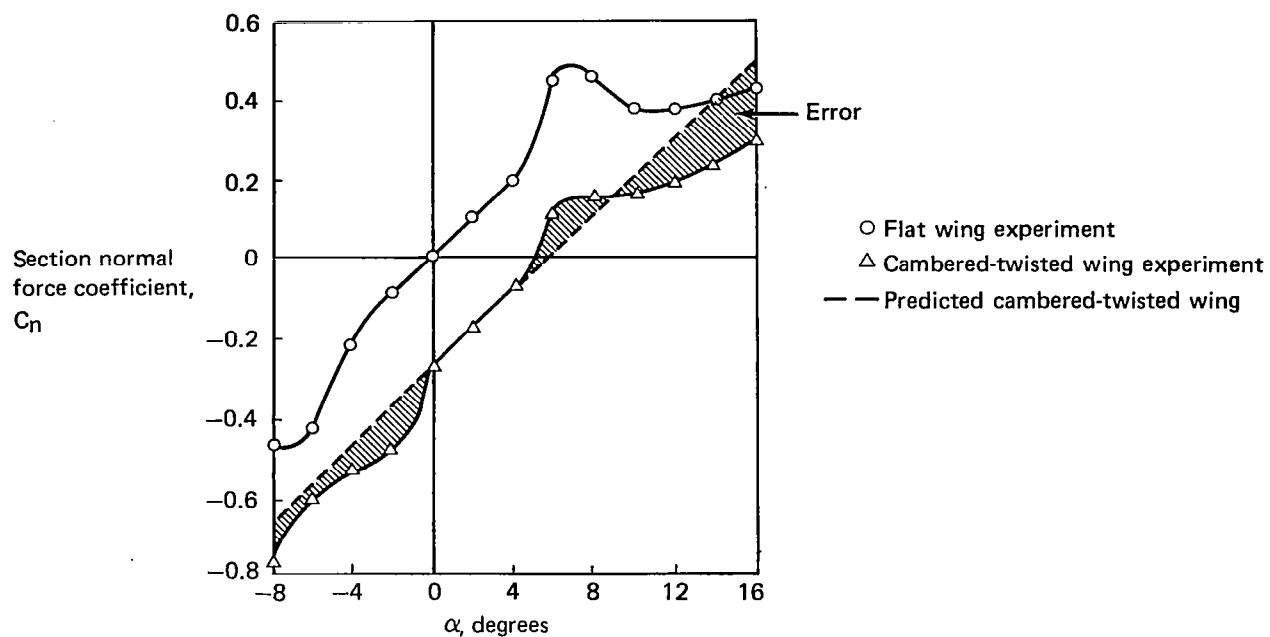
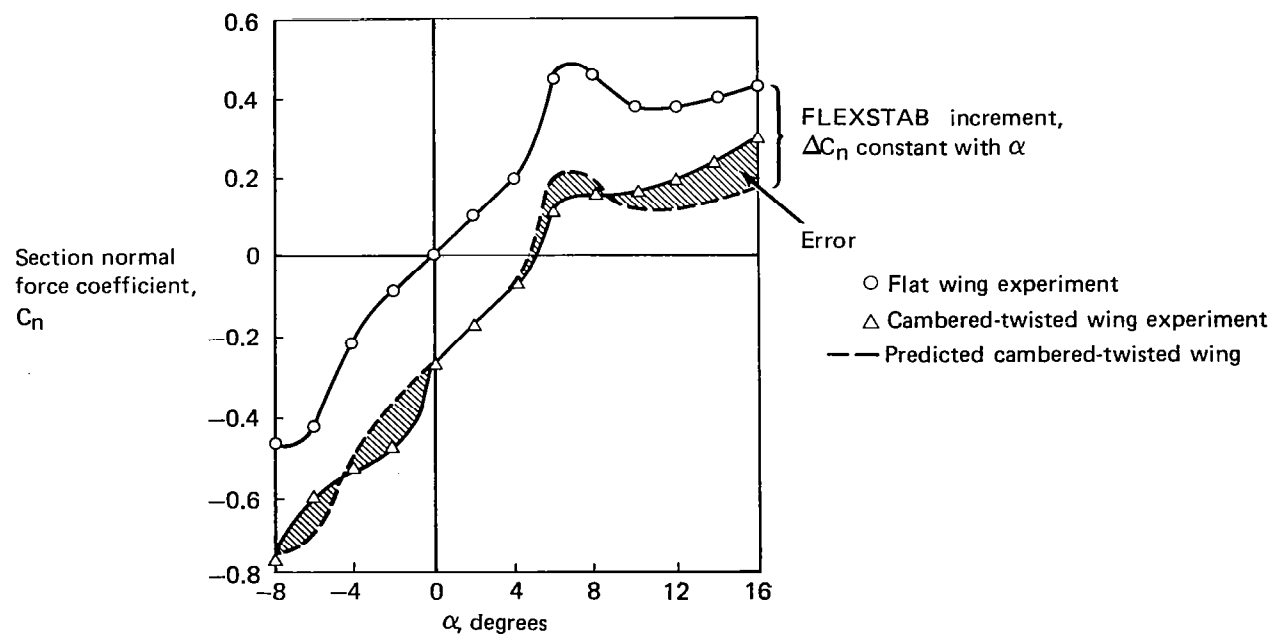


Figure 6.—Comparison of Experimental Section Normal Force Coefficients for Two Wing Shapes, $M = 0.85$, $\eta = 0.80$



(a) Prediction Using Linear Theory, FLEXSTAB



(b) Prediction Using Linear Theory, FLEXSTAB, for Increment to Flat Wing Data

Figure 7.—Typical Procedures Used for Aerolastic Loads Prediction, $M = 0.85$, $\eta = 0.80$

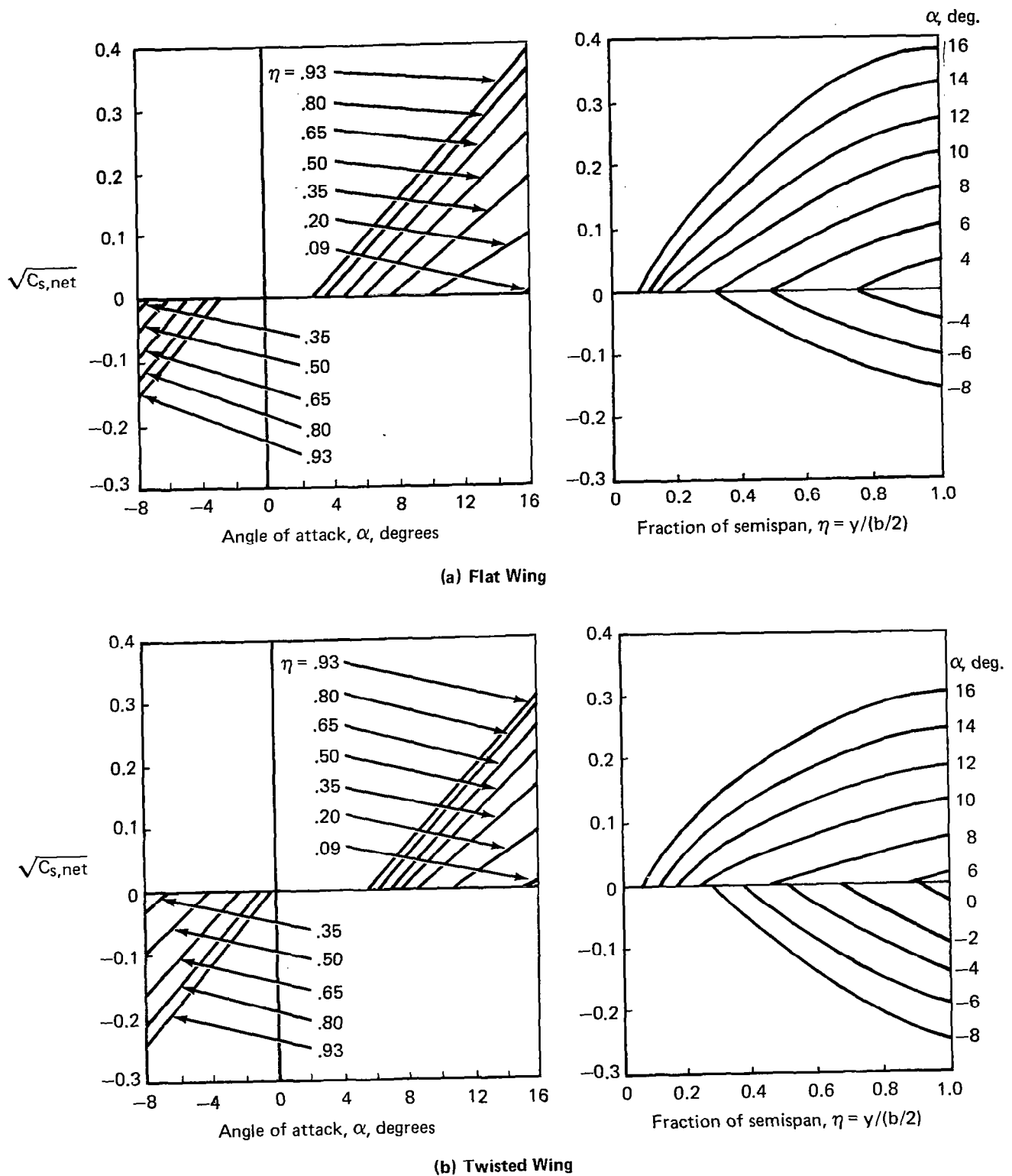
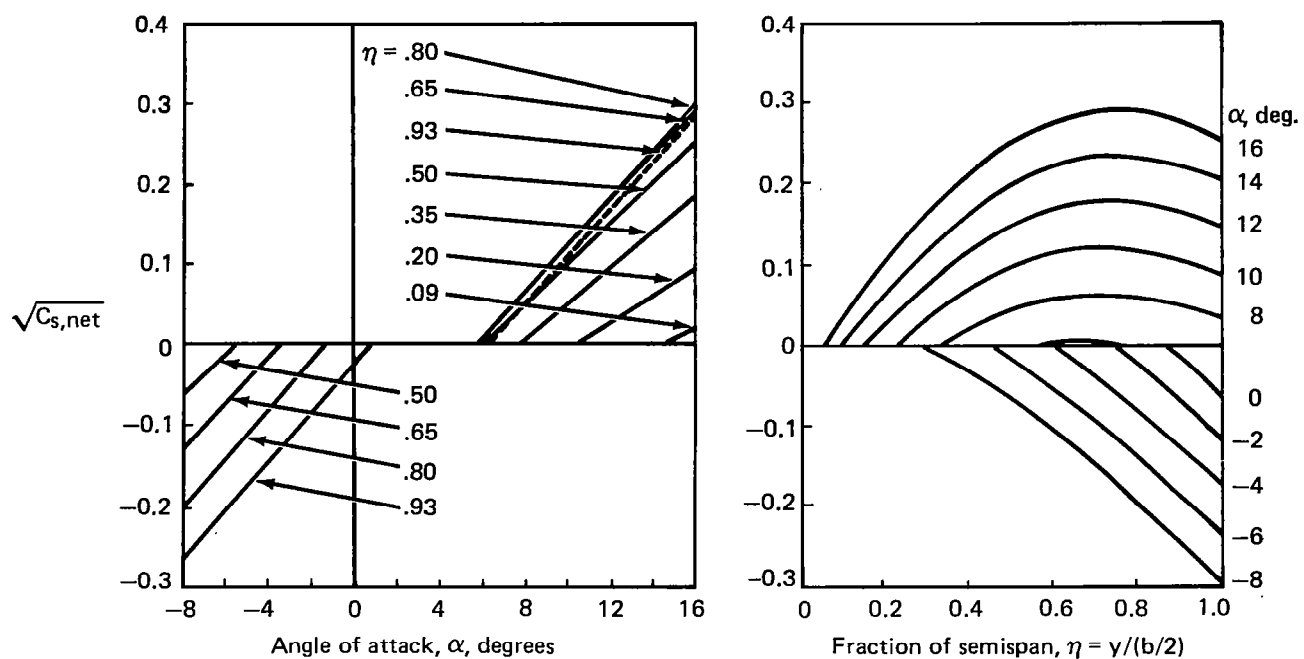


Figure 8.—Net Leading-Edge Suction Coefficients for the Three Wing Shapes, Rounded Leading Edge, $M = 0.85$, Calculated From FLEXSTAB Pressures



(c) Cambered-twisted Wing

Figure 8.—(Concluded)

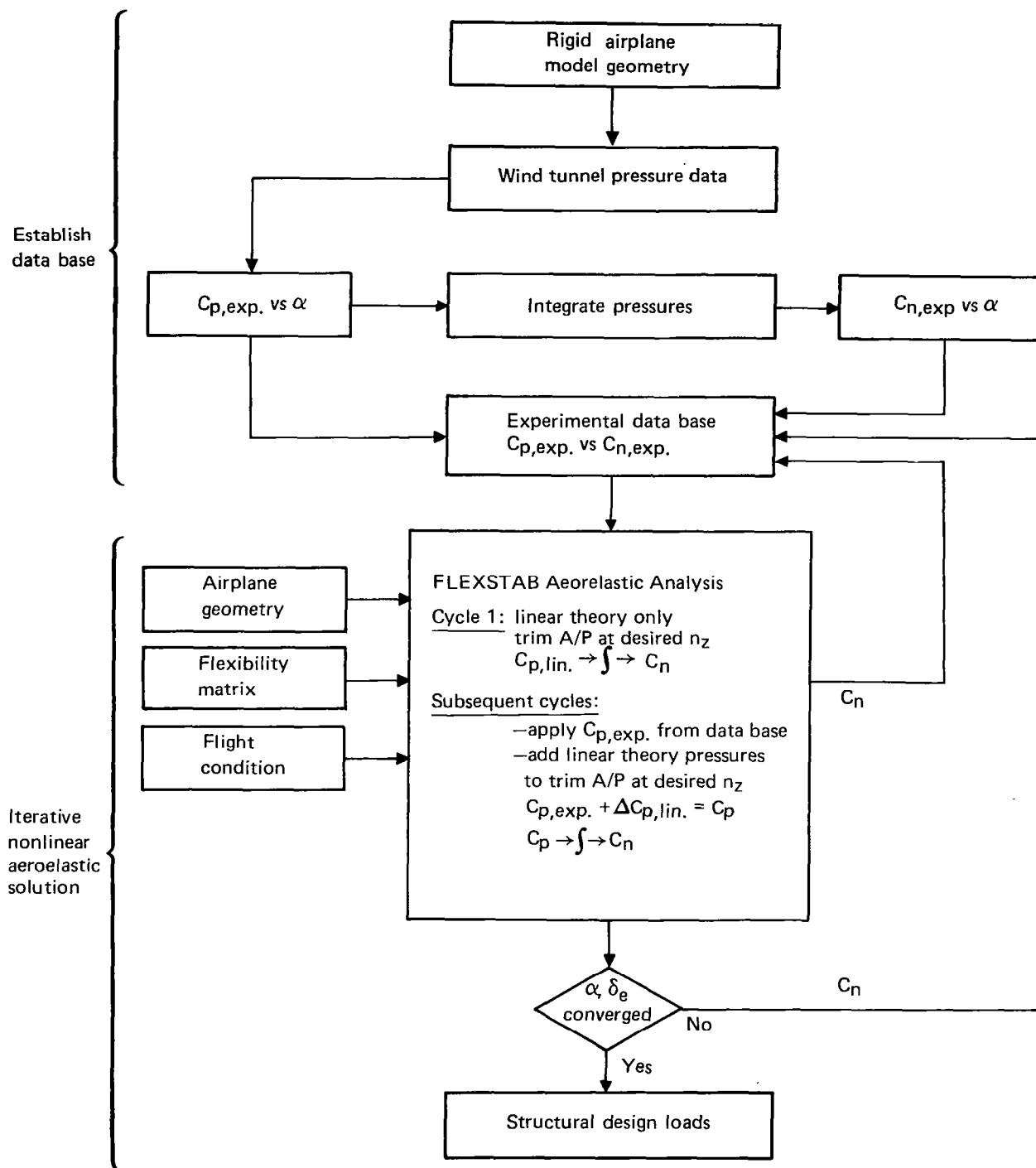


Figure 9.—Proposed Iterative Aeroelastic Loads Prediction Method Based on Section Normal Force Coefficient

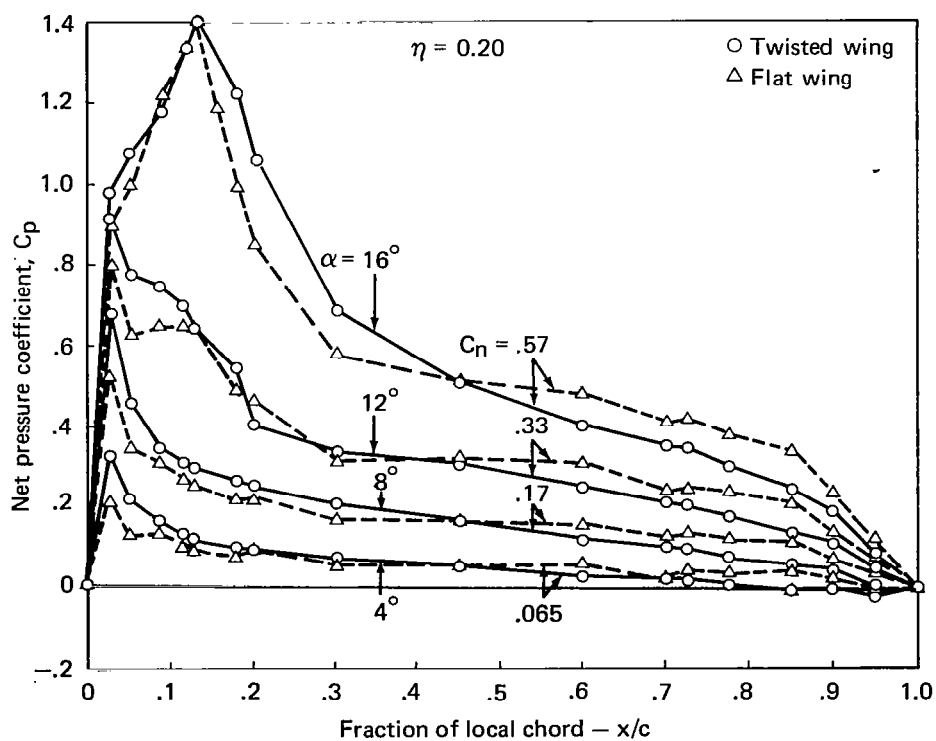
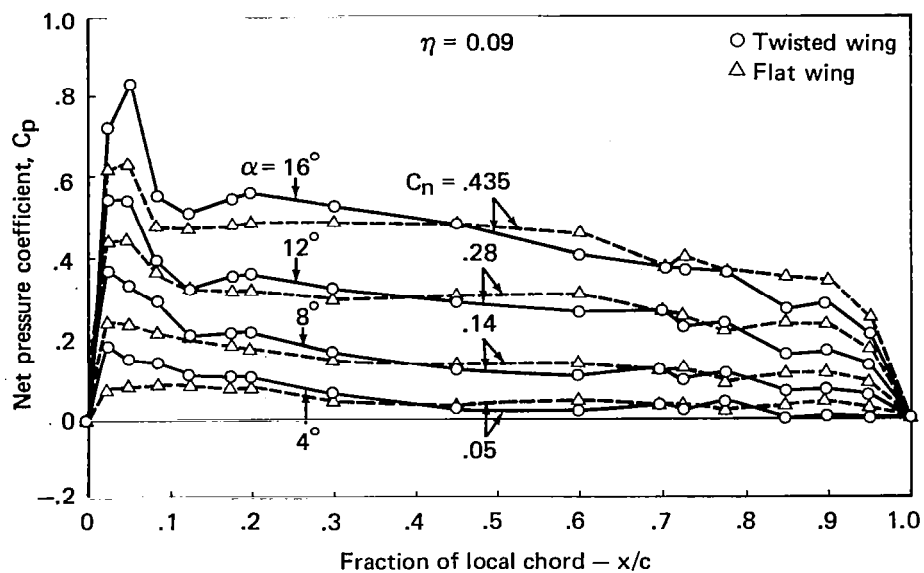


Figure 10.—Chordwise Pressure Distributions Which Produce the Same Section Normal Force Coefficient, Flat and Twisted Wings, $M = 0.85$

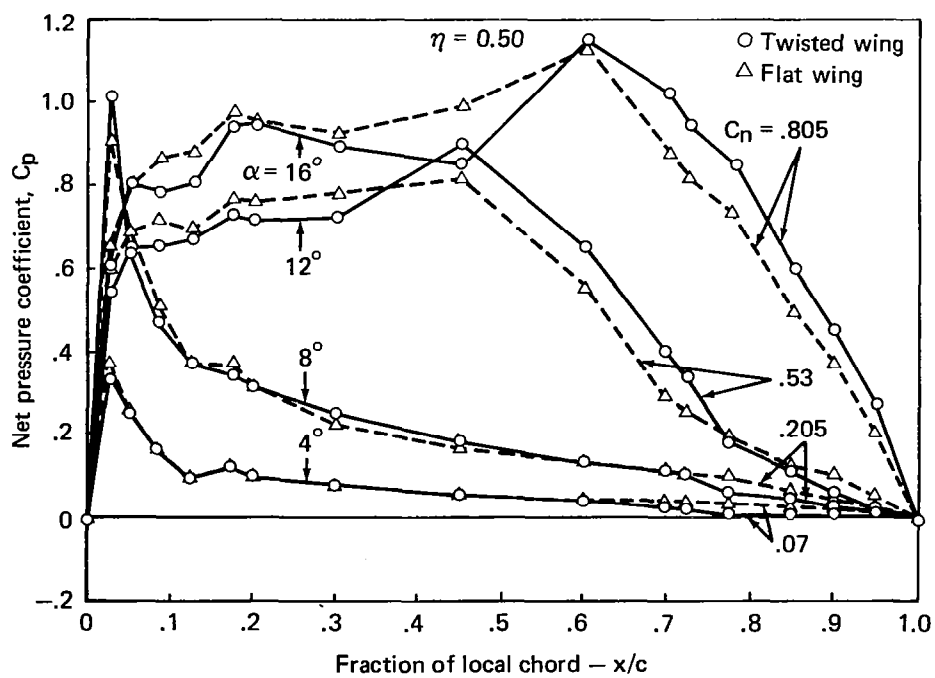
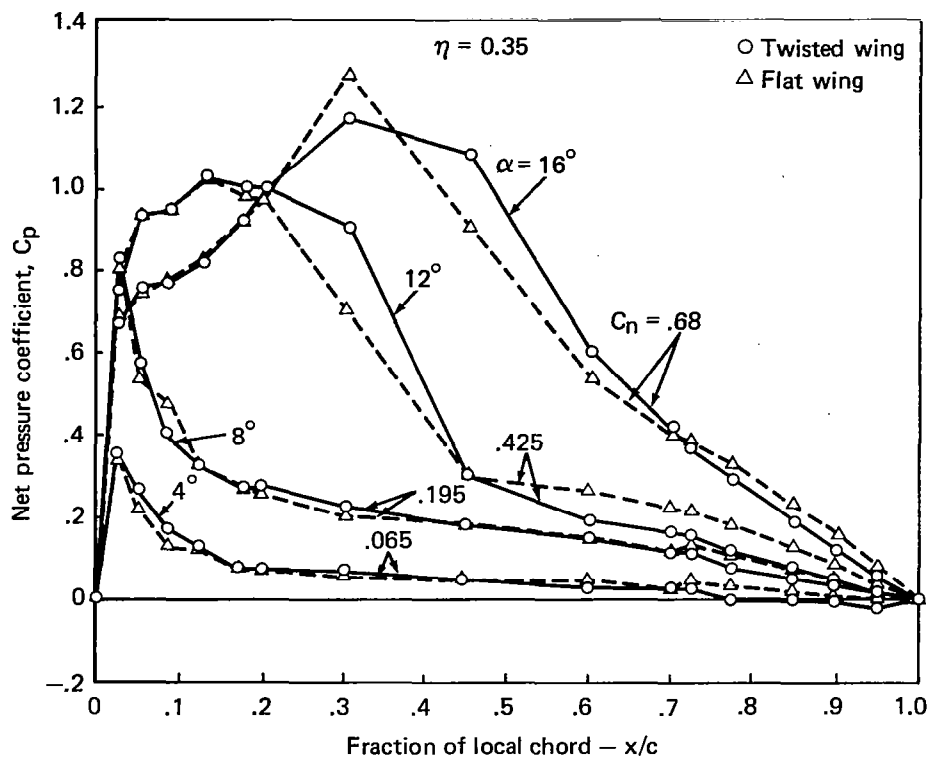


Figure 10.—(Continued)

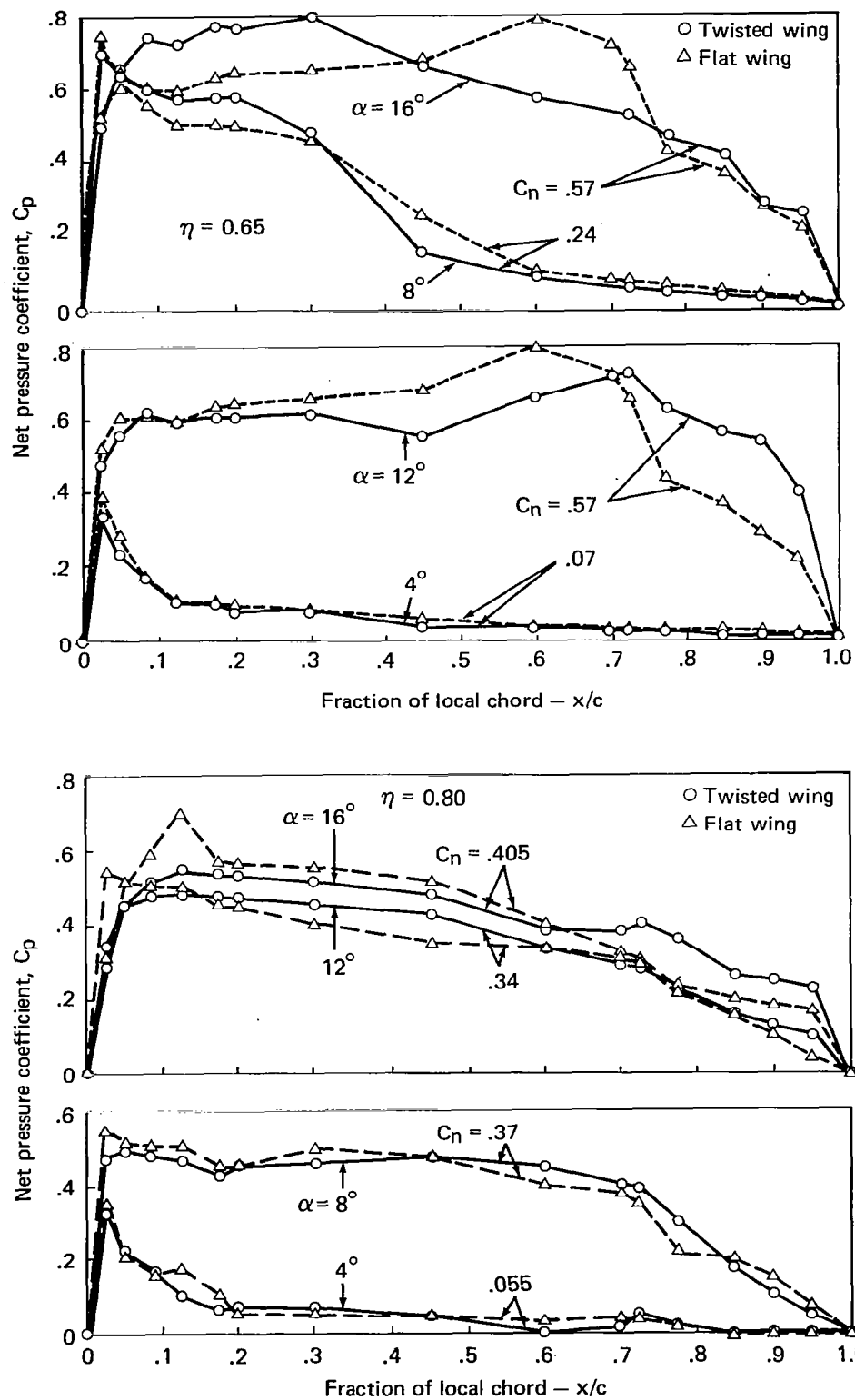


Figure 10.—(Continued)

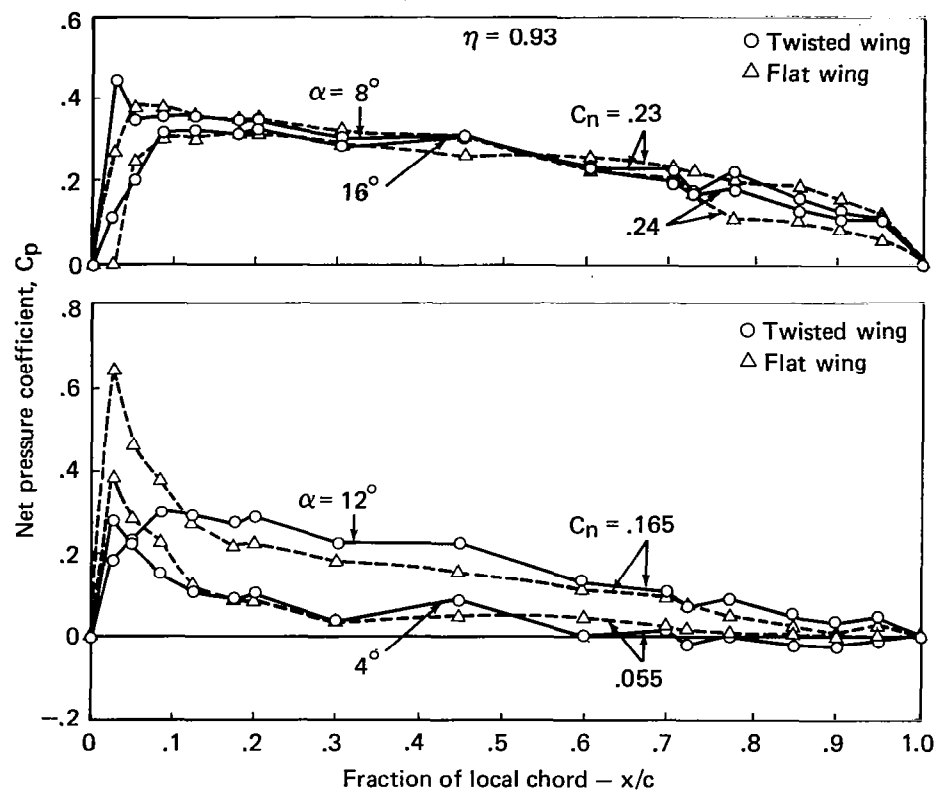


Figure 10.—(Concluded)

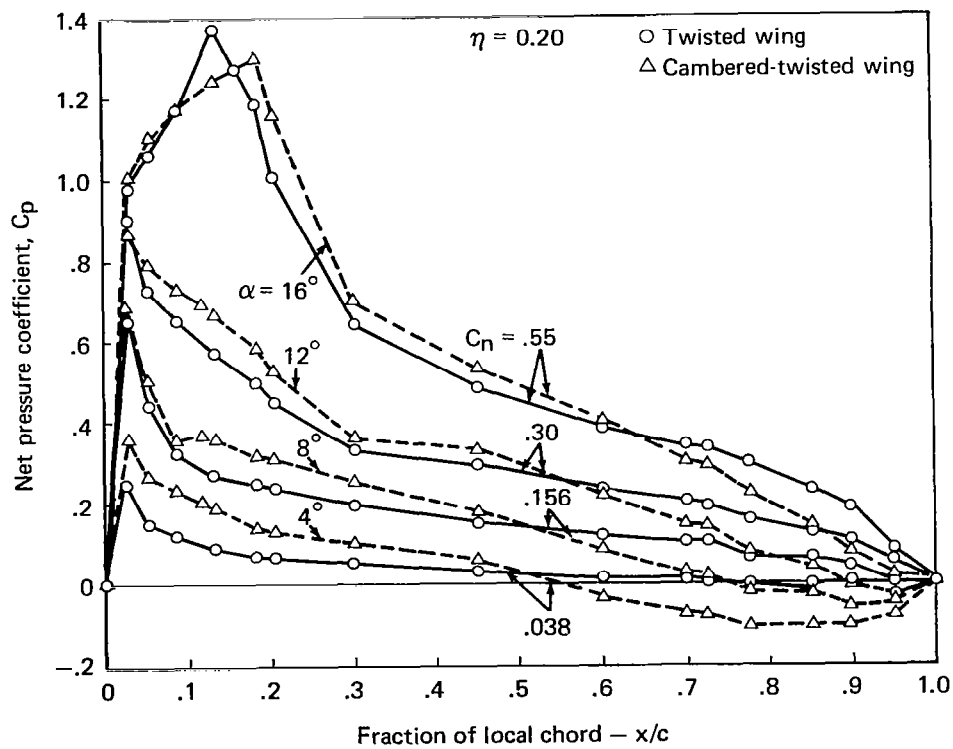
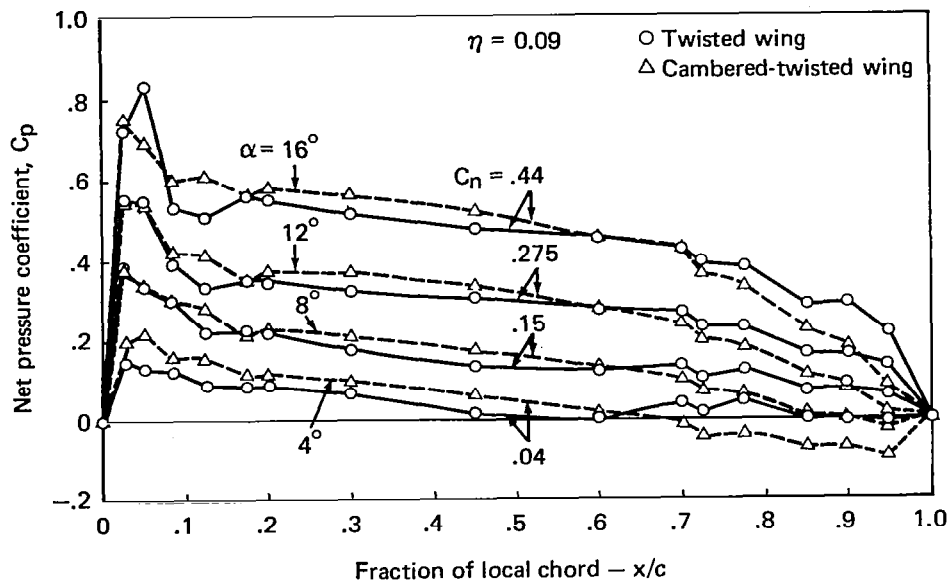


Figure 11.—Chordwise Pressure Distributions Which Produce the Same Section Normal Force Coefficient, Twisted and Cambered-Twisted Wings, $M = 0.85$

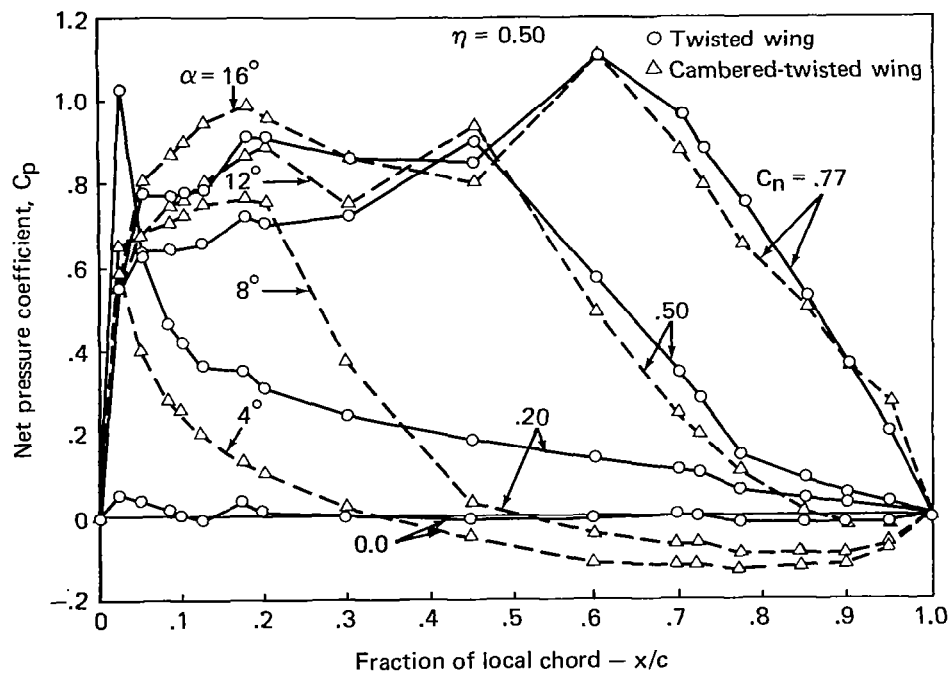
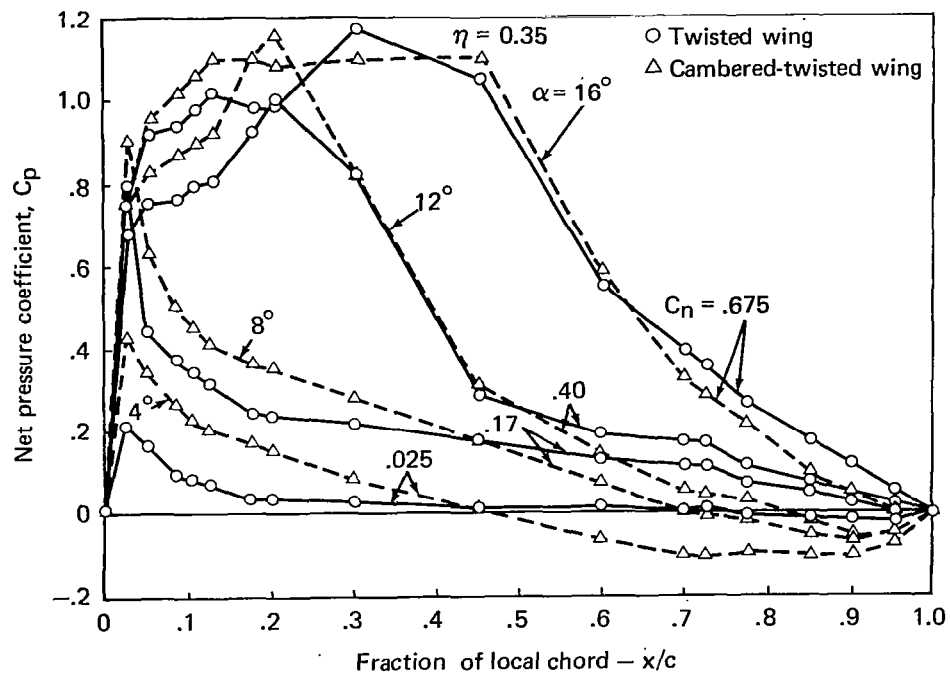


Figure 11.—(Continued)

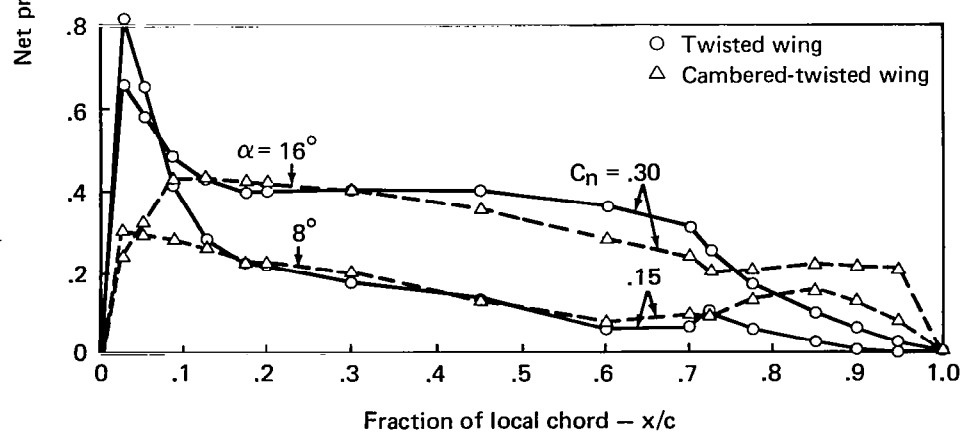
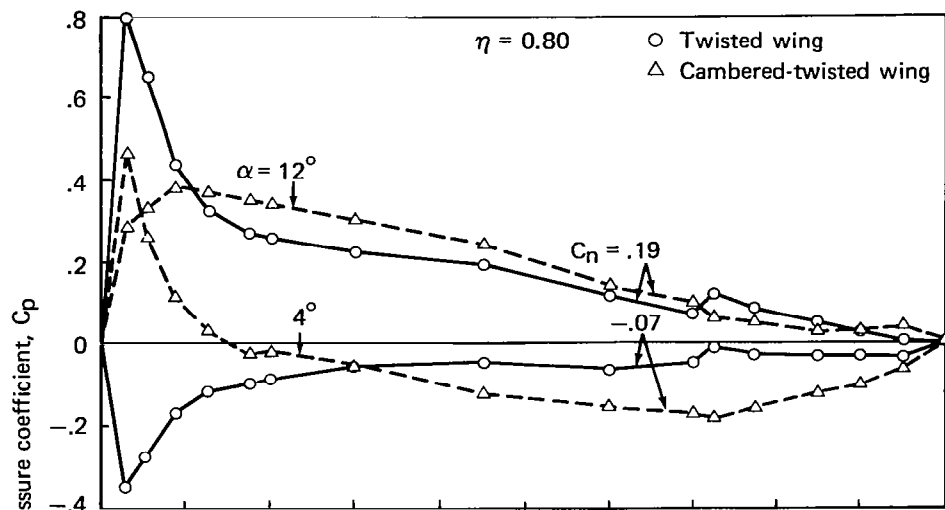
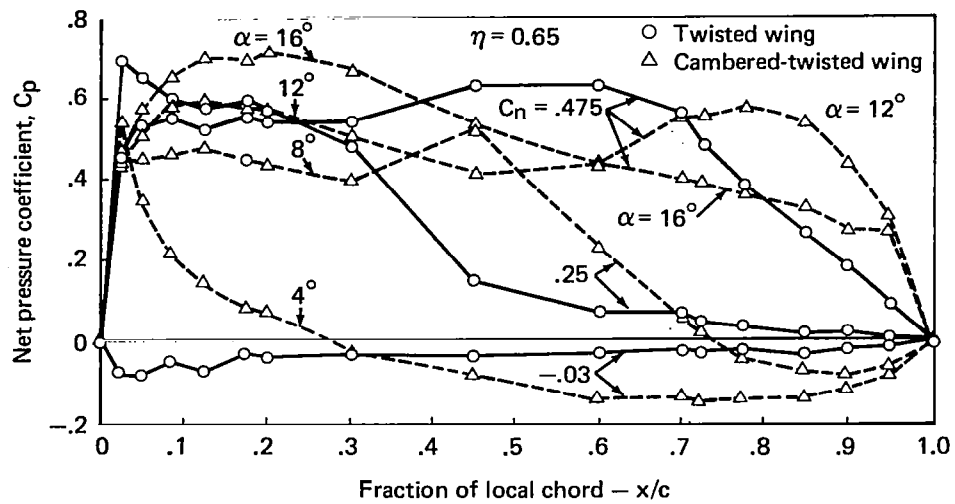


Figure 11.—(Continued)

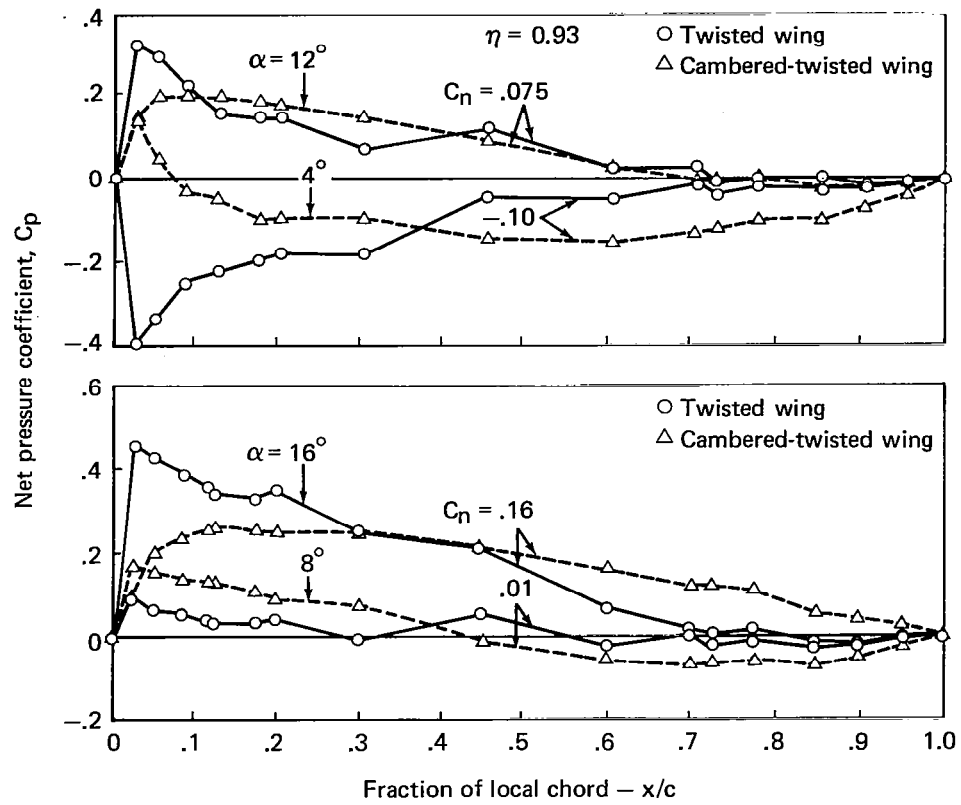


Figure 11.—(Concluded)

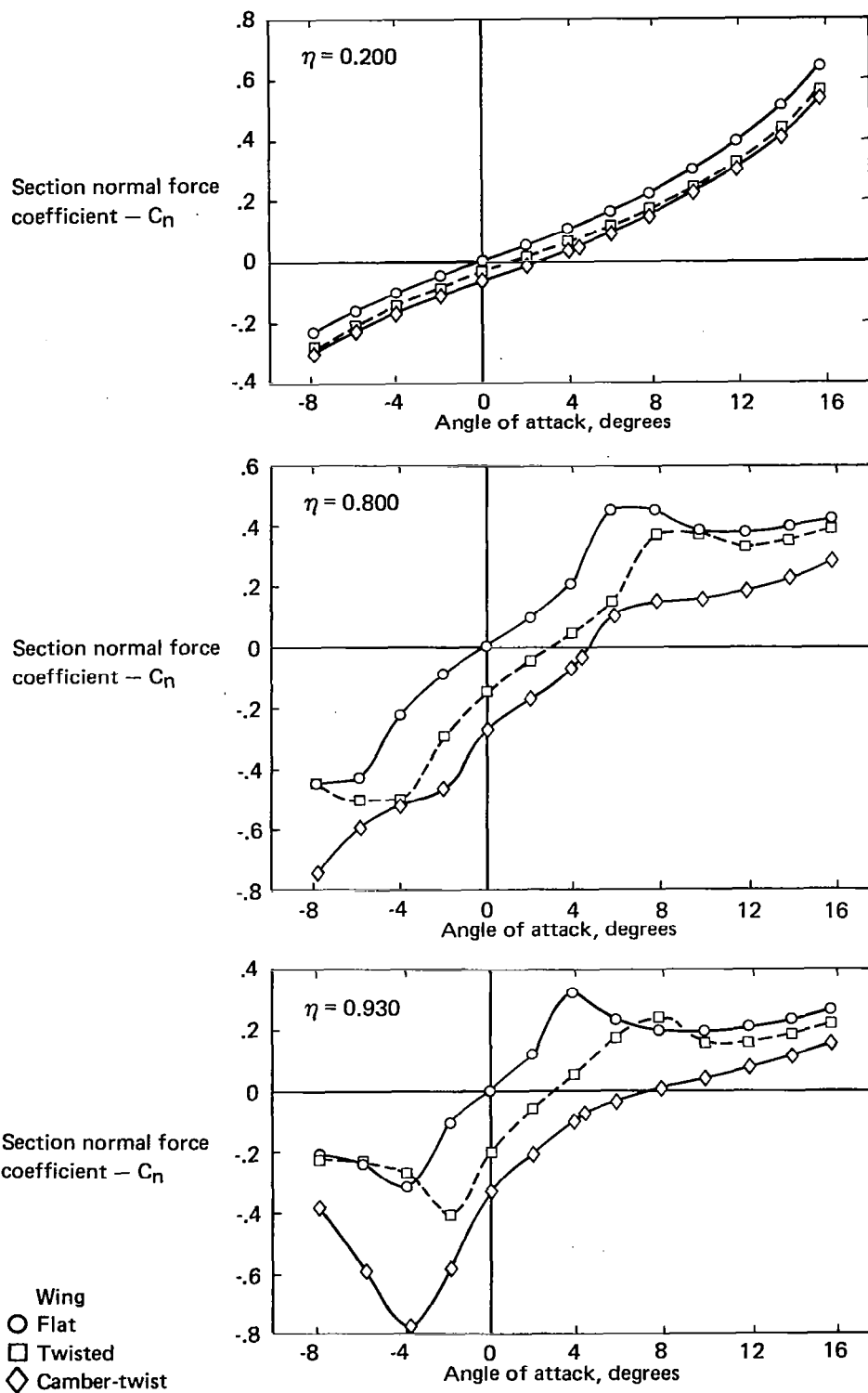


Figure 12.—Comparison of Experimental Section Normal Force Coefficients for Three Wing Shapes, $M = 0.85$

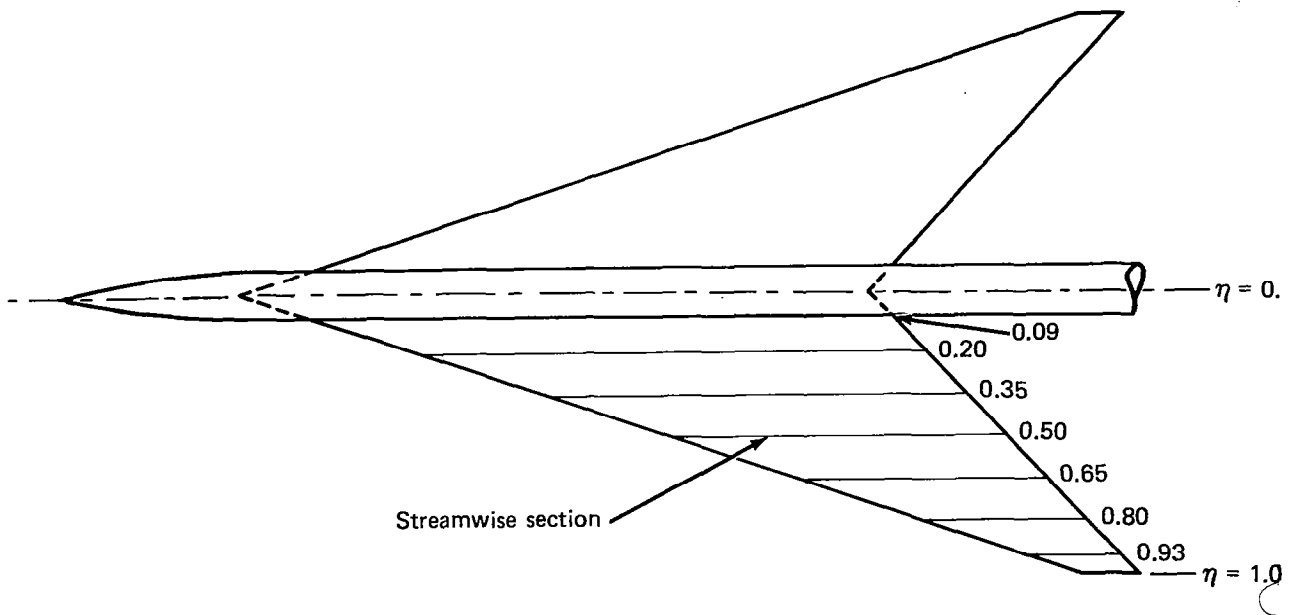


Figure 13.—Definition of Streamwise Wing Sections

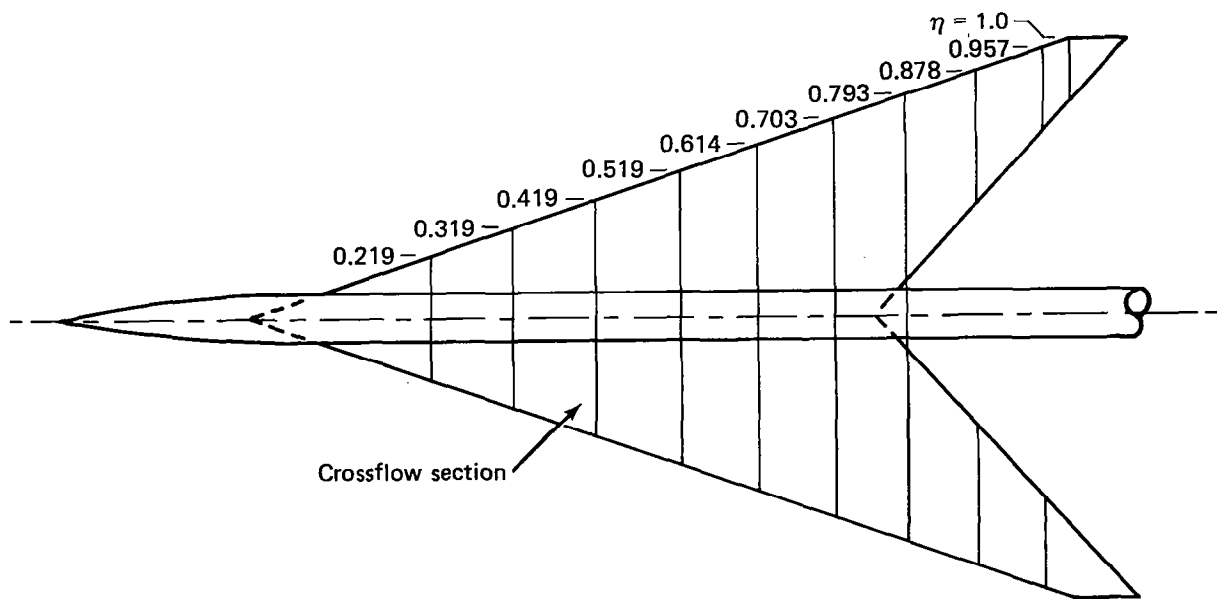


Figure 14.—Definition of Crossflow Wing Sections

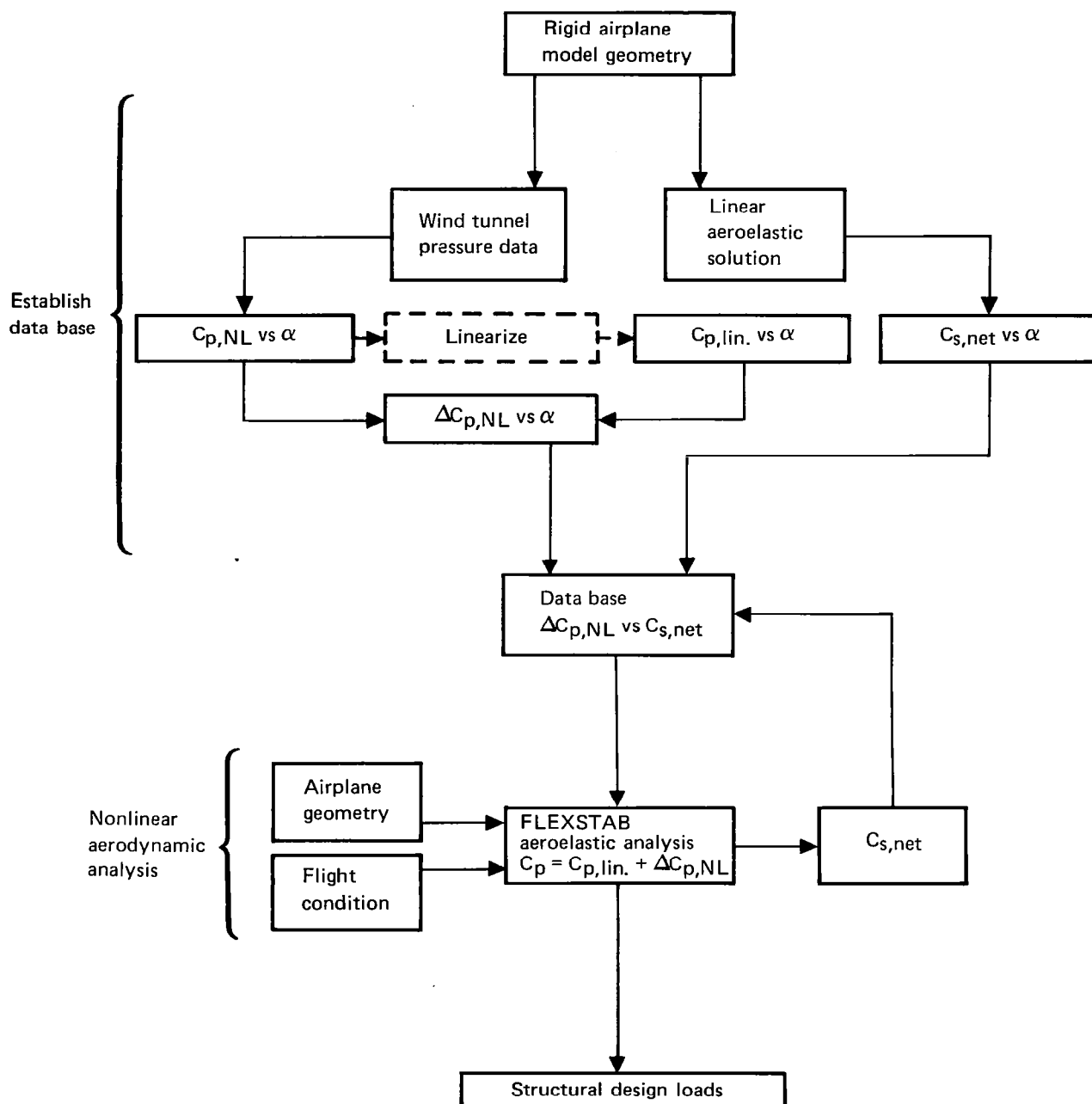


Figure 15.—Proposed Iterative Aeroelastic Loads Prediction Method Based on Net Leading-Edge Suction Coefficient

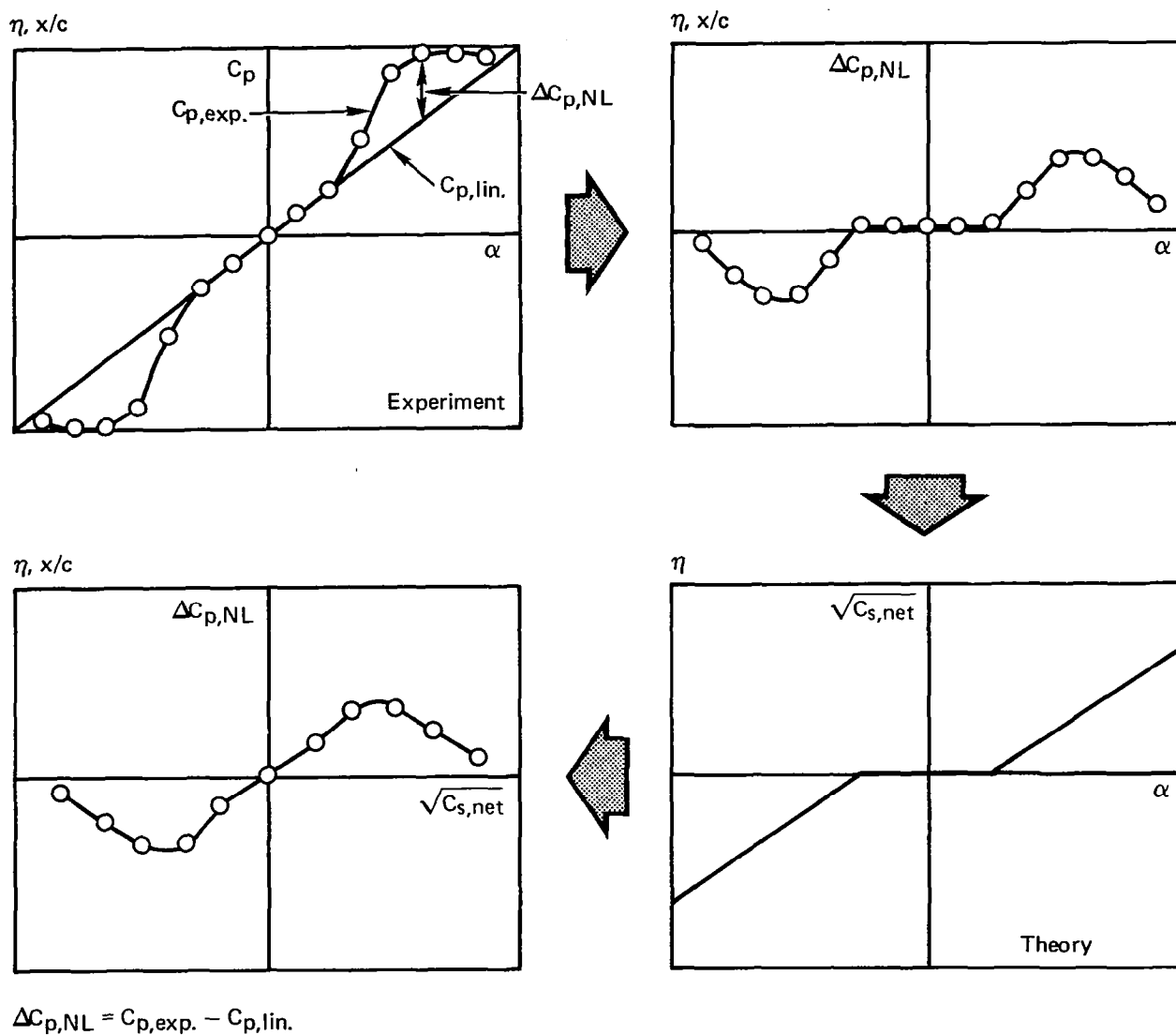


Figure 16.—Procedure to Establish a Data Base Which Relates Nonlinear Pressure Coefficients to Net Leading-Edge Suction Coefficient

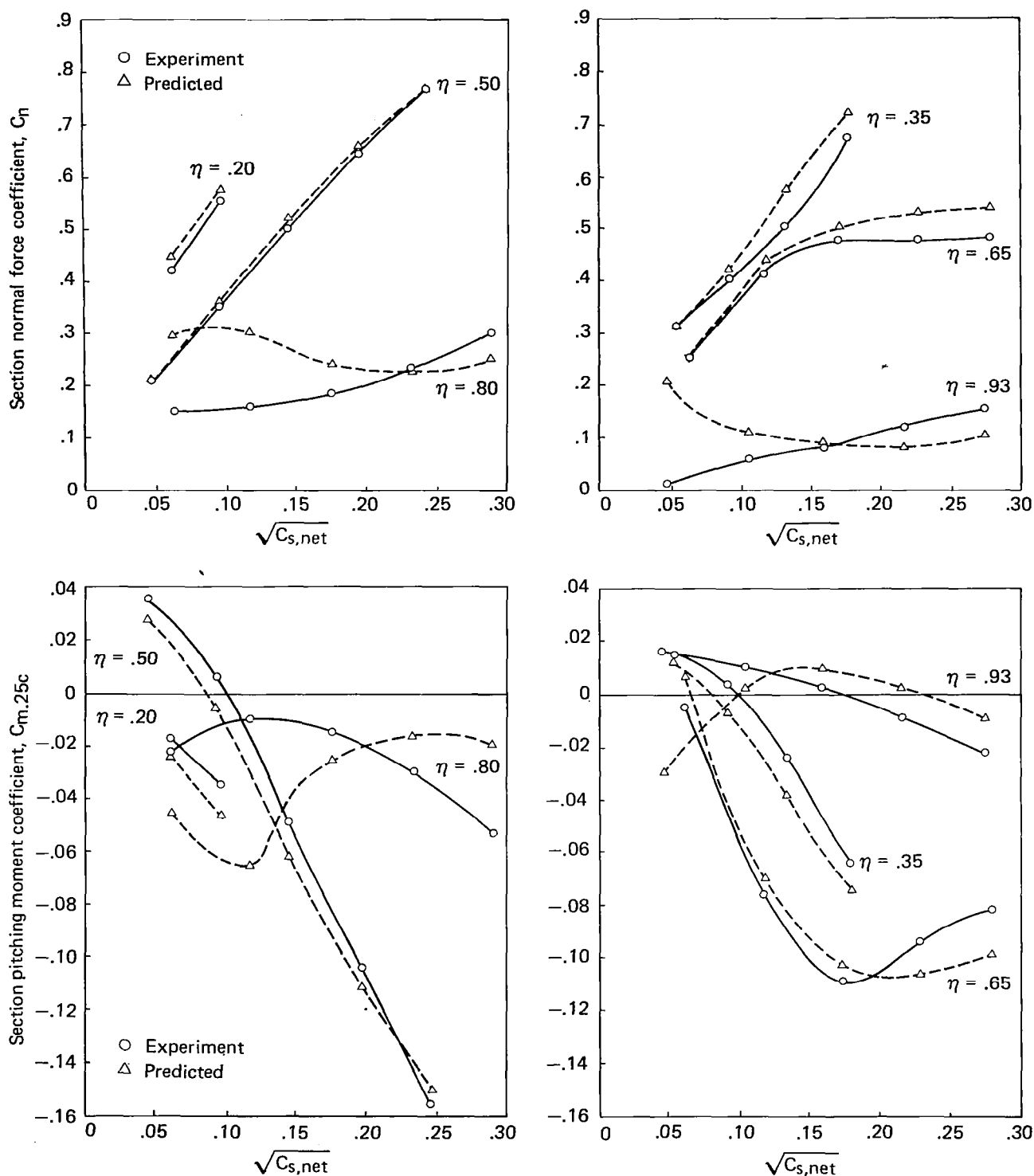


Figure 17.—Prediction of Streamwise Section Coefficients for the Cambered-Twisted Wing Using the Data Base for the Flat Wing Data Related to the Net Leading-Edge Suction Coefficient, $M = 0.85$

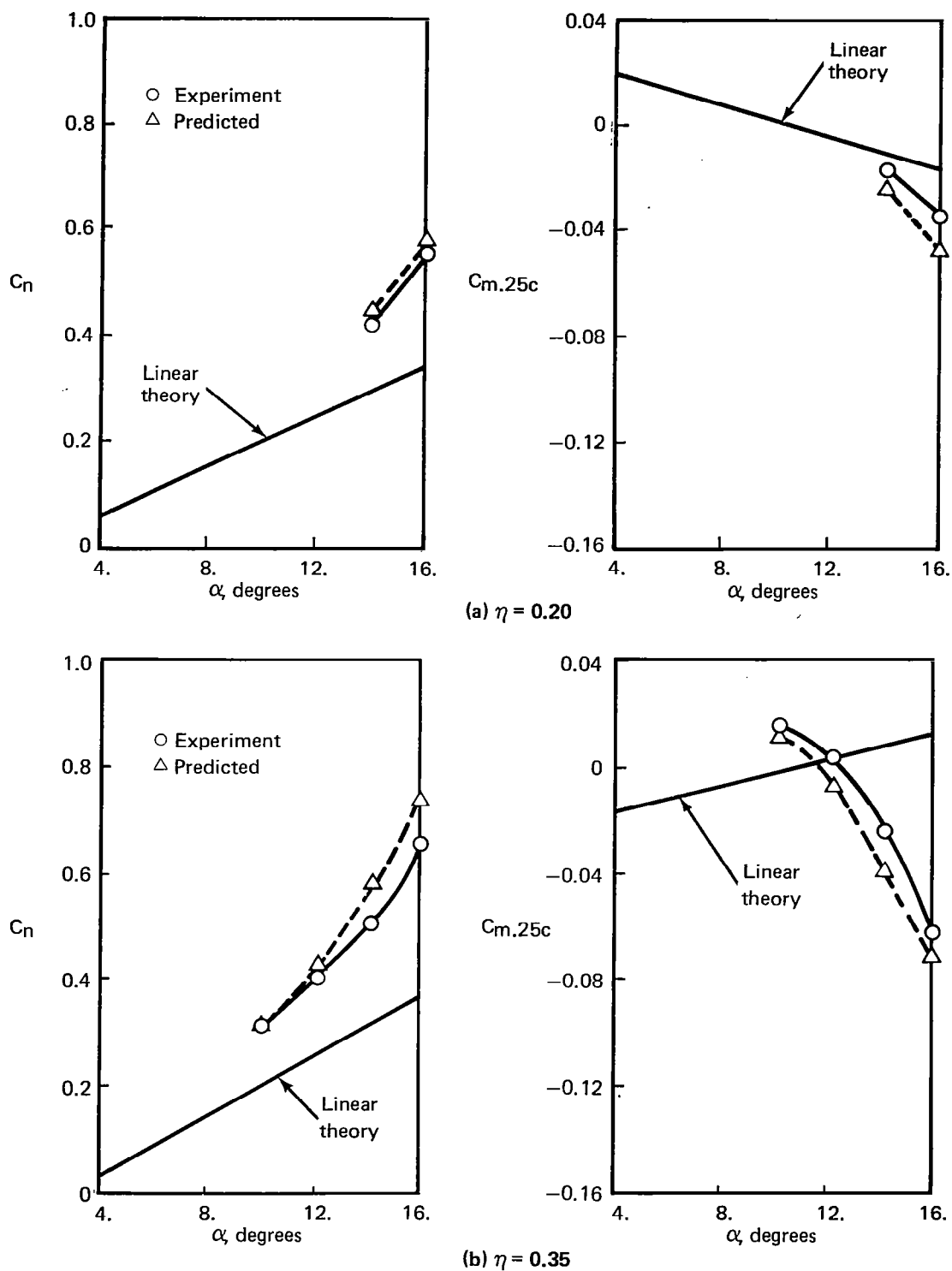
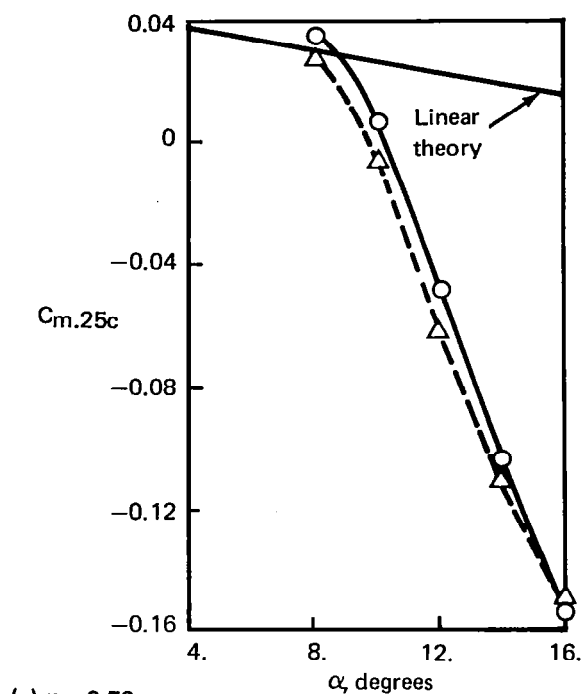
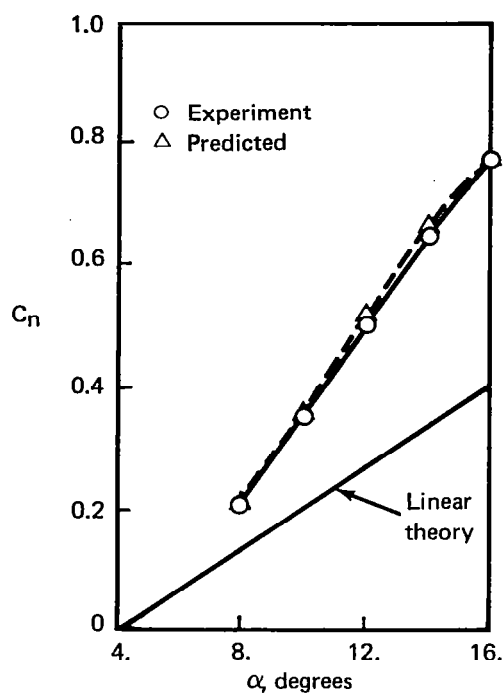
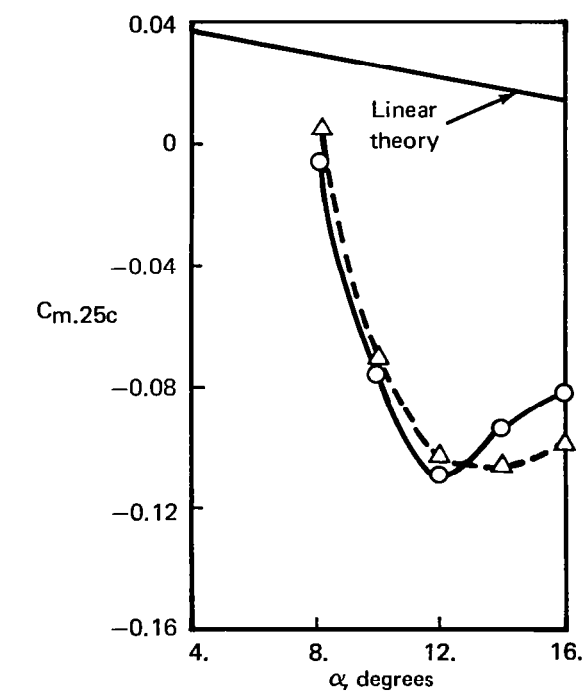
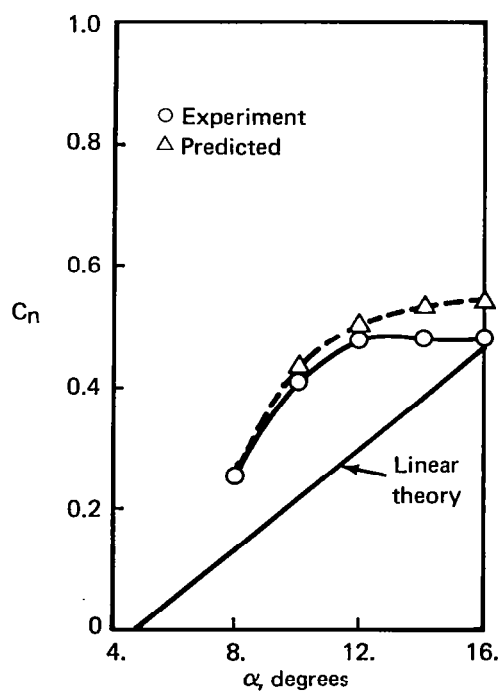


Figure 18.—Prediction of Streamwise Section Coefficients for the Cambered-Twisted Wing Using the Data Base for the Flat Wing Data Related to the Net Leading-Edge Suction Coefficient, Compared to Linear Theory, $M = 0.85$

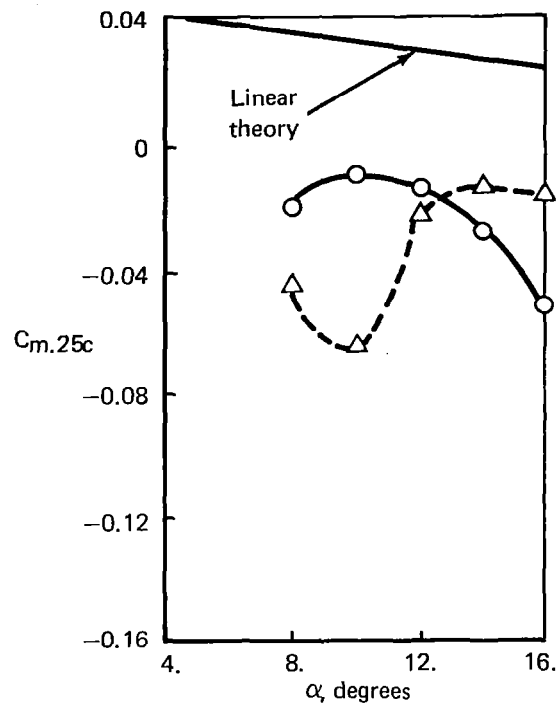
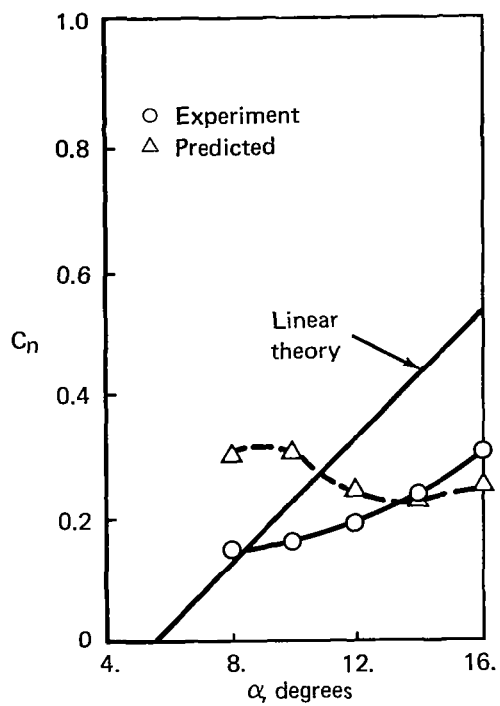


(c) $\eta = 0.50$

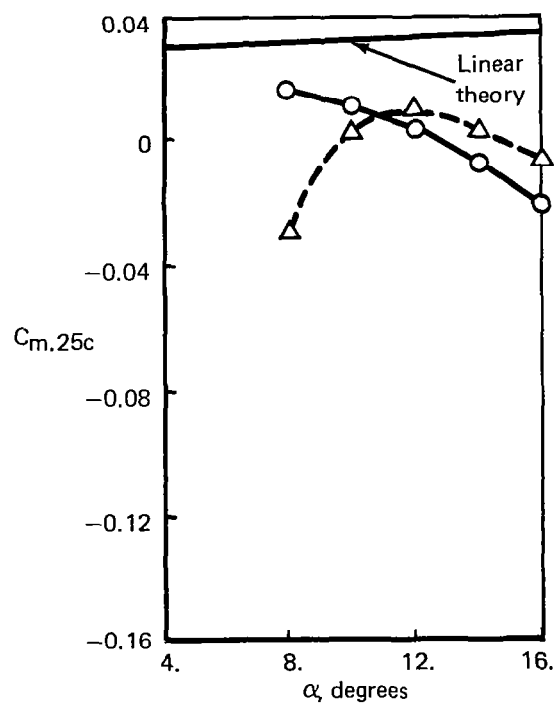
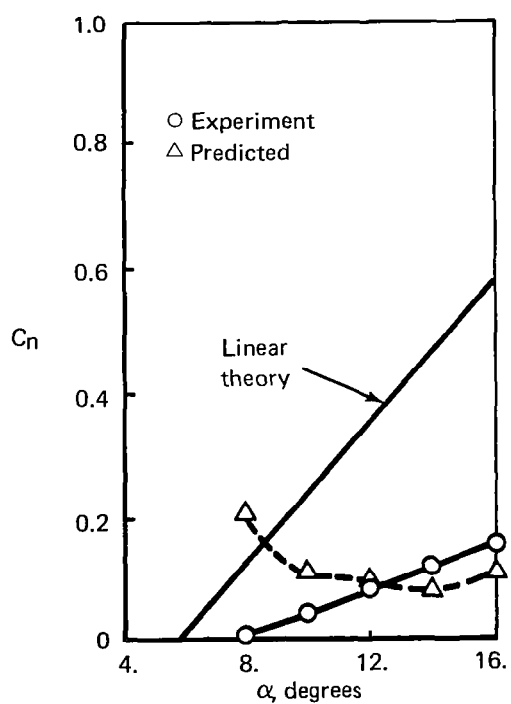


(d) $\eta = 0.65$

Figure 18.—(Continued)



(e) $\eta = 0.80$



(f) $\eta = 0.93$

Figure 18.—(Concluded)

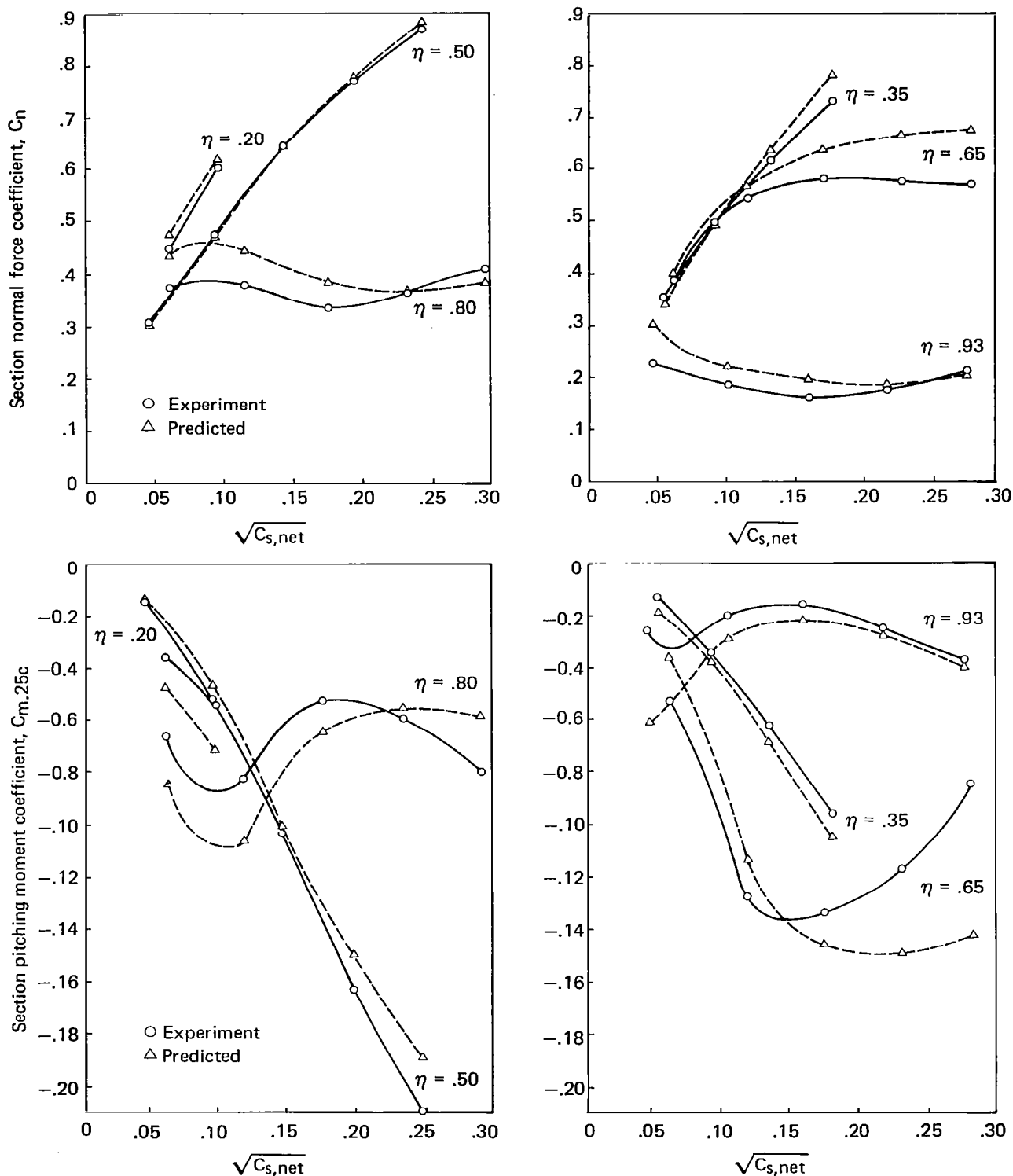


Figure 19.—Prediction of Streamwise Section Coefficients for the Twisted Wing Using the Data Base for the Flat Wing Data Related to the Net Leading-Edge Suction Coefficient, $M = 0.85$

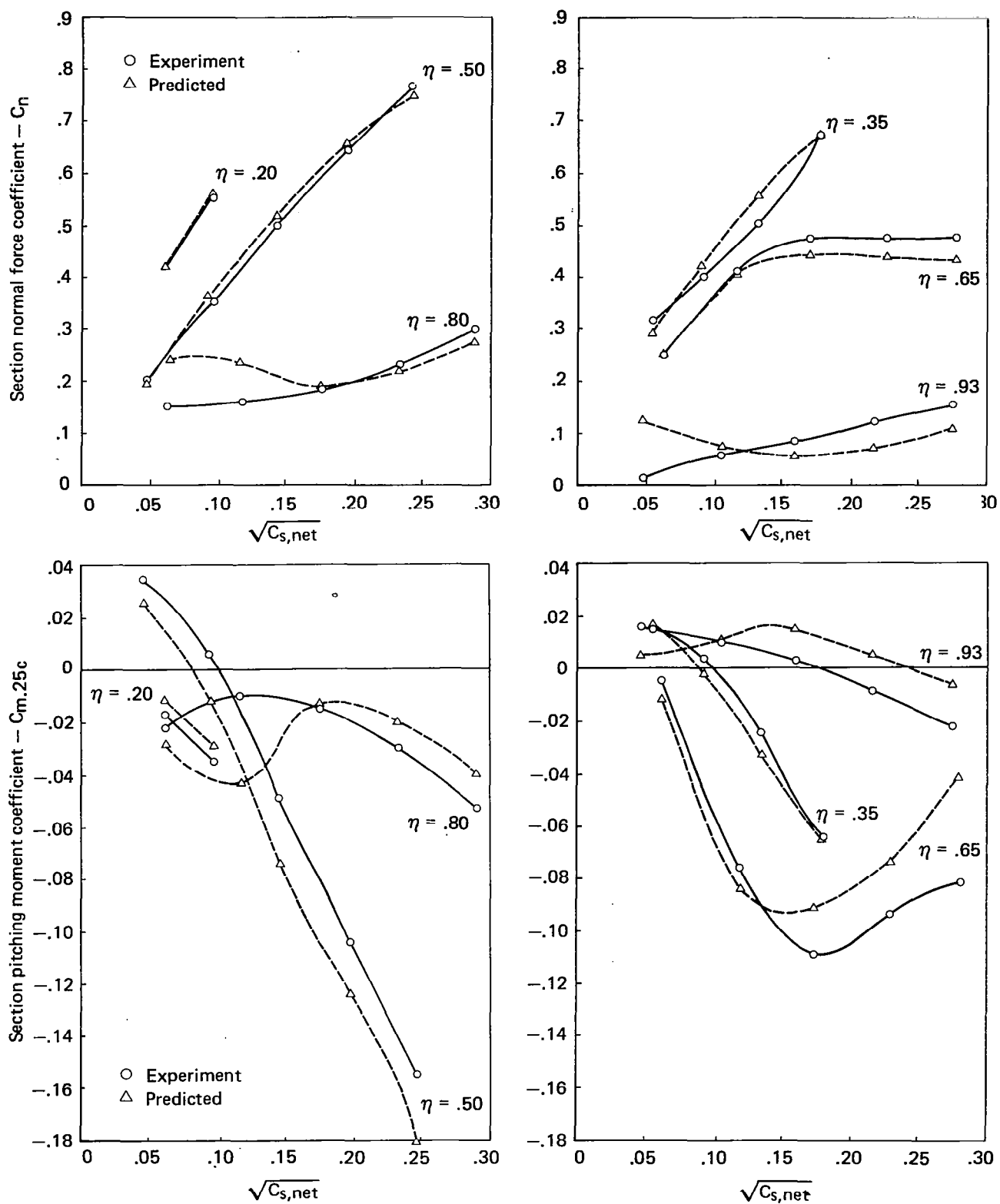
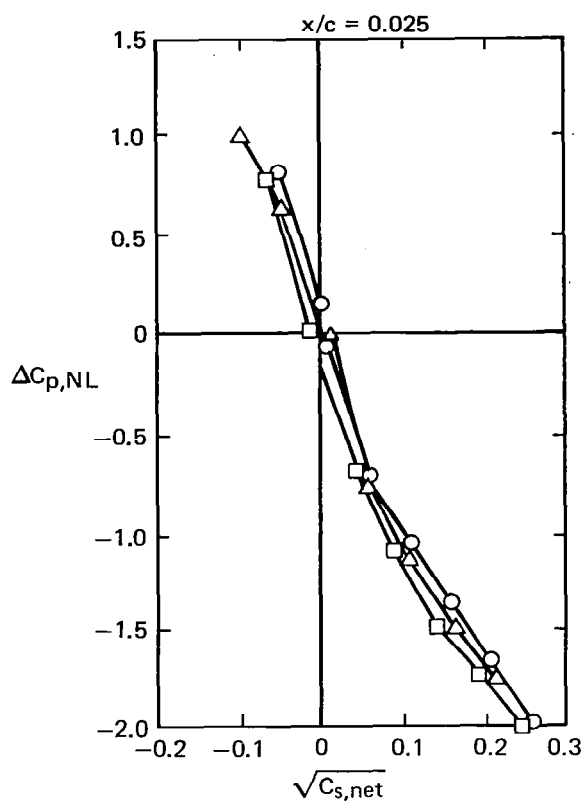


Figure 20.—Prediction of Streamwise Section Coefficients for the Cambered-Twisted Wing Using the Data Base for the Twisted Wing Data Related to the Net Leading-Edge Suction Coefficient, $M = 0.85$



○ Flat wing
 △ Twisted wing
 □ Cambered-twisted wing

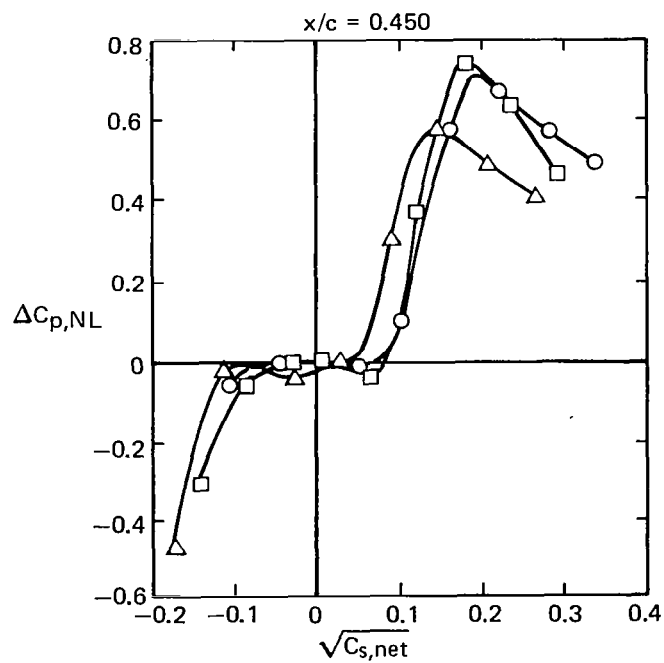
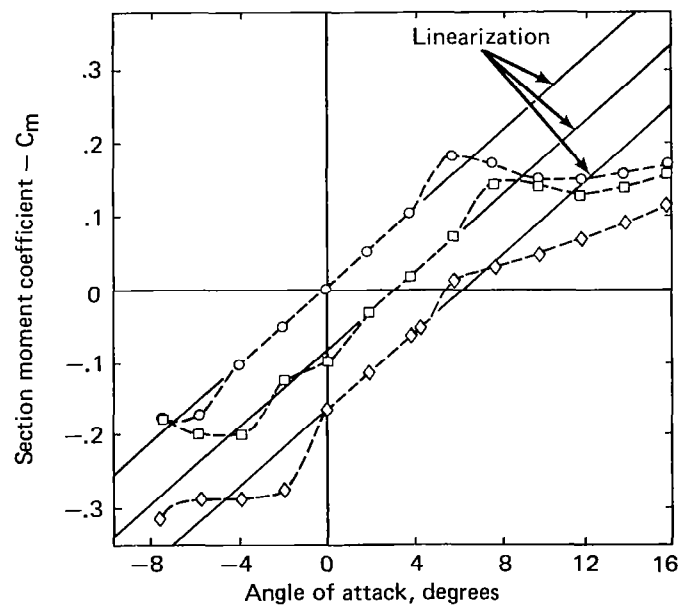
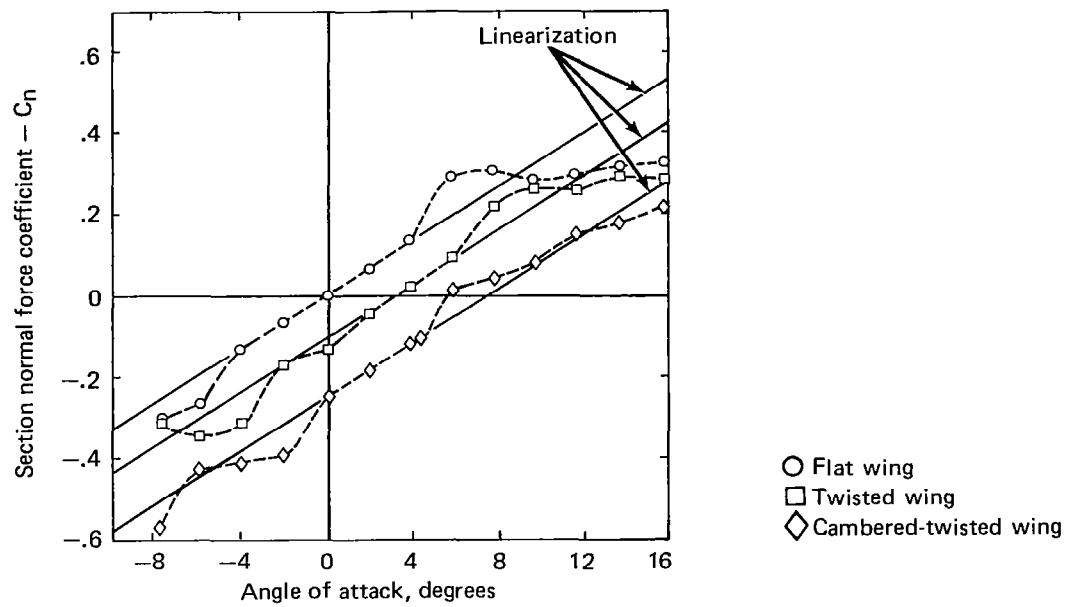
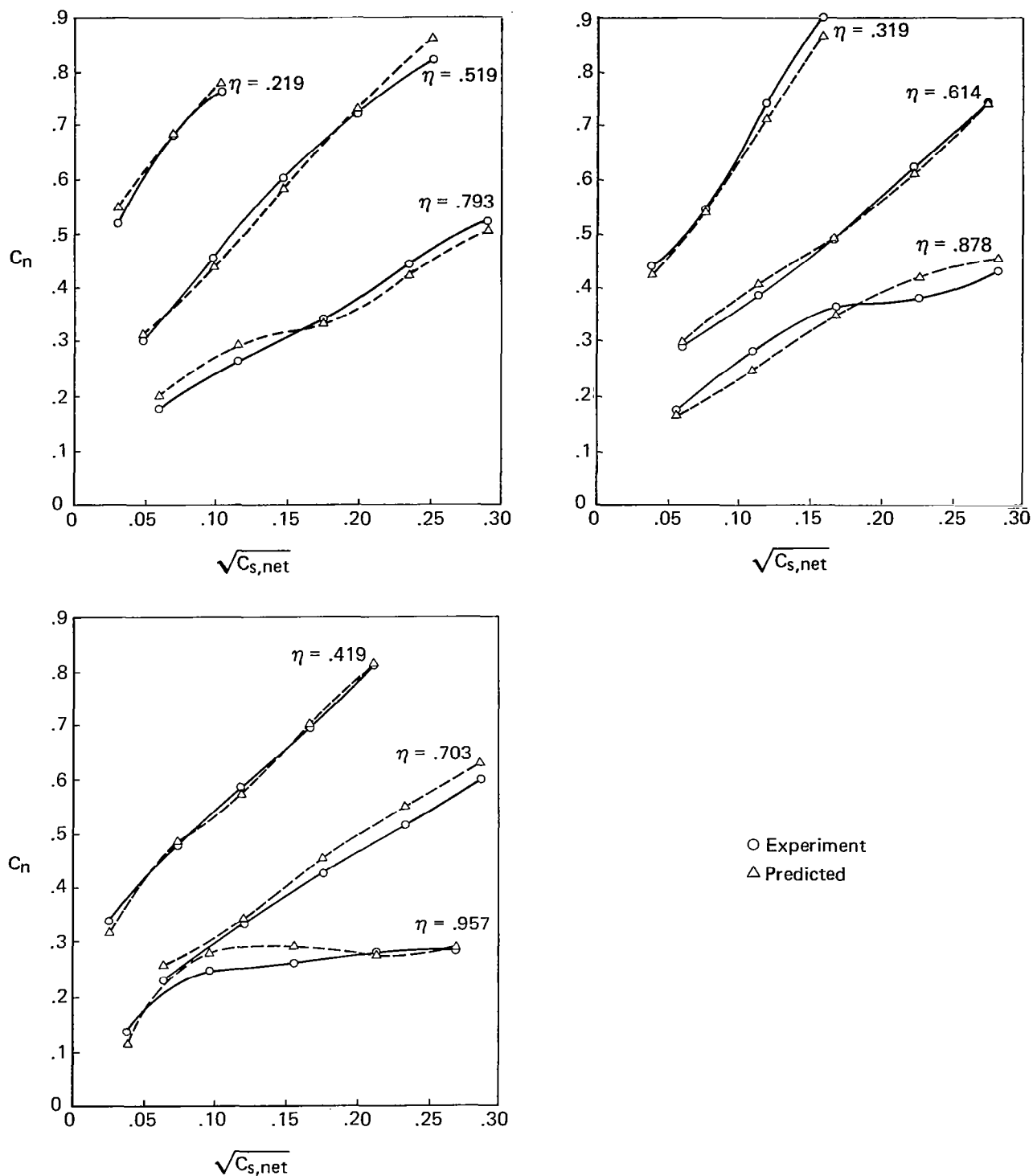


Figure 21.—Incremental Nonlinear Net Pressure Coefficients as a Function of the Net Leading-Edge Suction Coefficient for the Three Wings, $\eta = 0.50$, $M = 0.85$



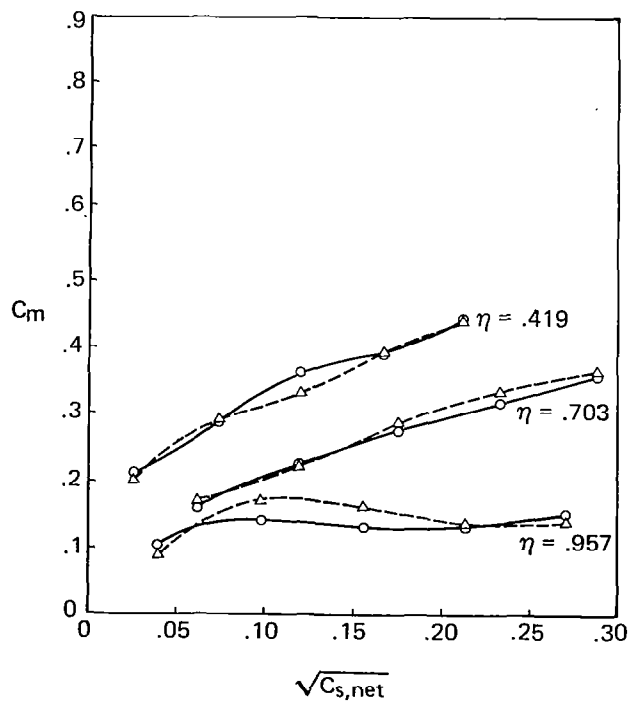
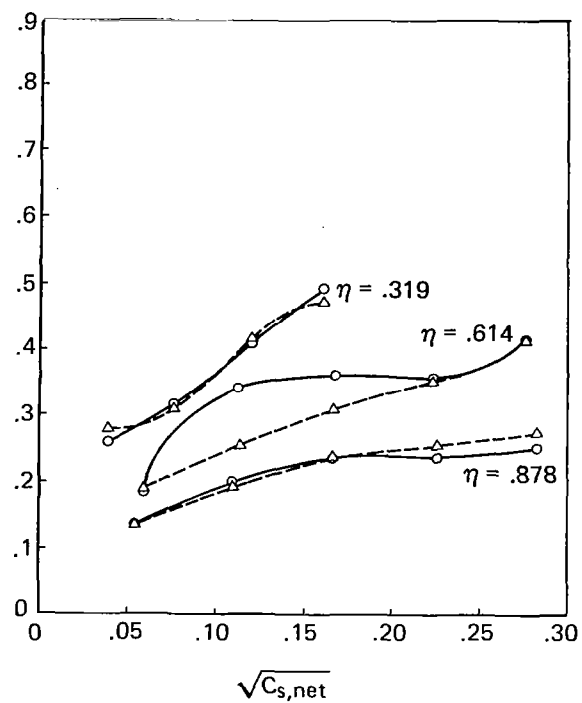
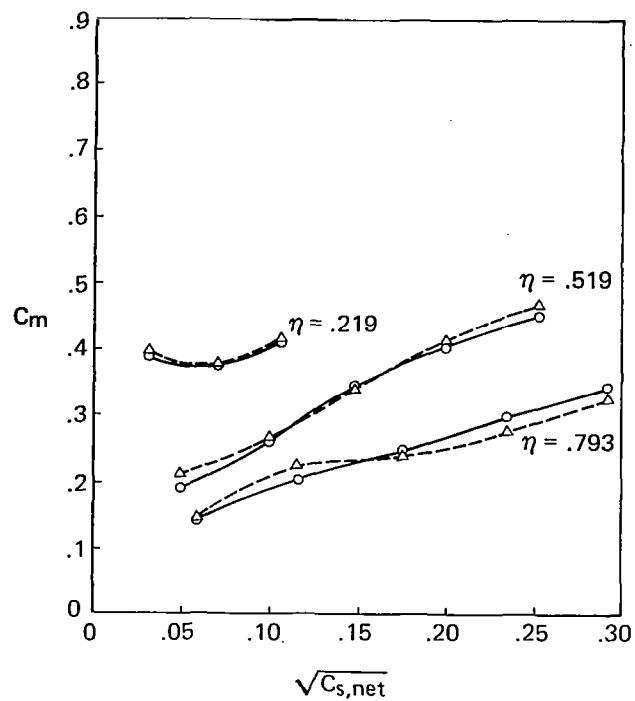
Note:
Constant body station (crossflow) section;
intersects leading-edge at $\eta = 0.957$

Figure 22.—Typical Variation of Crossflow Section Coefficients with Angle of Attack for the Three Wings, $M = 0.85$



(a) Section Normal Force Coefficient

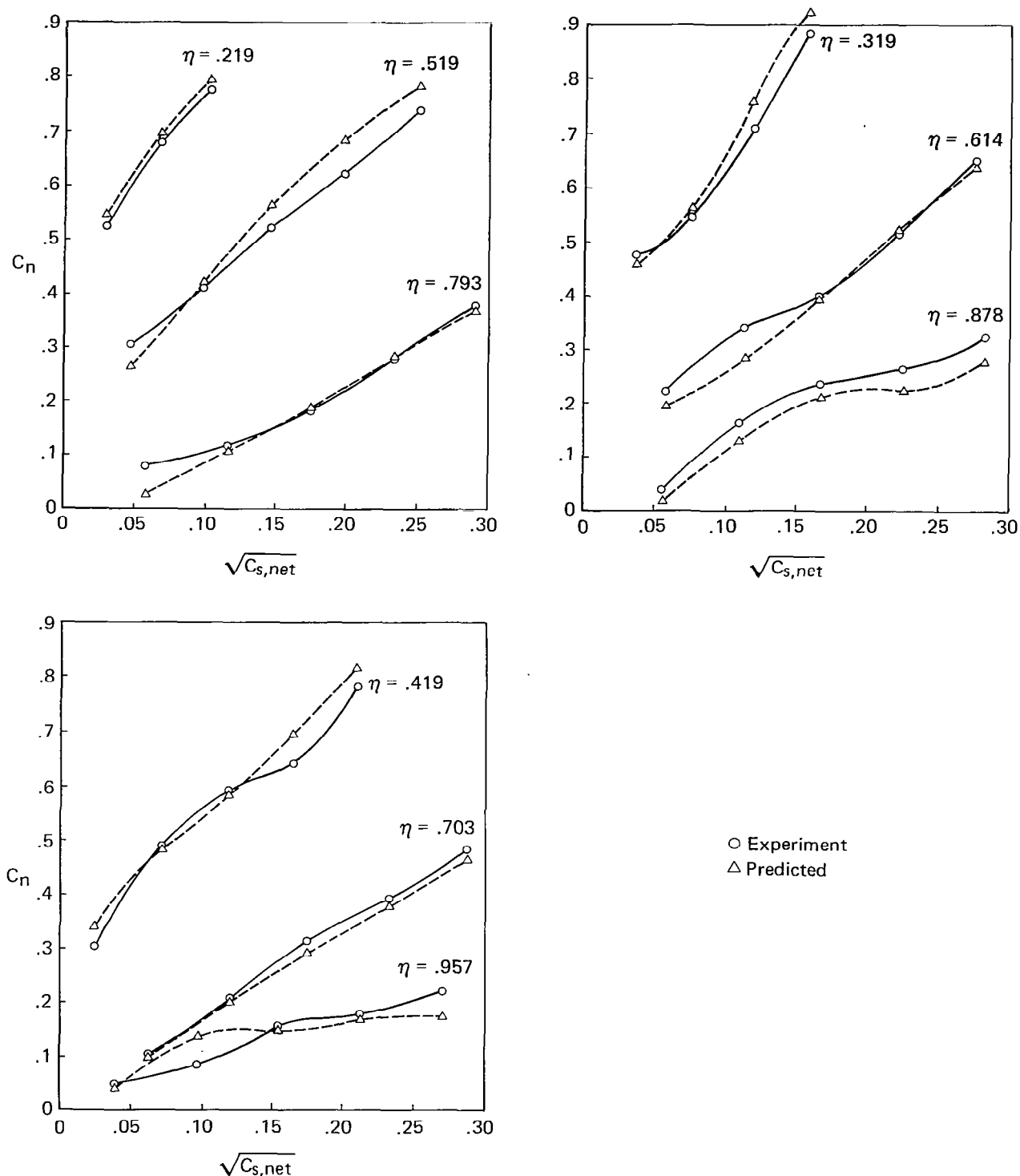
Figure 23.—Prediction of Crossflow Section Coefficients for the Twisted Wing Using the Data Base for the Flat Wing Data Related to the Net Leading-Edge Suction Coefficient, $M = 0.85$



○ Experiment
△ Predicted

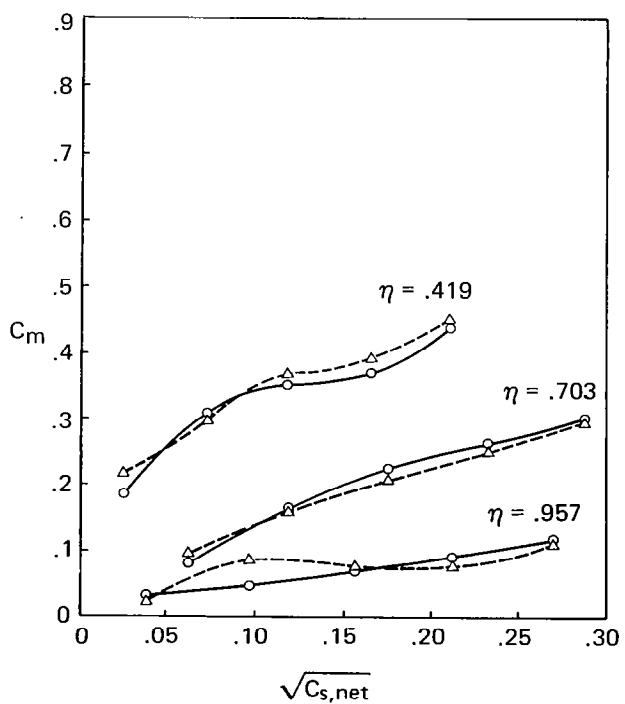
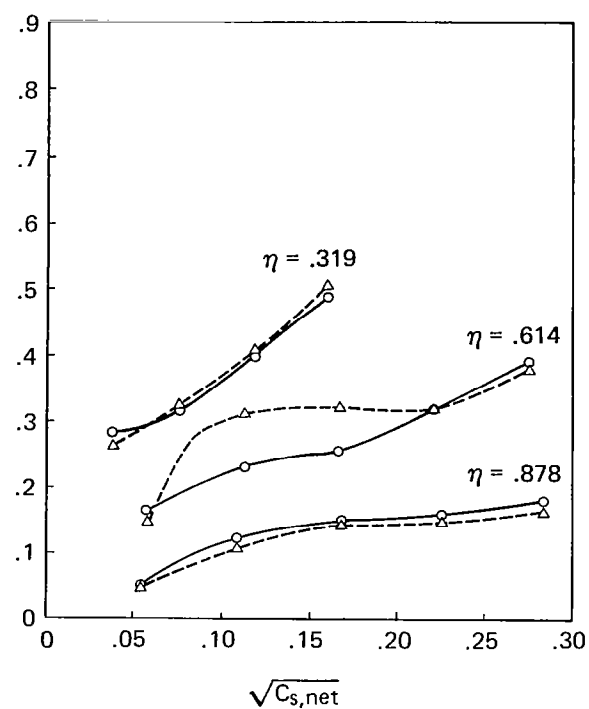
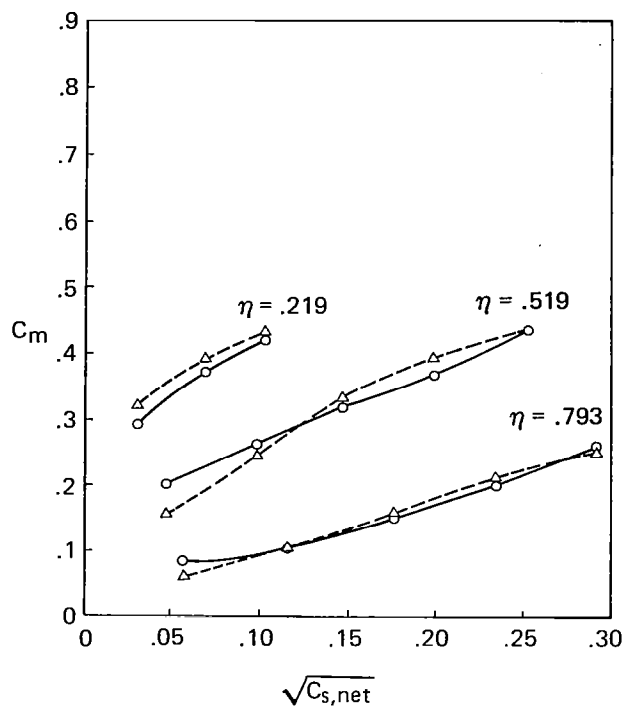
(b) Section Moment Coefficient at Side of Body

Figure 23.—(Concluded)



(a) Section Normal Force Coefficient

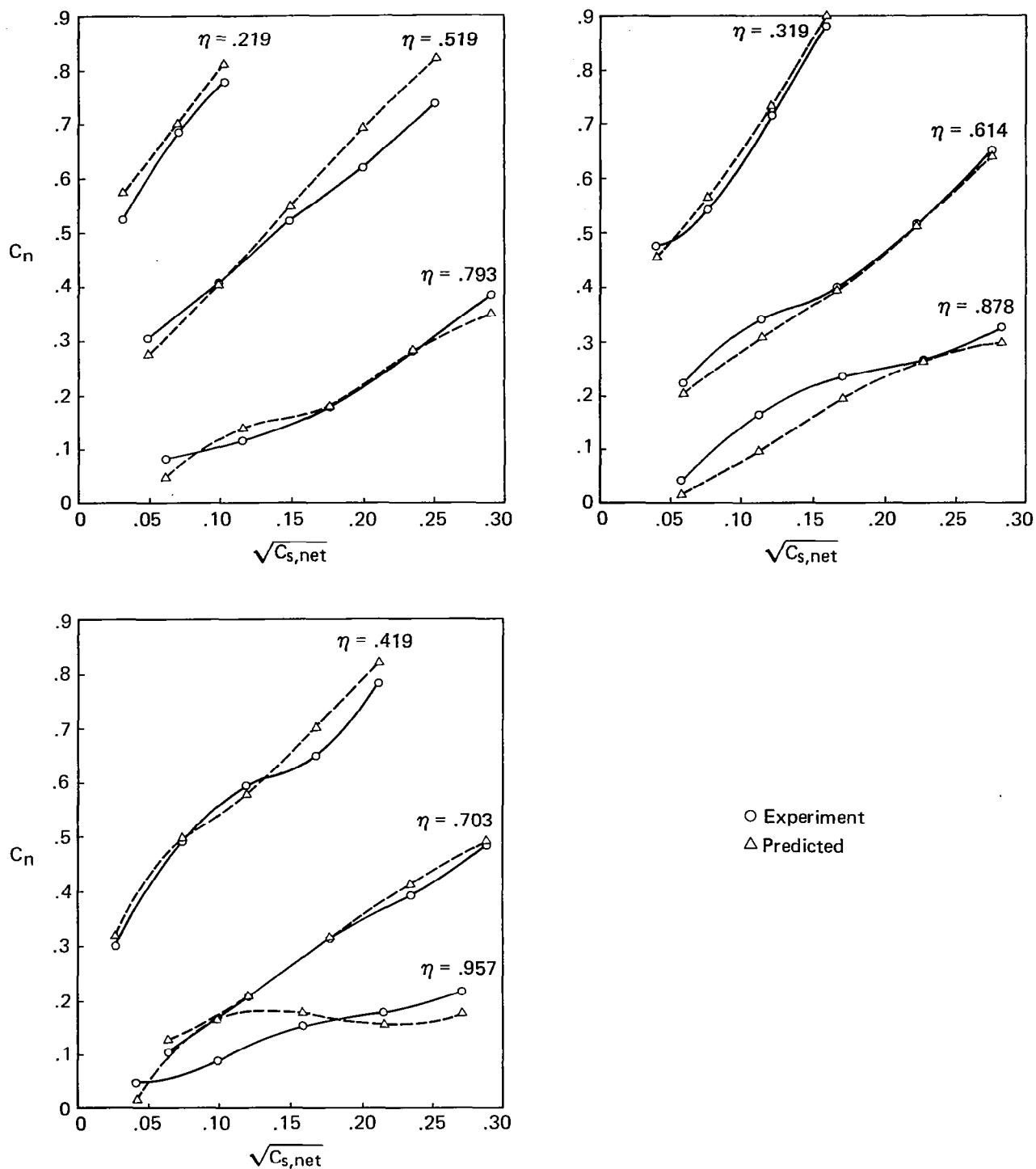
Figure 24.—Prediction of Crossflow Section Coefficients for the Cambered-Twisted Wing Using the Data Base for the Twisted Wing Data Related to the Net Leading-Edge Suction Coefficient, $M = 0.85$



○ Experiment
△ Predicted

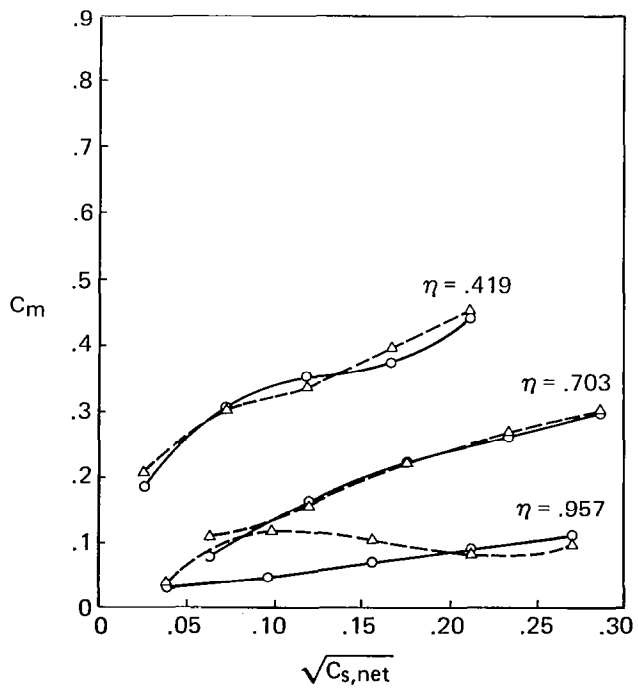
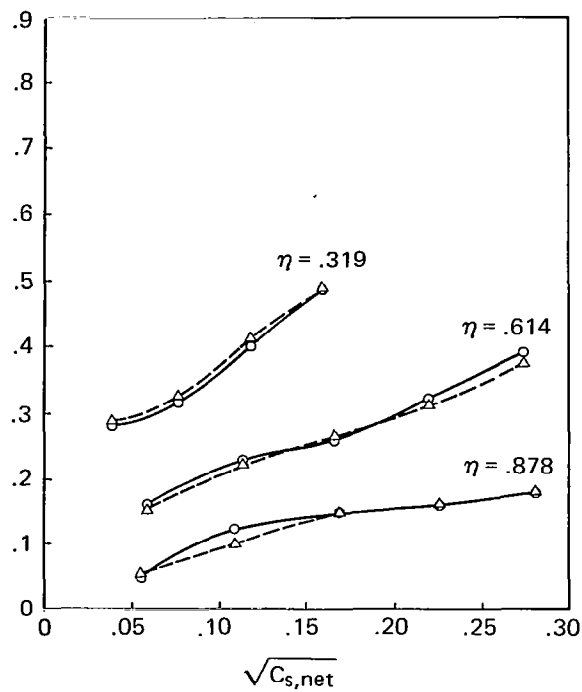
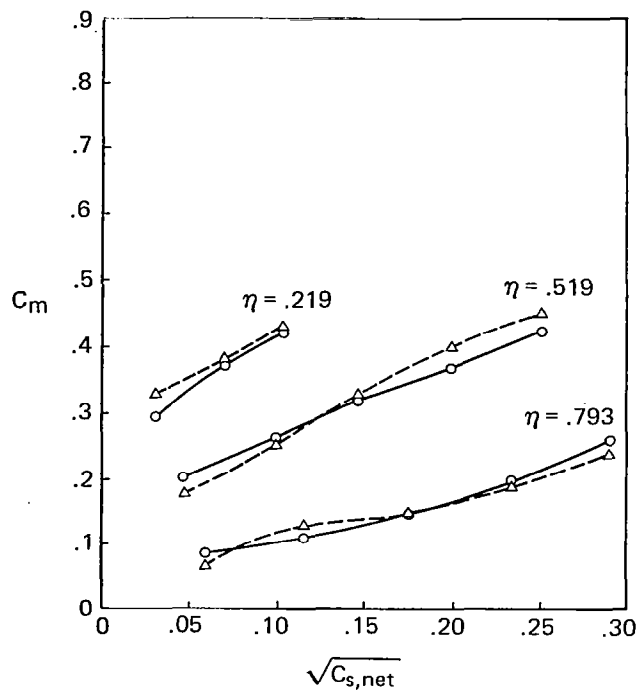
(b) Section Moment Coefficient at Side of Body

Figure 24.—(Concluded)



(a) Section Normal Force Coefficient

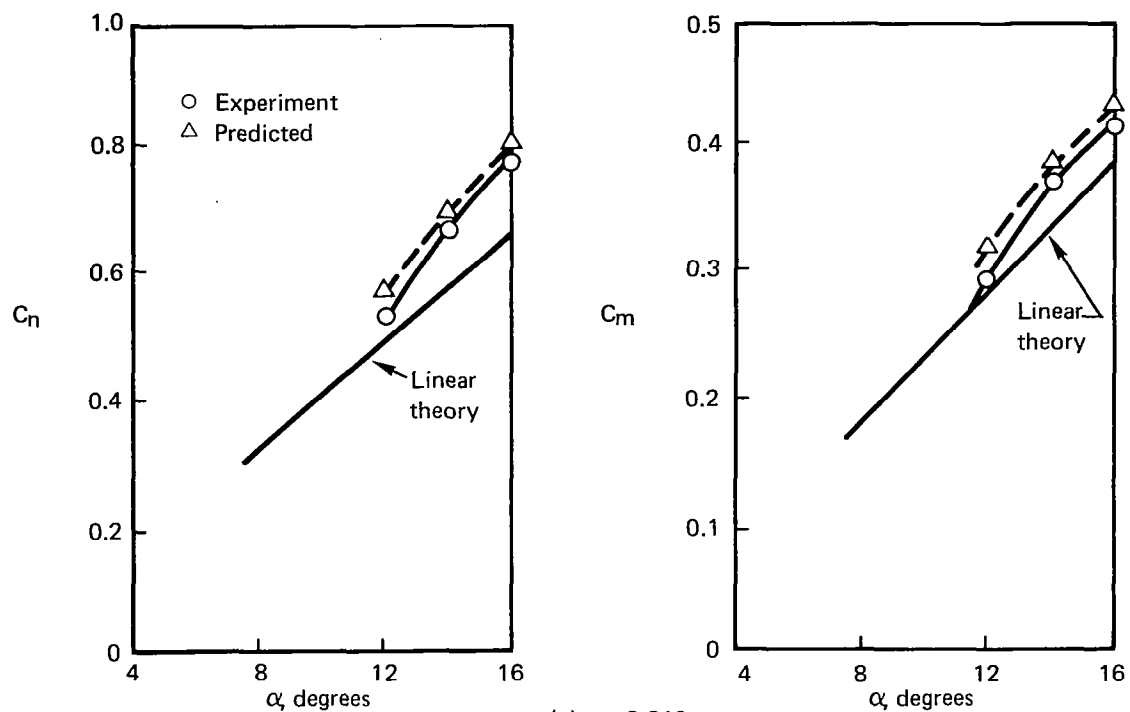
Figure 25.—Prediction of Crossflow Section Coefficients for the Cambered-Twisted Wing Using the Data Base for the Flat Wing Data Related to the Net Leading-Edge Suction Coefficient, $M = 0.85$



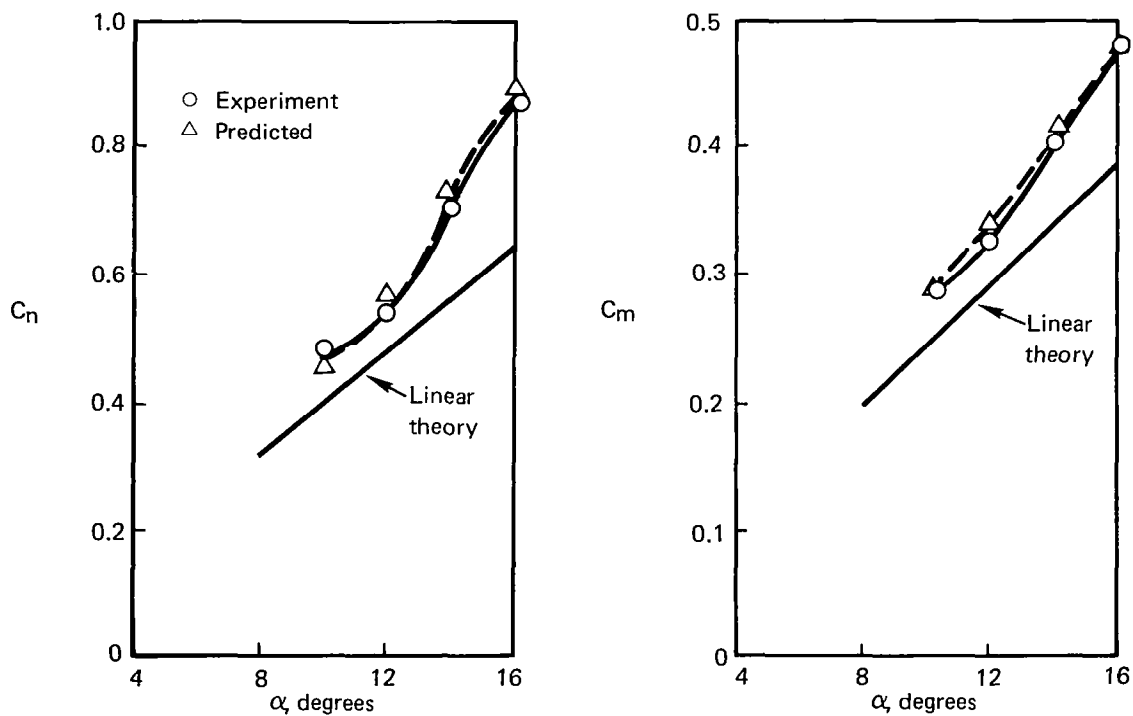
○ Experiment
△ Predicted

(b) Section Moment Coefficient at Side of Body

Figure 25.—(Concluded)

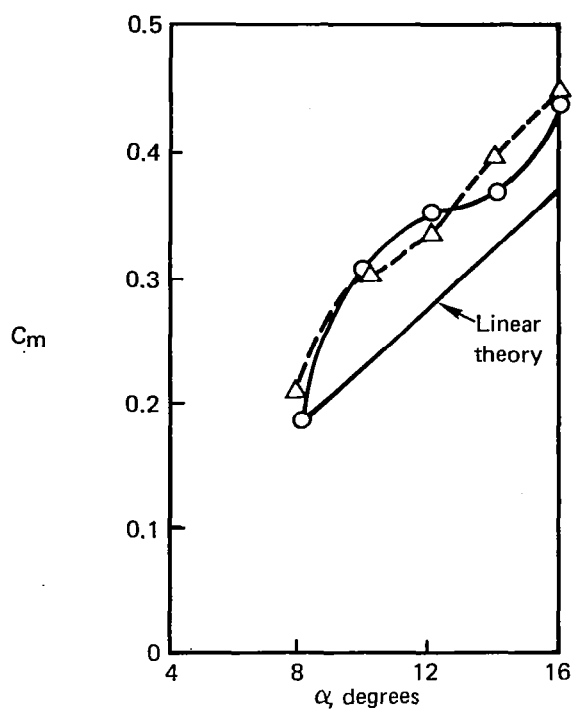
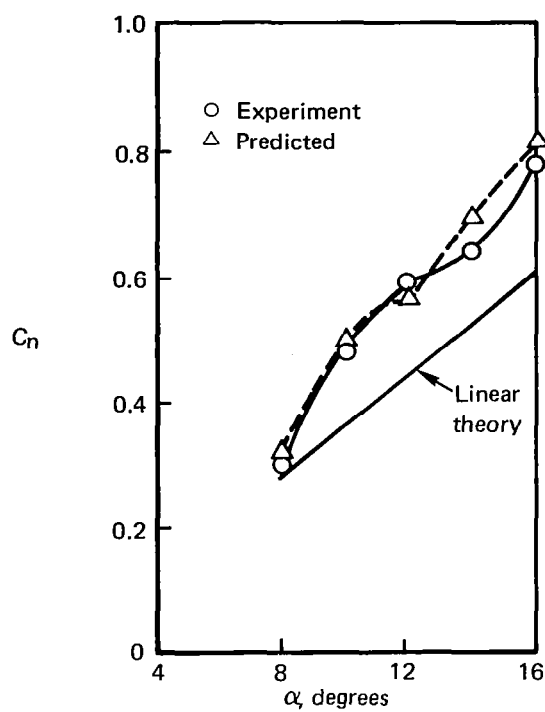


(a) $\eta = 0.219$

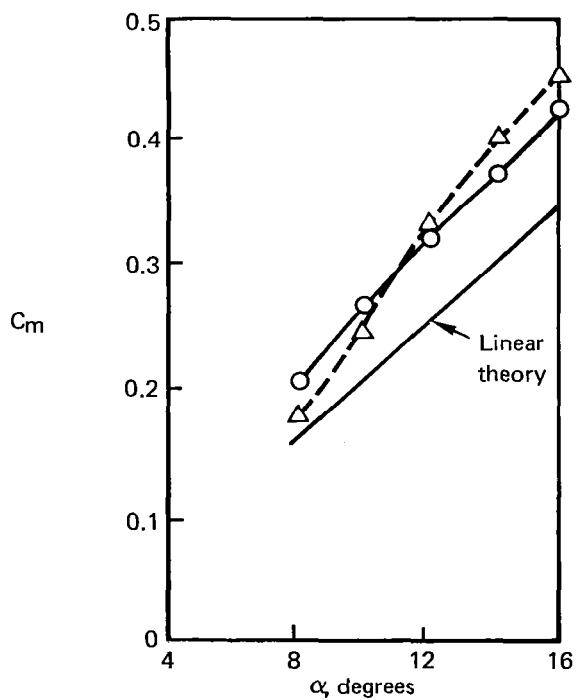
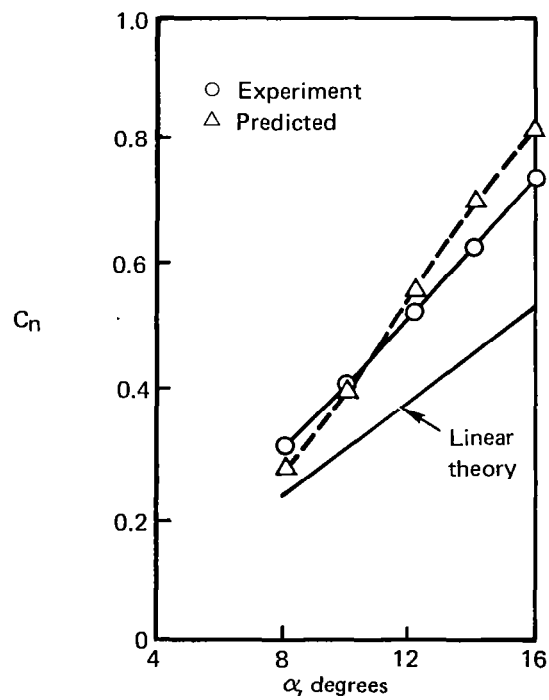


(b) $\eta = 0.319$

Figure 26.—Prediction of Crossflow Section Coefficients for the Cambered-Twisted Wing Using the Data Base for the Flat Wing Data Related to the Net Leading-Edge Suction Coefficient, Compared to Linear Theory, $M = 0.85$

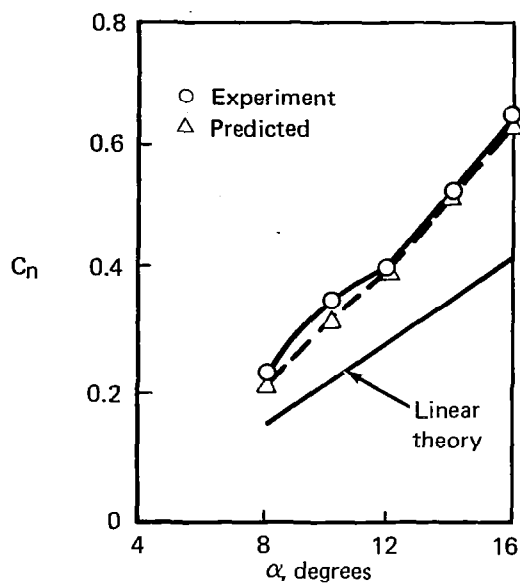


(c) $\eta = 0.419$

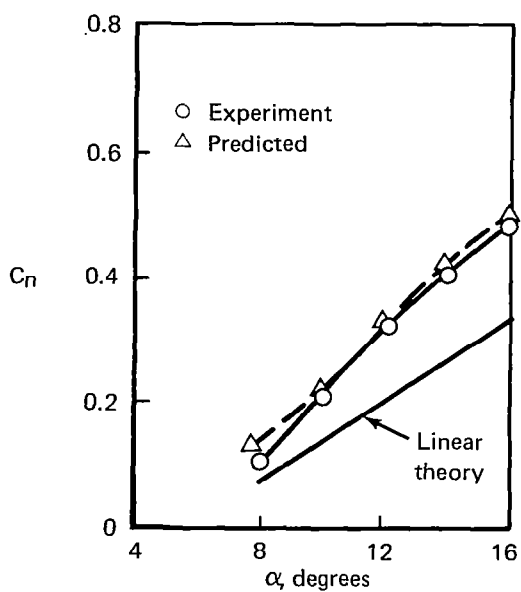
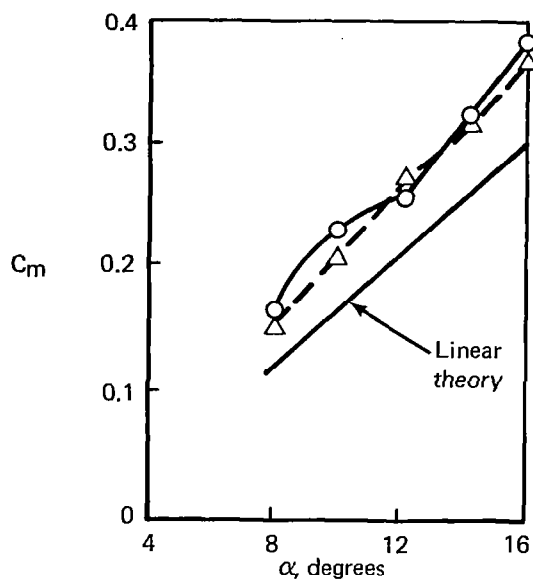


(d) $\eta = 0.519$

Figure 26.—(Continued)



(e) $\eta = 0.614$



(f) $\eta = 0.703$

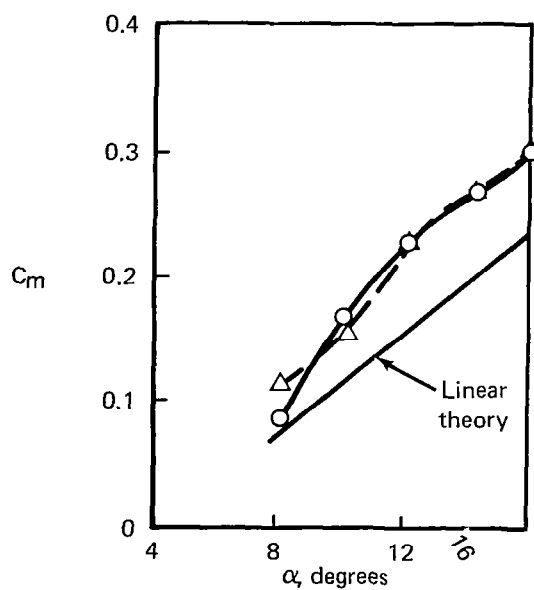
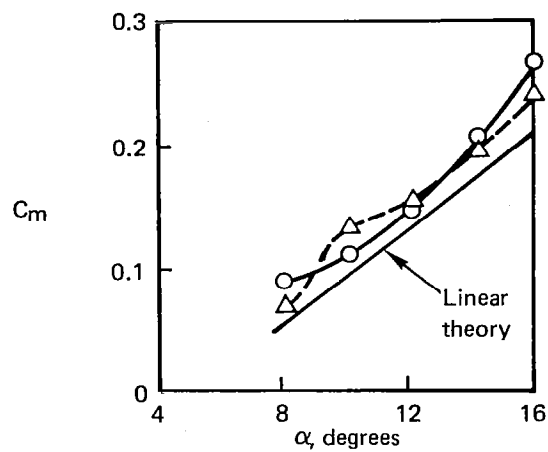
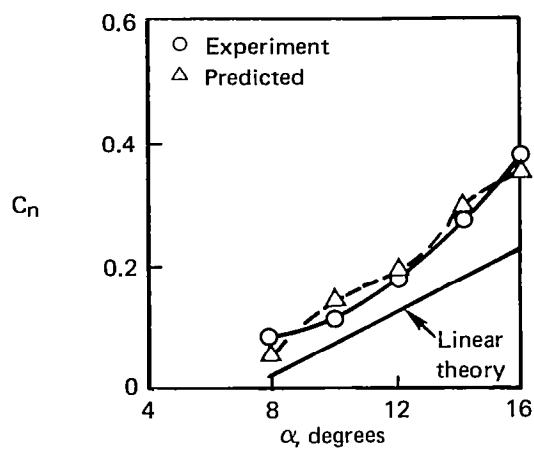
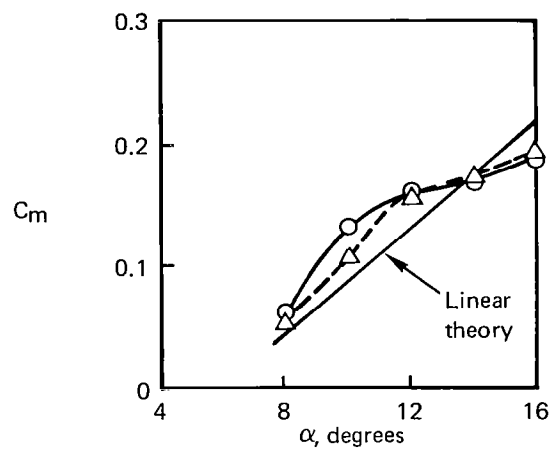
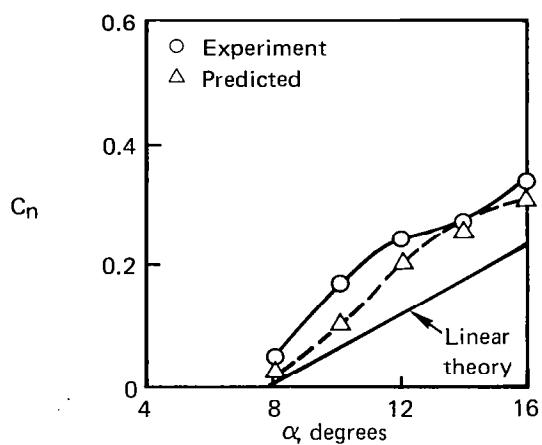


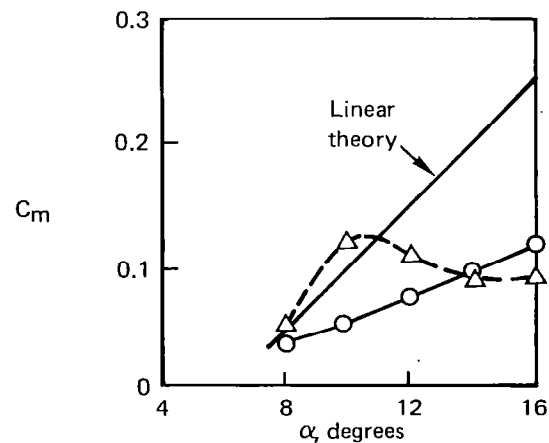
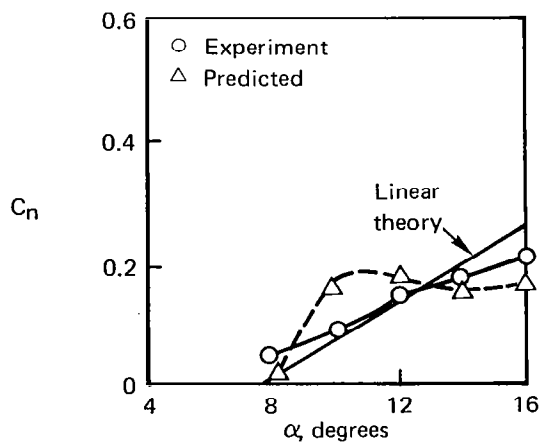
Figure 26.—(Continued)



(g) $\eta = 0.793$



(h) $\eta = 0.878$



(i) $\eta = 0.957$

Figure 26.—(Concluded)

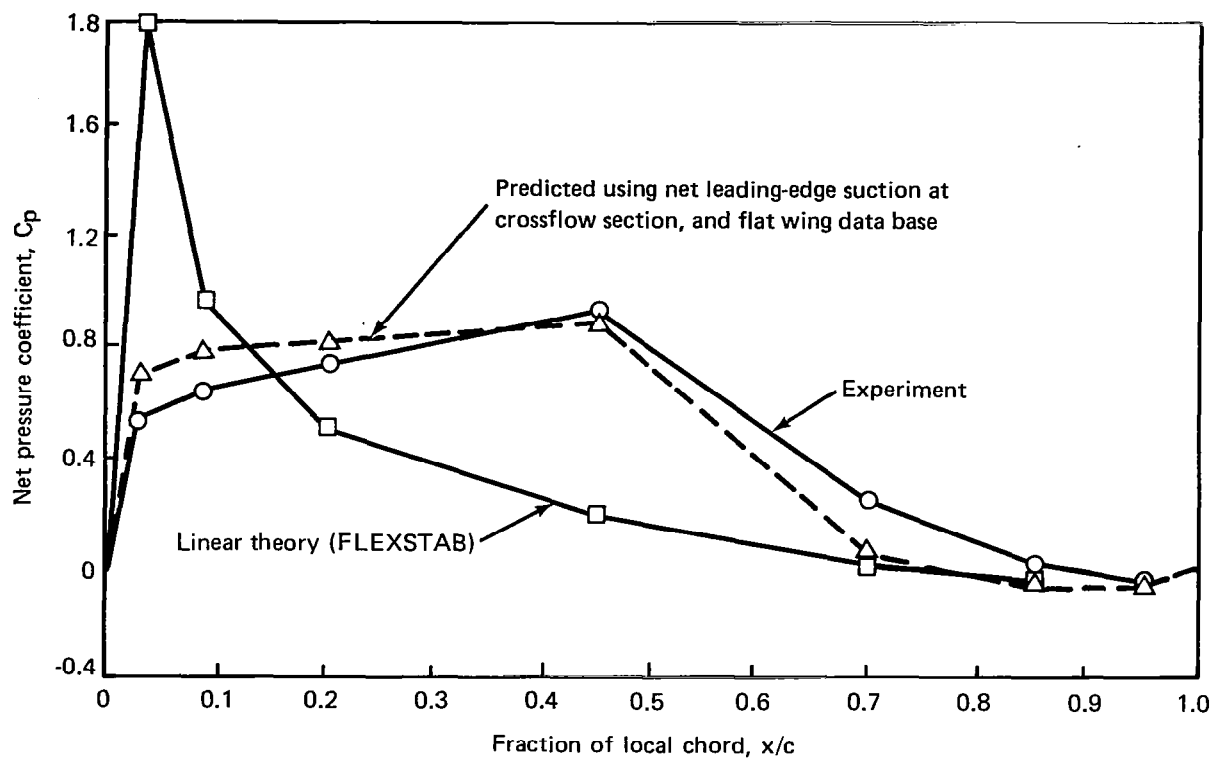


Figure 27.—Pressure Distribution on the Cambered-Twisted Wing Based on the Leading-Edge Suction Coefficients at Constant Body Stations and the Flat Wing Data Base, Streamwise Section, $\eta = 0.50$, $M = 0.85$, $\alpha = 12^\circ$

1. Report No. NASA CR-3641	2. Government Accession No.	3. Recipient's Catalog No.	
4. Title and Subtitle AEROELASTIC LOADS PREDICTION FOR AN ARROW WING Task II - Evaluation of Semi-Empirical Methods		5. Report Date March 1983	
		6. Performing Organization Code	
7. Author(s) Andre C. Wery and Robert M. Kulfan		8. Performing Organization Report No. D6-51762-2	
9. Performing Organization Name and Address Boeing Commercial Airplane Company P.O. Box 3707 Seattle, Washington 98124		10. Work Unit No.	
		11. Contract or Grant No. NAS1-15678	
12. Sponsoring Agency Name and Address National Aeronautics and Space Administration Washington, D.C. 20546		13. Type of Report and Period Covered Contactor Report	
		14. Sponsoring Agency Code 743-01-12-02	
15. Supplementary Notes Technical monitor - Percy J. Bobbitt, Chief, Transonic Aerodynamics Division, NASA Langley Research Center, Hampton, Virginia. Principal investigator - Marjorie E. Manro, Boeing Commercial Airplane Company.			
16. Abstract The accurate prediction of loads on flexible, low aspect-ratio wings is critical to the design of reliable and efficient aircraft. The conditions for structural design frequently involve nonlinear aerodynamics. Two separated-flow computer programs and a semi-empirical method for incorporating the experimentally measured separated flow effects into a linear aeroelastic analysis were evaluated under this contract. These three tasks are documented separately. This report describes the development and evaluation of a semi-empirical method to predict pressure distributions on a deformed wing by using an experimental data base in addition to a linear potential-flow solution. The experimental data accounts for the effects of aeroelasticity by relating the pressures to a parameter which is influenced by the deflected shape. Several parameters were examined before the net leading-edge suction coefficient was selected as the best. The evaluation of R. P. White's (RASA Division of Systems Research Laboratories) separated flow method (Task I) is described in NASA CR-3640. The evaluation of The Boeing Company's Three-Dimensional Leading-Edge Vortex (LEV) code (Task III) is presented in NASA CR-3642. These evaluations were based on a large experimental data base (for three wing shapes) obtained under previous NASA contracts: NAS1-12875, NAS1-14141, and NAS1-14962. Linear theoretical methods were also evaluated under these contracts.			
17. Key Words Aeroelasticity Experimental pressure distributions Aerodynamic theory Arrow-wing configuration Wind tunnel test		18. Distribution Statement Unclassified-unlimited Subject category 02	
19. Security Classif. (of this report) Unclassified	20. Security Classif. (of this page) Unclassified	21. No. of Pages 124	22. Price A06